ADVANCEMENTS IN THE VISUALIZATION OF THERAPEUTIC FOCUSED ULTRASOUND

By

Huiwen Luo

Dissertation

Submitted to the Faculty of the

Graduate School of Vanderbilt University

in partial fulfillment of the requirements

for the degree of

DOCTOR OF PHILOSOPHY

in

Biomedical Engineering

May 31, 2022

Nashville, Tennessee

Approved:

William A. Grissom, Ph.D. (Chair)

Charles F. Caskey, Ph.D.

Li Min Chen, MD, Ph.D.

John C. Gore, Ph.D.

Sandeep Arora, M.B.B.S.

ACKNOWLEDGMENTS

This journey would not have been possible without the support, love, and guidance of many people, who have helped me in many forms to finish the dissertation. I wish to express my gratitude and acknowledge how key people have influenced and mentored me.

First and foremost, I would like to thank my advisor Dr. William Grissom, who has the substance of a genius. He constantly provided guidance and support from the beginning of my Ph.D. journey until the day I had officially completed it. He convincingly guided and encouraged me to be professional and move in the right direction. Without his patience, encouragement, immense knowledge, and enthusiasm, I would have not gone through difficult times and hardly completed this thesis. I am always amazed by how many wonderful ideas he has and how smart he is. I am so proud and grateful that I can work with him and have done many exciting projects. He is always positive and optimistic, and gives me the sweet feedback all the time. When I have low self-esteem, he always tries his best to cheer me up. Thank him for believing in me when I didn't believe in myself. His words of encouragement brightened many of my days and helped sharpen my life for good. I very appreciate the positive influence he has had on me.

I would also like to express my deep gratitude to my dissertation committee: Dr. John Gore, Dr. Charles Caskey, Dr. Li Min Chen, Dr. Sandeep Arora and Dr. William Grissom. I really appreciate it that they are willing to sever on my thesis committee. Their insightful feedback and patient support pushed me to sharpen my thinking and brought my work to a higher level. These projects would not be nearly as good without their help.

My sincere thanks also go to Dr. Diego Hernando and Dr. Scott Reeder for opening the door of this fantastic field and allowing me to work on my first MRI project. Without their guidance and recommendations, I would not have a chance to meet Will and come to the Vanderbilt University.

I wish to acknowledge the help provided by everyone in the Grissom Lab (Jun Ma, Sumeeth Johnathan, Charlotte Sappo, Abitha Srinivas, Jonathan Martin, Chris Vaughn, Megan Poorman, Sarah Garrow and Kristen Zarcone), my colleagues in the Caskey Lab (Michelle Sigona, Thomas Mannuel, M. Anthony Phipps, Aparna Singh and Jiro Kusunose) and Zhangyan Yang in Dr. Gore's Lab. It has been a great honor to work with so many extraordinary people each and every day. They are not only my colleagues, but also my best friends in Nashville. They supported me greatly and were always willing to help me. I would like to especially say thank you to Charlotte and Abitha. They helped me build pretty hardware parts for my work and unblocked my progress. I enjoy studying, working and laughing with them. I also want to extend my sincere thanks to Michelle, Tom and Tony. We have worked at the scanner together for tons of hours for that bright focus in the monkey brain. We failed countless times due to different kinds of unexpected factors, but we never gave up. Thank them for being always positive and making me calm down and move forward. Thanks should also go to everyone at the Vanderbilt University Institute of Imaging science. Thanks for their efforts to build this productive and collaborative environment. I always feel fortunate to work here.

I am also grateful to my friends, Ante Zhu and Annie (Yuxin) Zhang who were PhD students at University of Wisconsin–Madison. Both of them have set an excellent example of student researchers for me. They gave me different insights into MRI field and my career. Although we are in different cities, they are always standing there behind me whenever I need support in academic and personal life.

Last but not least, I want to sincerely thank my parents for their love, encouragement, and sacrifices for educating and preparing me for my future. Without their unconditional love and support, I, a girl born in a small town in China, could not come to Vanderbilt University to pursue my Ph.D. Although they can not give me many suggestions on my career, they always try to support me and encourage me to do whatever I want. I would not be here without them.

Parts of this dissertation appear in the following manuscripts:

Luo, Huiwen, et al. "Rapid quantitative imaging of high intensity ultrasonic pressure fields." The Journal of the Acoustical Society of America 148.2 (2020): 660-677.

Luo, Huiwen, et al. "Reduced-FOV 3D MR acoustic radiation force imaging with a low-rank reconstruction for targeting transcranial focused ultrasound". Magnetic Resonance in Medicine. (under revision)

TABLE OF CONTENTS

LIST OF TABLES

LIST OF FIGURES

CHAPTER 1

Introduction

1.1 Motivation

Ultrasound can produce both mechanical and thermal effects with either high or low pressure waves. This ability enables focused ultrasound (FUS) to become a noninvasive or minimally invasive therapeutic technology (Ter Haar, 1999) that is able to treat tissue deep in the body precisely and noninvasively and offers a complement to surgery (Jolesz, 2009), radiation therapy, drug delivery (Lee et al., 2017), and cancer immunotherapy (Sheybani and Price, 2019). The applications of FUS (Miller et al., 2012; Elhelf et al., 2018; Jiang et al., 2018) with various settings of the ultrasound power, frequency and duration of sonications and using continuous or pulsed modes can induce diverse biological consequences, thereby allowing for treatments of a wide range of medical disorders. FUS has been approved for a broad range of applications including uterine fibroids (Hesley et al., 2013; Stewart et al., 2006) and breast caner (Huber et al., 2001; Furusawa et al., 2006; Schmitz et al., 2008), prostate caner (Blana et al., 2004; Chaussy and Thüroff, 2003; Thüroff, Stefan and Chaussy, Christian and Vallancien, Guy and Wieland, Wolfgang and Kiel, Hans J and Le Duc, Alain and Desgrandchamps, François and De La Rosette, Jean JMCH and Gelet, Albert, 2003) and liver lesions. Recently emerging applications of FUS involve using nonthermal pulsed ultrasound of medium intensity to induce microbubble-mediated opening of the blood-brain barrier (BBB) to facilitate drug delivery (Lipsman et al., 2018; Vykhodtseva et al., 2008; Burgess et al., 2015), and low-intensity pulsed ultrasound to excite or suppress neural activities (Darrow, 2019; Kubanek, 2018) by activating neuronal circuits. The success of these advanced therapeutic FUS procedures highly depends on whether the FUS beam's focus is placed on the target anatomy. This requires a good knowledge of the acoustic energy output and the acoustic field of FUS transducer in both in vivo and in vitro, which are the main focus of this dissertation.

Prior to FUS surgeries, a fundamental knowledge of the free-field output of FUS transducers is necessary for treatment planning, safety and quality assurance. The conventional instruments to measure the output of transducers are hydrophones (O'Reilly and Hynynen, 2010; Haller et al., 2012; Yu et al., 2013) that usually sample only one spatial location at a time and thus require a long acquisition time. There exist other techniques including radiation force balances (Maruvada et al., 2007; Shou et al., 2006), optical methods (Meier, 2002; Venkatakrishnan and Meier, 2004; Goldhahn and Seume, 2007) such as photographic and laser schlieren methods, and laser-based tomographic schlieren methods. However, radiation force balances provide limited or no spatial beam information; optical methods are limited to small field-of-views (FOVs)

and prohibitively expensive. What is more, the optical methods usually require the sophisticated optical setups, which limits their utility. Because of the above limitations of currently existing methods, we desire a method that is inexpensive, simple, and portable enough to be widely used in research and clinic flows and can directly and rapidly provide quantitative spatially-resolved measurements of acoustic fields at therapeutic pressure levels.

The ultrasonic wave field is easily distorted and shifted by the heterogeneities of biological tissue and skull bone in terms of speed of sound, density and ultrasonic attenuation (Fry and Barger, 1978). Magnetic resonance (MR) imaging (Vlaardingerbroek and Boer, 2013) with high spatial resolution, excellent soft tissue contrast and diverse physic parameters can guide FUS for more accurate treatment planning. The development of noninvasive MR thermometry (Rieke, 2011) allows localizing the focus and real-time monitoring the temperature changes for thermal applications of FUS such as thermal ablation. MR-guided FUS (MRg-FUS) therefore (Cline et al., 1992; Schlesinger et al., 2013) become widely used in FUS surgeries. However, MR thermomery has the disadvantages of resulting in tissue heating and unwanted bioeffects (Wang et al., 2014) when FUS is applied for its nonthermal applications in brain. To overcome this challenge, MR acoustic radiation force imaging (MR-ARFI) (McDannold and Maier, 2008; Sarvazyan et al., 1998; Pauly, 2015) was invented to localize the FUS focus with greatly reduced heat deposition by measuring the FUS-induced displacement of tissues. It typically utilizes one ultrasound sonication per repetition time (TR) to induce tissue displacements and then applies motion-encoding gradients (MEGs) to encode the displacements into the phases of MR images. Prevous studies have reported various MR-ARFI techniques (McDannold and Maier, 2008; Kaye et al., 2011; Kaye and Pauly, 2013; Mougenot et al., 2015; de Bever et al., 2016) based on spin-echo and gradient-recalled echo sequences combined with different MEG schemes. Because the ultrasound beam distortion may result in partial or complete destruction of the focusing pattern, a volumetric MR scan that can image the entire focus is desired. 3D MR-ARFI scans (de Bever et al., 2016) are capable to encode a whole brain volume in two dimensions but lead to long scan times because of increased phase-encoding steps. Consequently, it is needed to develop an MR-ARFI technique that can visualize the entire focus in 3D with a short scan time and minimal FUS duty cycle.

1.2 Dissertation Synopsis

To advance the visualization of therapeutic FUS both in free field and in in vivo, this dissertation tackles two limitations which exist in state-of-the-art methods:

1. The high cost, limited-FOV, long acquisition time and sophisticated setup for current ultrasound pressure mapping methods to quantitatively characterize the free-field ultrasonic pressure fields.

2. The relatively long scan times of MR-ARFI methods maintaining a low FUS duty-cycle to encode a volumeric view that can cover the entire focus in transcranial FUS applications.

This dissertation comprises three parts: 1) the design of hardware, control software, acquisition and reconstruction strategies of a novel background-oriented schlieren (BOS) system to enable quantitative rapid imaging of ultrasonic pressure fields at therapeutic levels, 2) pulse sequence development for a 3D reduced-FOV MR-ARFI scan to reduce scan times and keep a minimal FUS duty cycle, 3) the development of a joint low-rank reconstruction to recover the FUS focus in in vivo brain from undersampled datasets acquired with the developed pulse sequence.

Chapter 3 describes a two-dimensional rapid and quantitative method to characterize ultrasonic pressure fields of FUS transducers in free field based on continuous-wave BOS (CW-BOS) imaging, in order to ensure safety and quality assurance of FUS treatments and assist treatment planning. This method needs only a water tank, a background pattern, a camera. It employs a multi-layer deep neural network to reconstruct 2D root-mean-squared (RMS) projected pressure map in the ultrasound propagation dimension and one lateral dimension. The BOS system is able to produce high-resolution quantitative RMS projected pressure maps within a short time (less than 10 seconds). This technique is robust to beam rotations and translations and can map aberrated beams, which can be used to perform more efficient and faster evaluations of FUS transducers for treatments and improve the efficiency of quality assurance procedures.

Chapter 4 details a two-minute reduced-FOV 3D MR-ARFI method with a low-rank reconstruction for targeting transcranial FUS to simultaneously minimize scan time and the FUS duty cycle. The proposed 3D reduced-FOV MR-ARFI technique images a long tube which can cover the entire focus. The scan interleaved FUS-on and FUS-off data collection to improve measured ultrasound-induced displacement maps with 2 mm isotropic resolution and 0.85% FUS duty cycle. A low-rank reconstruction algorithm was developed to allow a scan time of 2 minutes and 20 seconds. This method will enhance the efficiency of targeting the focus for transcranial FUS, especially when it needs to repeated many times when finding, steering and phase-correcting the focus.

CHAPTER 2

Background

2.1 Ultrasound Basics

Sound waves are generated by the propagation of "vibrational energy" through a medium such as gas, liquid and solid. Ultrasound waves are sound waves that can be periodic or pulsed with frequencies greater than the maximum frequency audible to humans, which is 20 kHz (Skudrzyk, 1971; Temkin and Temkin, 1981; Fahy and Walker, 1998). When the ultrasound wave passes through the medium, it produces oscillation of particles about their rest position in medium and alternating compressions and rarefaction of the propagation medium (Jolesz and Hynynen, 2007). The compressions and rarefactions displace particles in the medium so that the wave propagates by transfer of momentum among particles. In most cases, the particles vibrate along the direction of the propagation (longitudinal wave). In some cases, the particles oscillate in the direction that is perpendicular to the propagation direction (Shear wave). Shear waves can propagate in solids such as bone but are quickly attenuated in soft tissues. Thus, longitudinal waves are more common in medical ultrasound applications.

Ultrasound waves are generated by ultrasound transducers by applying an electrical current across a piezoelectric crystal (Jolesz and Hynynen, 2007). The transducer crystal expands and contract proportional to the applied electrical energy to generate vibrations at a high speed and then produce ultrasound waves, causing the conversion from electrical energy to mechanical energy. This is based on the piezoelectric effect, a property of certain materials like quartz discovered in 1881 (Curie and Curie, 1881). In turn, echos reflected back to the crystal generate changes in electrical signals with the amplitude and phase of the received echoes encoded, which can produce image contrast in diagnostic ultrasound imaging.

2.1.1 Ultrasound Propagation

The ultrasound field generated by a transducer is determined by the size, shape and frequency of the source. Assuming a planar circular source, a plane wave travels in the ultrasound field near the source when the source aperture radius is larger than $\lambda/4$, where λ is the acoustic wavelength. A plane wave that propagates along one spatial dimension x through a homogeneous and non-attenuating fluid medium over time t, can be obtained from the acoustic wave equation. The acoustic equation (equation 2.3) is derived by combining Euler's equation (equation 2.1) and the equation of continuity (equation 2.2).

$$\frac{\partial}{\partial x}p(x,t)+\rho_0\frac{\partial}{\partial t}u(x,t)=0 \tag{2.1}$$

$$\frac{\partial}{\partial x}p(x,t)+\frac{1}{\kappa}\frac{\partial}{\partial x}u(x,t)=0 \tag{2.2}$$

$$\frac{\partial^2}{\partial x^2}p(x,t)-\frac{1}{c^2}\frac{\partial^2}{\partial t^2}p(x,t)=0 \tag{2.3}$$

where $c=\frac{1}{\sqrt{\rho_0\kappa}}$ is the speed of sound, ρ_0 is the undisturbed mass density of the medium, κ is the compressibility of the medium and $u(x,y)$ is the particle velocity produced by the wave.

By solving the wave equation, a monochromatic plane wave $p(x,t)$ is expressed as the following equation:

$$p(x,t)=Pcos(\omega t-kx) \tag{2.4}$$

where P is the amplitude of the wave, $\omega=2\pi f$ is the radian frequency and $k=\frac{2\pi}{\lambda}$ is the wave number.

The acoustic intensity $I(W/m^2)$ characterizes the strength of an ultrasound wave. Especially, the intensity of acoustic plane waves can be related to the pressure amplitude:

$$I(W/m^2)=\frac{P^2}{2\rho_0 c} \tag{2.5}$$

where P is the pressure amplitude of the acoustic wave, ρ_0 is the undistributed mass density of the medium and c is the speed of sound. The average speed of sound in most soft tissues is 1540 m/s.

2.1.2 Reflection and Transmission

All materials or tissues could be considered as an impedance of the passage of sound waves. The acoustic impedance of a tissue is determined by its density and elasticity. For the acoustic plane waves, the acoustic impedance (Z) can be expressed by:

$$Z=\rho_0 c=\sqrt{\frac{\rho_0}{\kappa}} \tag{2.6}$$

where ρ_0 is the undisturbed mass density of the medium, c is the speed of sound, and κ is the compressibility of the medium. Generally, the acoustic impedance of most soft tissues is close to that of water (Jolesz and Hynynen, 2007), 1.6×10^6 kgm^{-2}s^{-2}. Fat has a little lower impedance of 1.35×10^6 kgm^{-2}s^{-2} because of its lower density and lower speed of sound. Bone has a significantly higher impedance but lung has a much lower value.

Ultrasound waves are partially reflected at the boundary between the tissues of different densities. The relative proportions of the energy reflected and transmitted are determined by the acoustic impedances of two

types of tissues Z_1 and Z_2, which the reflection coefficient (R) can describe:

$$R = \frac{P_r}{P_i} = \frac{Z_2 cos\theta_i - Z_1 cos\theta_t}{Z_2 cos\theta_i + Z_1 cos\theta_t} \tag{2.7}$$

where P_i and P_r denote the incident and reflected waves, θ_i and θ_t represent the angles of incidence and transmission and the reflection coefficient R is ranged from -1 to 1. The greater the difference in impedance at the boundary, the greater the reflection that will occur, further the smaller the amount of energy that will be transferred. Generally, when the incident angle is not too large, the ultrasound beam suffers little reflection due to the slight difference of impedance values when it penetrates from one soft tissue to another. However, 30% - 40% reflection could result from the interface between soft tissue and bone at the normal incidence of the wave and total reflection of the longitudinal wave at angles larger than 25°.

2.1.3 Attenuation

The intensity and amplitude of ultrasound waves are reduced when they travel though a medium mainly because of two sources: 1) scatter and reflection and 2) absorption, which determines how deep ultrasound beams can penetrate in biological tissues. The degree of ultrasound attenuation in a medium is described by the attenuation coefficient α (dB/cm). The attenuation coefficient is the sum of individual coefficients for scattering α_s and absorption α_a:

$$\alpha = \alpha_a + \alpha_s \tag{2.8}$$

The plane wave with attenuation can be modelled with an exponential term regarding the equation 2.4:

$$p(x,t) = Pe^{-\alpha x} cos(\omega t - kx) \tag{2.9}$$

In addition to attenuation, reflection and scattering of sound at tissue interfaces may lead to the larger attenuation in the presence of small calcification or stones. However, absorption that converts the acoustic energy to heat dominates the attenuation (Bamber and Hill, 1979; Goss et al., 1979). Assuming the heterogeneous medium, the measured absorption coefficients of tissue increases as a function of the frequency (below 15 MHz) as the following equation shows:

$$\alpha_a = a(f)^m \tag{2.10}$$

where a and m are the tissue-specific parameters, and f is the frequency in MHz of the transducer. The parameter m has been found experimentally to be ranged from 1 to 1.2. For most soft body tissues, m is close to 1. The absorption coefficients vary with tissue properties like viscosity and relaxation phenomenon

(Jolesz and Hynynen, 2007). The averaged absorption coefficient in soft tissues is about ranged from 3 to 5 $m^{-1}MHz^{-1}$ except the tendon and testis that have absorption coefficients of 14 and 1.5 $m^{-1}MHz^{-1}$ respectively.

2.2 Effects of Ultrasound on Tissues

Ultrasound can produce a variety of biological effects in tissues that enable its wide range of applications. The bioeffects are produced by either thermal or mechanical mechanisms of interactions between ultrasound and targeted tissues. These bioeffects and their outcomes are determined by tissue properties and the acoustic parameters, including power, pulse duration, continuous or pulsed modes. This section will introduce thermal effects (heating) and nonthermal effects (cavitation and acoustic radiation force).

2.2.1 Thermal Effects

The majority of attenuated acoustic energy in tissues is turned into heat which can cause temperature rises in a small region. Ultrasound can produce different levels of thermal dose and their biological outcomes by changing its acoustic power and duration. A low level thermal rise over several minutes or hours can be created by ultrasound energy for local hyperthermia (Jang et al., 2010); a precisely localized high temperature rise over seconds can be used to destroy the tissue by protein denaturation in thermal ablation (Webb et al., 2011). The temperature rise in tissues depends on the absorption and attenuation coefficients of tissues, the size and shape of the ultrasonic field, and the local blood perfusion rate (Jolesz and Hynynen, 2007). If the temperature rise is large enough and the tissue is heated for an adequate duration, the exposure causes tissue damage. Given the temperature, cumulative equivalent minutes at $43°C$ (CEM_{43}) is the acknowledged metric for thermal dose assessment (Dewhirst et al., 2003):

$$CEM_{43} = \Delta t R^{(43-T)} \tag{2.11}$$

where Δt represents the summation over the length of exposure, T is the average temperature during time interval t, and R is a constant equal to 0.25 for $T < 43°C$ (Dewhirst et al., 2003) and 0.5 for $T > 43°C$. Temperature rises need to be monitored during an ultrasound exposure to ensure adequate thermal does. In terms of MRgFUS, MR thermometry is a powerful imaging method to monitor temperature elevations and control thermal does, which will be discussed in later sections.

2.2.2 Nonthermal Effects

2.2.2.1 Cavitation

Cavitation refers to a process that ultrasound waves interact with dissolved gases when they travel through tissues (Dalecki, 2004). It is the most widely studied nonthermal mechanism that can cause a variety of

bioeffects, from cell membrane permeability changes to complete destruction of tissue. The occurrence of cavitation requires the presence of a stabilized gas body. The dissolved gas bubble is referred to "microbubble". The microbubbles can be introduced intentionally into the body via the injection of gas-based ultrasound contrast agents or can be generated by the peak negative pressure of ultrasound itself at high-pressure amplitudes. There are two different types of cavitation: stable and inertial cavitation.

A gas bubble in an ultrasound field will expand and contract in resonance with the ultrasound wave, caused by the compressions and rarefactions of particles in the medium. The small amplitude oscillations of these bubbles about its equilibrium are named stable cavitation (Flynn, 1964; Liang et al., 2010), and it emits pressure to the surrounding fluid and cause flow around bubble which is termed microstreaming (Elder, 1959). The microstreaming affects diffusion rates and membrane permeability. The stable cavitation is a significant source of scattering.

In inertial cavitation, more gas diffuses into the gas bubble during the expansion phase than diffuses out during the compressive phase. This process is called rectified diffusion. The size of the gas bubble increases during each cycle with more acoustic energy contained. At higher acoustic pressure above a threshold pressure, the bubble may rapidly expand and violently collapse in a liquid medium, releasing a large amount of energy. The released energy is harmful to tissue viability and can completely destroy the exposed tissue (Lele, 1977; Vykhodtseva et al., 1994). The threshold pressure in free fluids increases with frequency, and decreases as the duty cycle and pulse length increase (Jolesz and Hynynen, 2007; Hill, 1972).

2.2.2.2 Acoustic radiation force

When ultrasound propagates through a medium, the absorption and scattering result in acoustic radiation force (Torr, 1984) by a momentum transfer from the propagating wave to the tissue. This force initiates both longitudinal and transverse waves. The acoustic radiation force can be formulated by modeling tissue as a viscous fluid under plane wave assumptions (Lighthill, 1978; Torr, 1984):

$$F = \frac{2\alpha I}{c} \tag{2.12}$$

where F is a force per unit volume, α is the tissue-dependent attenuation coefficient (Neper/cm), I is the temporal average intensity (W/cm^2) and c is the speed of sound in the medium. Equation 2.12 neglects the contributions of scattering in computing the momentum transfer by assuming that absorption dominates the attenuation of ultrasound in soft tissues. For a perfect reflector that is normal to the beam, the acoustic radiation force is only related to the acoustic intensity and the speed of sound: $F = \frac{2I}{c}$ (Torr, 1984). In the materials with relatively low attenuation, the spatial acoustic radiation field is distributed throughout the

geometric shadow of the transducer aperture (Palmeri and Nightingale, 2011). For example, the peak of the acoustic radiation field is near the focal spot of the acoustic field (Palmeri and Nightingale, 2011). In highly attenuating materials, the acoustic radiation force is distributed more evenly and as a result, the peak does not appear near the focal spot.

The static displacement of tissue over time $x(t)$ in response to acoustic radiation force is determined by tissues' elasticity and viscosity. It can be approximately modeled as a over-damped response model (Souchon et al., 2008; Callé et al., 2005; Kaye and Pauly, 2013):

$$\begin{cases} x_{rise}(t) = \frac{F}{k}(1 - e^{-\frac{t}{\tau_{rise}}}); T_{on} \leq t \leq T_{off} \\ x_{decay}(t) = x(T_{off})e^{-\frac{t}{\tau_{decay}}}; t > T_{off} \end{cases}$$

where F is the acoustic radiation force, k is a proportionality constant relating force and displacement, $\frac{F}{k}$ is the maximum displacement achieved with an infinitely long ultrasound pulse, T_{on} and T_{off} are the beginning and the end of the ultrasound pulse, and τ_{rise} and τ_{decay} are the time constants that describes the transient response separately.

A number of imaging modalities based on acoustic radiation force are currently studied, including vibroacoustography, supersonic imaging, shear wave elasticity (SWEI) and ARF impulse (ARFI) imaging (Nightingale, 2011; Palmeri and Nightingale, 2011). In vibroacoustograph, frequency-shifted, confocal beams are used to generate an oscillating radiation force at the target. The tissue response can be measured by a hydrophone or other ultrasonic methods outside the body. Supersonic imaging and SWEI can characterize the shear modulus of tissues by monitoring the shear waves generated by applying a short-duration acoustic radiation force. In ARFI imaging, the micron-scale displacement is generated by applying an ultra-short (under 100μs) ultrasound pulse and then tracked by ultrasonic, correlation-based methods. The tracked tissue response can be used to monitor tissue structure and stiffness, which is an advantageous replacement of manual palpation to evaluate disease. MRI has the ability to encode the tissue displacement induced by the radiation force into image information, which can help visualize the focus during MRgFUS. The relevant technique will be introduced in subsequent sections.

2.3 Ultrasonic Field Measurement

As mentioned earlier, the wide range of medical applications of ultrasound depends on its diverse bioeffects controlled by different acoustic settings. These bioeffects are capable of inducing irreversible changes in biological tissues. Therefore, it is required to characterize ultrasonic fields and know the acoustic intensity being delivered to the patient for treatment efficacy, safety, and planning. Several methods that characterize

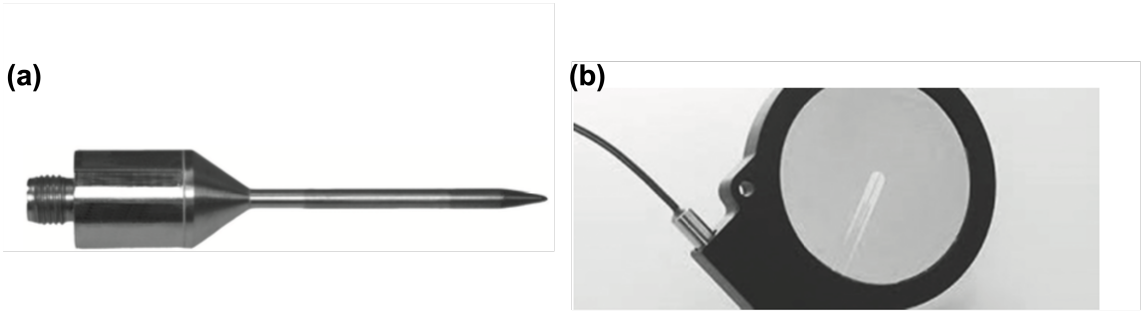

Figure 2.1: Needle (a) and membrane (b) PVDF hydrophone. Adapted from the reference (Zhou, 2015).

the acoustic output of ultrasound equipment have been standardized (Wilkens, 2017). For instance, International Electrotechnical Commission (IEC) 61161 standardizes radiation force balance methods for ultrasonic power, IEC62127-1, 2, 3 standardizes the uses of hydrophones for ultrasonic pressure. Schlieren imaging is also explored for ultrasonic field measurement recently. Many other methods have been developed, such as calorimeter measuring the heat resulting from acoustic energy, holography, and field mapping with vibrometer. This section will only focus on hydrophones, radiation force balance, and schlieren imaging methods.

2.3.1 Hydrophone

Paul Langevin and Constantin Chilowsky developed the first hydrophone in 1915, which was used in German U-boat and submarine surveillance. Today, hydrophones are the most frequently used devices and the gold standard methods for ultrasonic pressure measurements at an infinitesimally small spatial point. There are three commercially available types of hydrophones: needle, membrane, and fiber-optic hydrophones (Zhou, 2015).

Both of needle and membrane hydrophones (piezoelectric type) employ piezoelectric polymer elements such as the piezoelectric polymer polyvinylidene fluoride (PVDF) to convert acoustic pressure into electrical signals. Figure 2.1 (Zhou, 2015) shows the needle and membrane hydrophones, respectively. A needle hydrophone consists of a disc-shaped active element supported at the tip of a needle-like structure (Xing et al., 2021). This compact design enables needle hydrophones can be inserted into small spaces. A membrane hydrophone is composed of a thin PVDF sheet stretched across a hoop a few centimeters in diameter and poled in its center to be piezoelectrically actively in a small circular region of 0.2 - 1 mm in diameter (Szabo, 2004). The membrane hydrophone tends to result in less pressure pulse distortion than another two types due to its relatively uniform sensitivity, but its bulky design prevents its use in many practical applications (Wear et al., 2017). The piezoelectric hydrophones are usually expensive and easily damped by cavitation at high-pressure levels, which limits their uses in some applications.

Different from piezoelectric types, fiber-optic hydrophones are based on optical principles that the index of refraction in the fluid is modulated by the ultrasonic field (Hocker, 1979; Phillips, 1980; Gopinath et al., 2007). The optical fibers sense light modulated by ultrasound wave perturbations at their tips. Laser light is injected into the optical fiber, and the modulated light that is reflected from the tip can be sensed by a broad-band optical detector (Parsons et al., 2006). Compared with piezoelectric types, fiber-optic hydrophones are able to handle higher pressure levels, are easy to repair, and have long-term stability, flat and broad bandwidth (Parsons et al., 2006). However, fiber-optic hydrophones need more care, set-up time, and equipment.

Mapping the ultrasonic field is performed in a testing tank and the hydrophone is connected with a 3D translation stage for scanning the acoustic field mechanically, as Figure 2.2 illustrates. The testing tank is filled with distilled, degassed water to minimize the effect of acoustically-induced bubble cavitations, and it has acoustically treated walls to suppress reflections that might influence the measurements. At each spatial location, the time-varying measured acoustic pressure $p(t)$ measured by hydrophones is calculated by the measured signal in voltage $v(t)$ as follows:

$$p(t) = \frac{v(t)}{M} \tag{2.13}$$

Here, M is the hydrophone's sensitivity whose value is selected at the driving frequency of ultrasound in the frequency response plot. Therefore, hydrophones require relatively long measurement times to acquire a highly spatial-resolved beam map because they sample one spatial point at a time.

2.3.2 Radiation Force Balance Measurements

The radiation force balance is a relatively simple approach to measuring absolute acoustic power by measuring the acoustic radiation force described in section 2.2.2.2. This method measures the time-averaged force exerted by the ultrasonic field on any object which intercepts and totally absorbs the acoustic energy within the field (Zeqiri and Hodnett, 2010). Generally, the setup of radiation force balances consists of a target immersed in a testing tank filled with degassed water and intercepts the ultrasound waves emitted from the transducer. The acoustic power can be calculated from the force balance reading (Szabo, 2004):

$$W = gF \tag{2.14}$$

where W is time-averaged power and g is a constant determined by calibration.

As a benchmark technique, the radiation force balance is quick and easy to use. However, it can only measure acoustic power but not provide detailed spatial beam information. At low power levels, the precision of the radiation force is affected by fluctuations and drifts by the other forces applied to the target (Zhou, 2015).

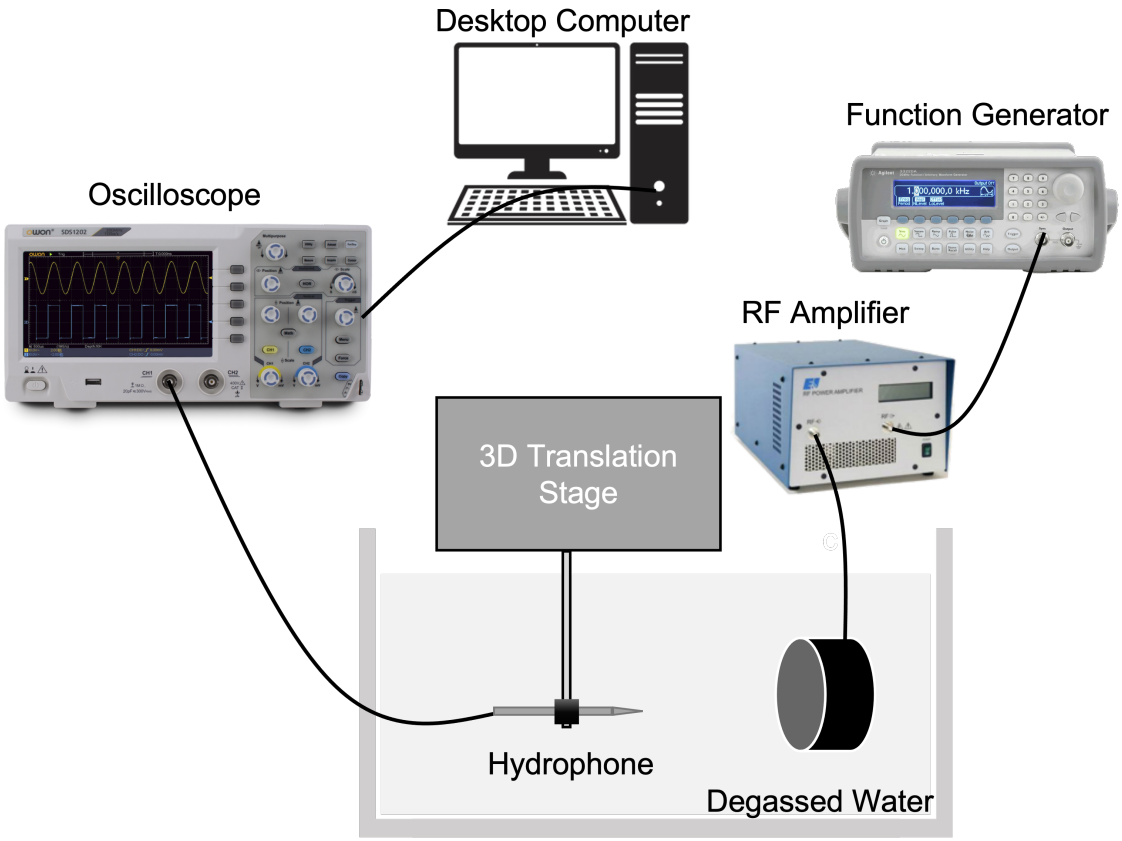

Figure 2.2: Experimental setup for using hydrophones to measure the acoustic out of ultrasound transducers.

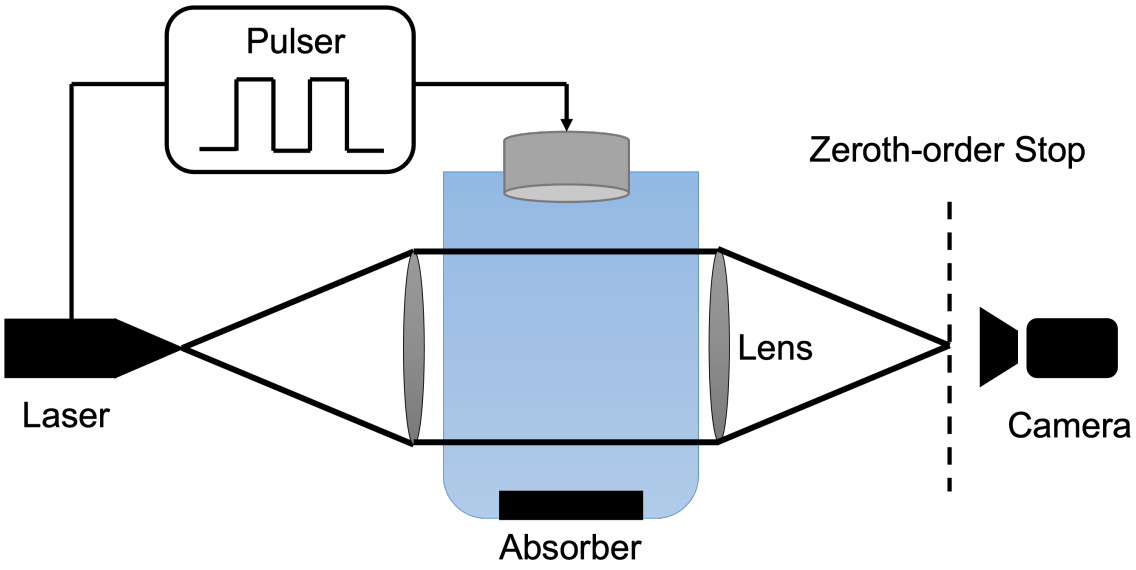

Figure 2.3: Experimental setup for conventional schlieren system for mapping ultrasound beams.

2.3.3 Schlieren Visualization

Raman and Nagendra Nath (1935) first described the fundamental principle and theory of schlieren optical diffraction by sound waves in a transparent medium: ultrasound waves produce a periodic variation in the density and refractive index of the medium and behave as a phase grating to a normally incident planar monochromatic light (Zhou, 2015). Then, schlieren imaging can been applied for the visualization of pressure field produced by ultrasound transducers, according to the interaction of light with transparent media with a nonuniform refractive index such as photographic and laser-based schlieren methods in both two and three dimensions (Bronson, 1969; Newman, 1973; Smith and Thurstone, 1974; Baborovsky, 1979; Reichel et al., 2005; Zanelli and Howard, 2006; Christensen and Chao, 2007; Johns et al., 2007; Neumann and Ermert, 2006; Reibold and Molkenstruck, 1984; Reibold, 1987; Hanafy and Zanelli, 1991; Pitts et al., 1994; Charlebois and Pelton, 1995; Schneider and Shung, 1996). Generally, the optical approaches require an intense point source of light (a laser or an arc lamp) placed at the focal length from a lens to project a parallel beam of light through the transparent medium at a plane that is perpendicular to the ultrasound beam (Hanafy and Zanelli, 1991; Charlebois and Pelton, 1995), as Figure 2.3 describes. The parallel light is blocked at the spatial filter, and the light which is not blocked and was diffracted by the ultrasound beam can be refocused into a two-dimensional image at the zeroth-order stop. The intensity of this image has been proved to be directly proportional to the acoustic power in the beam and equivalent to traditional radiation force balance measurements (Charlebois and Pelton, 1995). Compared with traditional measurements (hydrophones and radiation force balances), schlieren methods offer significant advantages of insensitivity to vibrations, much faster data acquisition,

higher spatial resolution, detailed visualization of beam shape and structure and faster detection of aberrated beams.

Standard 2D schlieren images contain the square of the integral of the peak acoustic pressure, that is, each image represents a projection of the acoustic beam along the light dimension (Charlebois and Pelton, 1995). With a transducer rotated through 180°, a number of images captured at fixed angular intervals can be used to reconstruct the 3D volumetric acoustic pressure distribution using the standard tomographic imaging back-projection methods. 3D schlieren system characterizes ultrasonic pressure fields over the entire observed volume and provides more useful information than 2D methods. However, rotating the transducer itself makes 3D schlieren systems incompatible with in situ clinical transducers and limit their research utility.

Background-oriented Schlieren Imaging

Unlike conventional schlieren systems that require optical setups such as intense point source, collimating lenses and spatial filters, background-oriented schlieren (BOS) imaging is a relatively new technique using a camera to image a background image under uniform and nonuniform conditions of refractive index field, based on light diffraction through a nonuniform refractive index (Raffel, 2015). Cross-correlation of the two background images with and without light diffraction could produce the refractive index maps. Ultrasound waves can cause changes in the refractive index while propagating through the medium, which offers the potential to apply BOS imaging to characterize ultrasonic pressure fields. Figure 2.4 shows a schematic presentation of BOS imaging to measure the acoustic field. At low-pressure amplitudes, the refractive index change can be related to the acoustic pressure with linear approximation (Pulkkinen et al., 2017; Pitts and Greenleaf, 2000; Pitts et al., 2001). The refractive index at location $\boldsymbol{r}$ and time t $n(\boldsymbol{r},t)$ can be denoted as:

$$n(\boldsymbol{r},t) = n_0 + (\frac{\partial n}{\partial p})p(\boldsymbol{r},t) \tag{2.15}$$

where n_0 is the refractive index of the ambient medium, $p(\boldsymbol{r},t)$ is the acoustic pressure at location $\boldsymbol{r}$ and time t and $\frac{\partial n}{\partial p}$ is the adiabatic piezo-optic coefficient (Raman and Venkataraman, 1939; Riley and Klein, 1967). The displacements in horizontal (x) and vertical (y) dimensions of light ray originating from location $\boldsymbol{r}$ at time t and with a propagation distance D can be finally obtained by the projection of pressure gradients with the relation 2.15:

$$\begin{cases} u(x,t) = & D(\frac{\partial n}{\partial p})\int \frac{\partial p}{\partial x}(x,y,z,t)dz \\ u(y,t) = & D(\frac{\partial n}{\partial p})\int \frac{\partial p}{\partial y}(x,y,z,t)dz \end{cases}$$

where u(x,t) and u(y, t) are displacements in x and y dimensions, respectively. Inspired by the above relations, the ultrasonic pressures can be derived from the displacement images derived from background images with

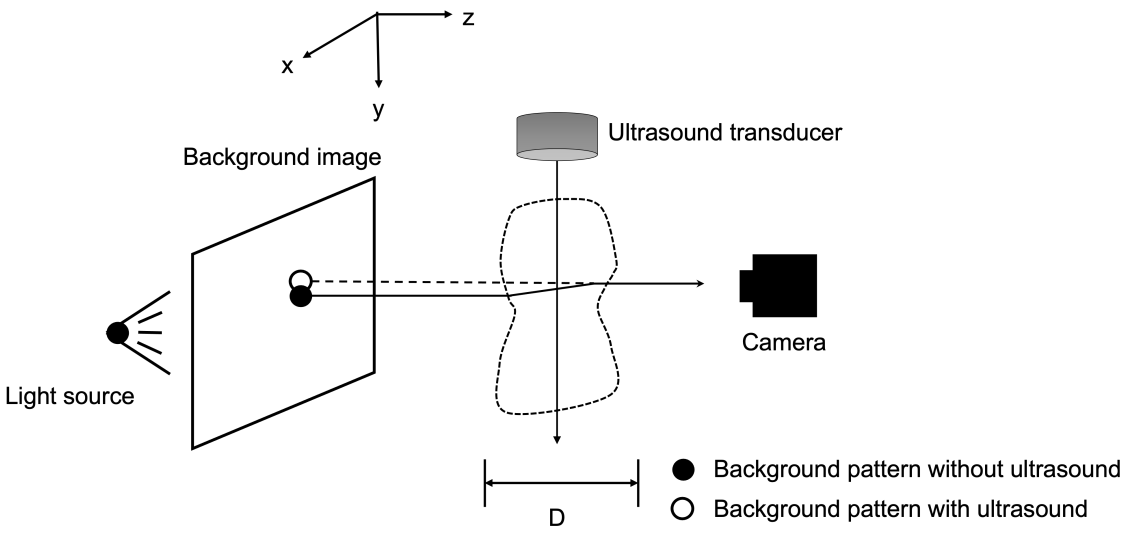

Figure 2.4: A schematic presentation of BOS imaging to measure the acoustic field. The setup consists of a camera, a light source, a background image and a ultrasound transducer. D is the propagation distance of lights in the acoustic field.

and without a nonuniform refractive index.

BOS imaging has been used for qualitative description of the acoustic field in both 2D (Butterworth and Shaw, 2010) and 3D (Pulkkinen et al., 2017). In the previous literatures, it is referred synthetic schlieren imaging. Pulkkinen et al. (2017) proposed to use optical flow algorithms (Horn and Schunck, 1981; Atcheson et al., 2009) to obtain displacement images of refracted light. The acquired images reflect projections of the gradient of refractive index, and then, they can be used to calculate the derivative of ultrasonic fields. Finally, inverse Radon transform and an approximate method were used to compute the 3D pressure field (Pulkkinen et al., 2017).

BOS imaging trades the sophisticated setup of conventional schlieren systems for more sophisticated computation, which is cheaper and easily replicated. It is also much faster than hydrophones and can provide beam shape and structure within short times. However, the existing BOS methods are mainly for qualitative visualization of the ultrasound beam. In this dissertation, Chapter 3 will describe a novel method based on BOS imaging to rapidly and quantitatively characterize the ultrasound beam and the method is demonstrated by comparing it with hydrophone measurements quantitatively.

2.4 Applications of Therapeutic Focused Ultrasound

2.4.1 A Brief History

In 1932, H. Freundlich, K. Collner, and F. Rogowski (Freundlich et al., 1932) proposed applying ultrasound to therapeutically heat tissues, which was the first thought of the use of therapeutic ultrasound. Lynn et al.

(1942) first used the focused ultrasound to produce lesions deep in the bovine liver without causing any damage to surrounding tissues. Then, the Fry Brothers Fry et al. (1955) designed the first FUS device with four piezoelectric transducers to focus ultrasound waves and produce pinpoint lesions without unwanted damage, mainly to treat symptoms with Parkinson's disease. Later on, Lynn and Putnam (1944) performed the first preclinical study using FUS to destroy cerebral tissue in animals. They studied the effects of FUS in a total of 37 animals and found that the lesions were well-circumscribed on physical examination of the areas. In 1950, Lars Leksell designed a specially adapted frame and ultrasound transducer for the lesion and successfully applied it to treat psychiatric orders, which was the first therapeutic use of FUS. Until 1992, MRI was first combined with FUS to guide and monitor tissue damage (Yang et al., 1992), which boosted the development of therapeutic use. Moreover, advanced phase-arrayed transducers were proved to focus waves through the skull and be feasible to use cavitation for through skull treatments, resulting in many breakthroughs in transcranial treatments using FUS. In 2004, the INSIGHTEC's Exablate system was first approved by FDA for thermal ablation treatment of uterine fibroids (Ringold, 2004). Thereafter, MRgFUS systems have been FDA-approved for musculoskeletal diseases including bone metastases and osteoid osteoma, neurological diseases such as essential tremor and Parkinson's disease, tremor, urological diseases for benign prostatic hyperplasia and prostate cancer. Currently, 152 clinical disorders with FUS are under development, which is still increasing. In addition, there have been 34 indications of regulatory approval worldwide. In the US, seven indications have been approved by the FDA. Therapeutic FUS is still rapidly developing. Numerous researchers are still contributing to utilizing FUS to provide significant therapeutic and cost-effective values for more diseases.

General clinical procedures for MRgFUS comprise four parts (Payne et al., 2021): patient preparation (e.g., skin hair removal, anesthesia), treatment planning, treatment delivery, and post-treatment assessment. In treatment planning, the patient is required to lie in the bore of MRI scanner. The targeted anatomy is located as close as possible to the isocenter. Then, initial and structural images are acquired to check bubbles for coupling between the ultrasound transducer and skin, and prescribe overlapping volume to cover the target. MR thermometry or MR-ARFI could be used for verifying the localization of the focal spot. For treatment delivery, ultrasound sonication is usually accompanied by MR scans. For example, function MRI is performed when applying FUS for neuromodulation, and real-time MR thermometry monitors temperature rises and thermal dose for thermal ablations. The patient's status is periodically assessed to ensure safety. Lastly, before removing the patient from the MRgFUS table, dynamic contrast-enhanced MRI scans are performed to evaluate tissue changes for post-treatment assessment. Figure 2.5 shows detailed steps for treatment planning and treatment delivery in clinical MRgFUS workflow.

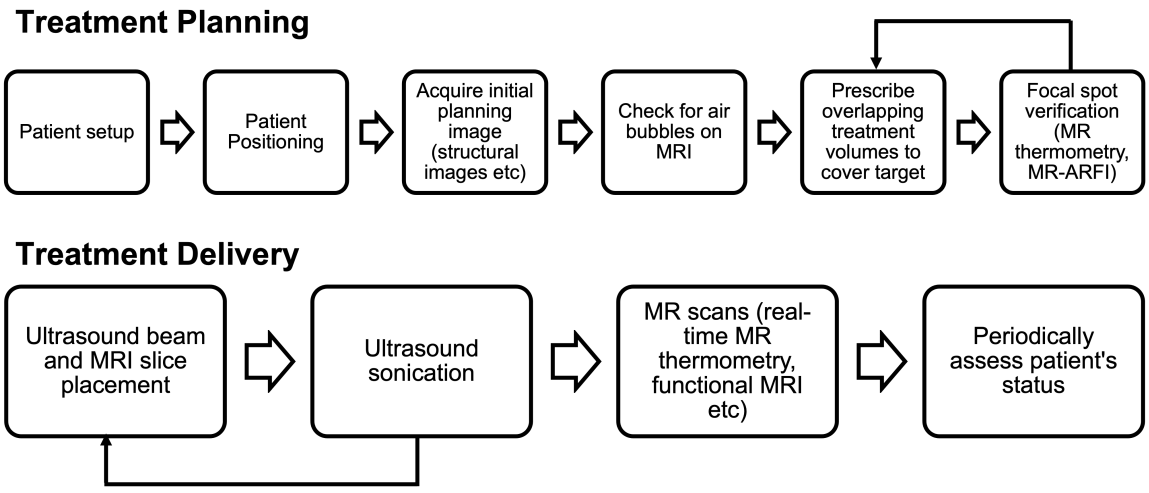

Figure 2.5: Workflows for treatment planning, treatment delivery for MRgFUS.

2.4.2 Applications

Brain applications are more challenging since the skull attenuates and distorts ultrasound emission. The recent advancements in the noninvasive transcranial focusing methods and MRI guidance (which will be talked about in section 2.6) contribute to the emerging applications of focused ultrasound (FUS) for brain surgery and therapy for both ablative and nonablative applications, including the treatments of essential tremor (Benabid et al., 1991), Parkinson disease (Moosa et al., 2019; Magara et al., 2014), obsessive-compulsive disorder (Kim et al., 2018), chronic pain (Meng et al., 2021; Todd et al., 2020), blood-brain barrier (BBB) (Vykhodtseva et al., 2008; Lipsman et al., 2018) and neurodegenerative diseases (Miller and O'Callaghan, 2017). The effects of some ablative applications such as tissue destruction and clot lysis are permanent. This section will mainly focus on applications that are transitory and reversible - neuromodulation and BBB opening.

2.4.2.1 Neuromodulation

Neuromodulation is a technology that acts directly upon nerves. It allows reversible stimulation or suppression of neural activity in the central, peripheral or autonomic nervous systems. Neuromodulation could potentially enable numerous therapeutic effects such as targeting regions in the brain for ablative procedures, suppressing epileptic seizures or symptoms of psychiatric disorders, reversible nerve blocks to treat pain, and brain mapping. Deep brain stimulation (DBS), transcranial magnetic stimulation (TMS) and transcranial current stimulation (TCS) are widely used and studied to control modulation of brain activity. However, DBS involves an invasive procedure of surgical implantation of electrodes into the brain targets, which may lead to

infection or hemorrhage (Bergey et al., 2015). Both TMS and TCS are lack of spatial specificity and penetrate depth, resulting in their limited use in clinical studies (Fregni and Pascual-Leone, 2007).

Transcranial FUS at low intensities can reversibly stimulate or suppress neural activity noninvasively (Khraiche et al., 2008; Tufail et al., 2010; Tyler et al., 2008). It is more advantageous than magnetic or electric non-invasive brain stimulation because it has a higher spatial resolution and a better penetration depth (Di Biase et al., 2019). FUS with a range of frequency (220 kHz-1.9 MHz) has been used to produce effective neuromodulation safely in a series of experiments on rodents, large animals, and primates, including humans (Naor et al., 2016; King et al., 2013; Kim et al., 2014; Deffieux et al., 2013; Fomenko et al., 2018; Yang et al., 2018). The mechanisms are dominated by the mechanical interaction between FUS and neuronal membranes. The mechanical effects of FUS can modify the membrane gating kinetics with the acoustic radiation force through the action on neurotransmitter receptors. In addition, the mechanical interaction may induce cavitation into the cellular membrane, which changes the membrane permeability.

FUS neuromodulation can be achieved by two paradigms: continuous or pulsed ultrasound waves. Functional MRI scans are performed to investigate the FUS-induced neural activities. Thermal and mechanical indexes that describe thermal and mechanical effects of FUS are necessary for safe treatments. Firstly, local heating should be avoided since it can lead to cell death through protein denaturation. Thermal index, the ratio of total acoustic power to the acoustic power required for temperature rises of 1°C, is used to describe thermal effects. Then, the inertial cavitation (mechanical) induced by high peak negative pressure can also generate tissue damage. The mechanical index is to depict mechanical effects and it is directly proportional to the peak negative pressure and inversely proportional to the frequency of the beam. Recent studies have been typically performed at relatively low pressures (under 6 MPa within 300 msec) (Kubanek, 2018). These protocols lead to minimal temperature increases of less than 0.01°C (Tyler et al., 2008).

2.4.2.2 Blood-Brain Barrier Opening

The blood-brain barrier (BBB) is a specialized structure of the blood vessel wall consisting of tightly jointed cells in the brain. It limits transport and diffusion from the vasculature to the central nervous system and prevents harmful substances such as toxins and infectious agents from diffusing into the surrounding brain tissue (Jolesz and Hynynen, 2007). As a consequence, it also limits the amount of many therapeutic and imaging agents that can reach diseased brain targets. Therefore, safely and temporally opening the BBB is promising for treating a broad range of brain tumors, neurological diseases (e.g., Alzheimer's disease) and neurological disorders (e.g., epilepsy).

Early studies (Bakay et al., 1956; Ballantine et al., 1960; Patrick et al., 1990; Vykhodtseva et al., 1995) first observed that FUS could disrupt the BBB at or near ablation intensities while accompanied with neuronal

damage through cavitation. Cavitation is the principal cause of BBB disruption (Sheikov et al., 2008; Tung et al., 2011). The main hypothesis is that microbubbles vibrate due to cavitation and exert force on the capillary walls, which widens the tight junctions between cells in the BBB. However, to induce cavitation with FUS, large amounts of energy are needed and can cause harmful effects on tissues. FUS combined with microbubbles that are induced by injection of ultrasound-contrast agents, can reduce the acoustic intensity and result in BBB opening noninvasively in a targeted region with a reduced risk of unintended tissue damage (E Konofagou et al., 2012; Vykhodtseva et al., 2000; McDannold et al., 2005).

In most studies, pulsed FUS is applied for the opening of BBB for hours. After the procedure, BBB disruption is verified by MR contrast imaging (Kinoshita et al., 2006) using intravenous gadolinium contrast injection. Since various combinations of FUS parameters are employed in the existing studies, the mechanical index is utilized to measure the potential bioeffects. In general, low mechanical indices are ranged from 0.32 to 0.47. The mechanical indices from 0.82 to 0.98 are considered mild. A mechanical index of 0.4 is roughly thought to be the transition to the inertial cavitation in the presence of microbubble contrast agents (Arif et al., 2020; Fowlkes et al., 2008).

FUS-induced BBB opening has been successfully validated in animal studies safely and without evidence of adverse side effects (Fishman and Frenkel, 2017; Kinoshita et al., 2006; Meng et al., 2019; Aryal et al., 2013; Horodyckid et al., 2017). In 2018, Lipsman et al. (2018) presented the first human study without significant negative events. Besides, more clinical studies (Abrahao et al., 2019; Mainprize et al., 2019) further proved the safety and efficacy of FUS for BBB opening in humans. FUS assisted with microbubbles is promising to enhance drug treatment of brain disorders and gene therapy delivery in the future.

2.5 Magnetic Resonance Imaging (MRI)

MRI is a powerful noninvasive imaging modality that can produce high quality images of the inside of the human body with good spatial resolution. Compared to computed tomography (CT), MRI involves no ionizing radiation so it has no health risks. MRI can image a great variety of physic parameters, provide both anatomic imaging and valuable metabolic information with superior soft-tissue contrast. MRI stems from the phenomenon of nuclear magnetic resonance (NMR), which was first described by Felix Bloch and Edward Purcell (Bloch, 1946; Purcell et al., 1946; Lauterbur, 1973). This section will briefly discuss the MR basic physics from a classical view.

2.5.1 MR Physics

The atomic nuclei with an odd number of protons such as ^{1}H, ^{31}P and ^{23}Na possess the intrinsic angular momentum ('spin'). Because ^{1}H is the most abundant in the human body, the proton is the dominant nucleus

in MRI. MRI images human body by manipulating magnetization and detect the bulk precession of the hydrogen spins in water, fat and other organic molecules (Brown et al., 2014).

2.5.1.1 Magnetization, Precession and Relaxation

When placed in a strong static field B_0, the spins tend to align in the direction of B_0 (z) and a net magnetization moment $\mathbf{M}$ is produced. The direction of the main field B_0 (z) is the longitudinal direction while another two dimensions (xy) perpendicular to the z dimension are the transverse direction. The spins precess about B_0 at the Larmor frequency:

$$\omega_0 = \gamma B_0 \tag{2.16}$$

where γ is the gyromagnetic ratio that is determined by atomic species.

At thermal equilibrium, $\mathbf{M}$ will point in the same direction as B_0. Applying an additional radiofrequency (RF) field B_1 in the transverse direction rotating at the Larmor frequency can induce a torque to let spins rotate away from their equilibrium position (z) and precess about the z-axis. The transverse component of the magnetization causes the change in flux in the receiver coil (mostly the same coil that generates RF field) and then the coil can detect the precessing magnetization as MR signals.

After applying RF field B_1, the magnetization experiences relaxation: the transverse component of the magnetization decays over time, and the longitudinal component regrows to its equilibrium state. The decay of the longitudinal component M_z can be described as:

$$M_z = M_0 + (M_z(0) - M_0)e^{-t/T_1} \tag{2.17}$$

where T_1 is the spin-lattice time constant that involves the exchange of energy between the nuclei and the surrounding lattice. The transverse component M_{xy} decays with the spin-spin time constant T_2:

$$M_{xy} = M_0 e^{-t/T_2} \tag{2.18}$$

Bloch Equation

The interaction of the magnetization $\mathbf{M}(t)$ with magnetic fields $\mathbf{B}(\mathbf{t})$ could be described by the Bloch equation:

$$\frac{d\mathbf{M}}{dt} = \mathbf{M} \times \gamma\mathbf{B} - \frac{M_x\mathbf{i} + M_y\mathbf{j}}{T_2} - \frac{(M_z - M_0)\mathbf{k}}{T_1} \tag{2.19}$$

$\mathbf{B}(\mathbf{t})$ is composed of three types of magnetic fields: the main field B_0, RF fields B_1 for excitation and gradient fields for spatial encoding.

2.5.1.2 Spatial Localization and K-Space

The spatial localization in MRI is achieved by applying smaller linear gradient magnetic fields in addition to the main field B_0. If a gradient field $\mathbf{G}$ is applied, the frequency of the spins is a function of its location $\mathbf{r}$:

$$\omega(\mathbf{r}) = \gamma(B_0 + \mathbf{G} \cdot \mathbf{r}) \tag{2.20}$$

By applying different gradients, spins at each locations have a unique processional frequency so that spatial information can be encoded into MR signals by accumulated phase over time.

For a single spin, the accumulated phase can be denoted by $\phi = \gamma(x \int G_x dt + y \int G_y dt)$. The measured time-domain MR signal over spins is given by:

$$S(t) = \int \int m(x,y) e^{-i\gamma(x \int G_x dt + y \int G_y dt)} dxdy \tag{2.21}$$

With the definition of the time integrals of the gradient waveforms, $k_{x,y}(t) = \frac{\gamma}{2\pi} \int_0^t G_{x,y}(\tau) d\tau$, the signal equation becomes:

$$s = \int \int m(x,y) e^{-i2\pi[k_x(t)x + k_y(t)y]} dxdy \tag{2.22}$$

According to this signal equation, the MR images can be recovered from the acquired k-space by 2D or 3D inverse Fourier transform.

2.5.1.3 Constrained MR Undersampled Reconstruction

In MRI, speeding up data acquisition via undersampling the k-space data is desired to achieve high resolution, reduce motion artifacts and provide more comfort to the patients. Undersampling is typically associated with aliasing or other artifacts caused by missing data. Fortunately, the developed advanced reconstruction techniques with constrained and regularization methods can recover unaliased reconstruction from the undersampled data. This section will discuss the general formulation for the constrained MRI, and then the structured low-rank modeling used in Chapter 4.

MR reconstruction is a problem that estimates the image from the recorded signals by the receiver coil. The MR reconstruction problem is undetermined because the magnetization of the underlying object is a space-limited continuous-space function but only a finite set of samples are acquired. In common, the measured MR signals are linear functions of the discrete object's transverse magnetization. The measurements in k-space can be denoted by a linear problem:

$$\mathbf{b} = \mathbf{E}\mathbf{x} \tag{2.23}$$

where **E** is the encoding matrix including k-space sampling and Fourier transform, **b** is the vector of the k-space samples and **x** is the unknown vector of image intensities.

The regularization method can solve this ill-posed MR image reconstruction problem and it is typically formulated as a optimization problem as follows:

$$\hat{\mathbf{x}} = \underset{x}{\operatorname{argmin}} \|\mathbf{b} - \mathbf{E}\mathbf{x}\|_2^2 + \lambda A(\mathbf{x}) \tag{2.24}$$

where the image $\hat{\mathbf{x}}$ is estimated by balancing data consistency ($\|\mathbf{b} - \mathbf{E}\mathbf{x}\|_2^2$) and the regularization term $A(\mathbf{x})$, $\lambda > 0$ is a parameter that controls the degree of regularization, and **E** is encoding matrix that is mostly written as **E = UFS** (**U**: undersampling matrix; **F**: Fourier transform; **S**: Coil sensitivities). Assumptions and prior-information can be incorporated into the cost function $A(\mathbf{x})$ to stabilize the solution.

2.5.1.4 Structured Low-Rank Approaches for MR Reconstruction

The structured low-rank MR reconstruction relies on the annihilation property (Ongie and Jacob, 2015, 2016, 2017; Jin et al., 2016; Jacob et al., 2020). If we assume that the edge locations of the image f are represented by the zero-level sets of a 2D periodic band-limited function $\hat{h}(\mathbf{x}) = \sum_{k\in\Lambda} h[\mathbf{k}] exp(i\mathbf{k}^{\mathbf{T}}\mathbf{x})$ in a rectangular region $\Lambda \subset \mathbb{Z}^2$ (Jacob et al., 2020):

$$\mathrm{C} = \{x | \hat{h}(\mathbf{x}) = 0\} \tag{2.25}$$

It can be shown that there exists a multiplication-based space-domain annihilation relation:

$$\nabla f(\mathbf{x}) \cdot \hat{h}(\mathbf{x}) = 0 \tag{2.26}$$

The above multiplication relationship can be converted into Fourier domain Vetterli et al. (2002):

$$(h * \hat{\nabla} f)[\mathbf{k}] = 0 \tag{2.27}$$

Further, the convolution relation can be rewritten in the matrix form as:

$$\mathbf{H}(\hat{f})\mathbf{h} = 0 \tag{2.28}$$

where **H** is the block Hankel matrix and **h** represents the vectorized filter coefficients. Equation 2.28 shows that the Hankel matrix becomes low-ranked if the filter size is large enough. Therefore, we are able to use the low-rank property to recover the missing k-space data.

The structured low-rank reconstruction can be formulated as the following optimization problem to use

the matrix completion to estimate the missing k-space data:

$$\min_{\hat{g}\in\mathbb{C}^n} \|\hat{g}[\mathbf{k}] - \hat{f}[\mathbf{k}]\|_2^2, \quad \text{s.t. } \text{rank}(\mathbf{H}(\hat{g})) \leq r \tag{2.29}$$

where $\hat{f}[\mathbf{k}]$ denotes the measured sparse k-space samples, $\hat{g}[\mathbf{k}]$ represents the estimated k-space measurements, $\|\cdot\|_*$ represents the nuclear norm, and r is the predefined threshold of rank. The nuclear norm can be minimized by computing truncated singular value decomposition (SVD) (Haldar, 2013; Shin et al., 2014). However, this method is highly non-convex and needs lots of computations due to large matrices. More recently, SVD-free optimization approaches are proposed to reduce the required computations, avoid storing large matrices, improve recovery, and enable more new applications. (Ongie and Jacob, 2015, 2016; Jin et al., 2016) .

2.6 MRI for Guiding Focused Ultrasound

MRgFUS has opened a new revenue with the advantages of MRI, including providing high resolution, great soft-tissue contrast, quantitative temperature mapping, and the ability to target the location of FUS focus, which leads to more advances in treatments of diseases in the brain, prostate, and breast. MRI plays a vital role in treatment planning, monitoring, and assessment of FUS surgery. First, MRI can produce high-resolution anatomical images and the images that can visualize the FUS beam to place the focus on the targeted anatomy for treatment planning. Then, real-time MR temperature mapping can monitor temperature rises and control thermal dose for ablative applications during treatment, or functional MRI can monitor the neural activities resulting from FUS-induced neuromodulation. Finally, treatment assessment can be done with the acquisition of T_{2w} fat-saturated images followed by T_{1w} fat-saturated sequences acquired after the administration of clinically approved gadolinium-based contrast agents for applications such as BBB opening (in Chapter 4) and bone metastases (Payne et al., 2021). This dissertation will focus on the stage of treatment planning. Prior to applying FUS treatments, it is required to know the location and beam intensity of the focus spot. MR thermometry (Rieke, 2011; Quesson et al., 2000) and MR-ARFI (McDannold and Maier, 2008; Huang et al., 2009) are basic tools to localize the FUS during this stage and will be introduced in the following sections.

2.6.1 MR Thermometry

It is essential to monitor temperatures at the treated tissue for the safety of thermal therapy such as hyperthermia (43-45 °C for several tens of minutes) and thermal ablation (50 - 80 °C for shorter time). MRI is sensitive to temperature with a number of parameters, e.g., the proton density, the T_1 and T_2 relaxation times,

the diffusion coefficient, magnetization transfer, and the proton resonance frequency (PRF). This section will only discuss the two most commonly used techniques - PRF shift thermometry (Poorter et al., 1995; Ishihara et al., 1995), and T_1-based method that is suitable for fatty livers (Bloembergen et al., 1948; Parker, 1984).

PRF Shift Thermometry

In water molecules, the hydrogen nuclei ^{1}H are protected by a "shield" produced by the electrons circulating around the them. The "shield" gives rise a "induced" magnetic field B_{0s} that opposes B_0. The local magnetic field B_{local} that the nuclei experience becomes:

$$B_{\text{local}} = B_0 - B_{0s} = (1-s)B_0 \tag{2.30}$$

where s is the shielding constant relying on the local chemical environment. Then, the resonant frequency of the nucleus is written as:

$$\omega = \gamma B_0(1-s) \tag{2.31}$$

where γ is the gyromagnetic ratio of hydrogen. Hydrogen bonding occurs when the hydrogen atom of one water molecule interacts with the oxygen atom of another molecule. The hydrogen-bonded ^{1}H nuclei experience a stronger local field than those in free water molecules. When temperatures increases, the hydrogen bones stretch, bend and break, resulting in more screening effects - a larger screening constant s, a lower local magnetic field B_{local}, and thus a lower resonance frequency. The screening constant increases linearly with temperature at a rate of -1.03 $\pm$ 0.02 $\times$ 10^{-8} °C in the range between -15 °C and 100 °C (Kuroda, 2005; Hindman, 1966).

Temperature maps can be obtained from measuring the temperature-independent change in resonant frequency, mostly using a gradient-recalled echo (GRE) imaging sequence. Images before and during heating are acquired first and their phase differences are calculated to eliminate temperature-independent effects (e.g., B_0 inhomogeneities). The phase differences can be written as:

$$\Delta T = \frac{\phi(T) - \phi(T_0)}{\gamma \alpha B_0 T E} \tag{2.32}$$

where ϕ(T) is the phase of the image during heating, $\phi(T_0)$ is the baseline image before heating. B_0 is the main field strength, γ is the gyromagnetic ratio and TE is the echo time. α = - 0.01 ppm/°C is the PRF change coefficient for aqueous tissues. The temperature accuracy is determined by the phase contrast-to-noise ratio. Assuming the signal intensity only depends on the imaging parameters, it can be derived that the optimal TE is T_2^* (Cline et al., 1996; Kuroda et al., 2000). Moreover, the effects of tissue types, susceptibility, and

external field drift also need to be considered for the accurate measurements of temperatures. First, PRF shift thermometry is only suitable for aqueous tissues because the heat-induced changes in the hydrogen bonds are absent in fat (Hindman, 1966). Then, the susceptibility constant changes with temperatures due to the temperature dependence of magnetic flux density, affecting the local magnetic field. The susceptibility change is 0.0026 ppm/°C in pure water, 0.0016 ppm/°C in muscle tissue (Poorter et al., 1995). For applications of PRF shift thermometry in aqueous tissues, susceptibility is neglected, and we mainly consider the temperature-dependent effects of a much larger screening constant. In addition, an extra phase shift can be caused by an intense gradient utilization (El-Sharkawy et al., 2006). The phase shift is termed as phase drift, which can be measured with a reference phantom at a fixed temperature (Depoorter et al., 1994) and corrected by advanced reconstruction techniques automatically (Grissom et al., 2010; Rieke et al., 2007).

T_1- Relaxation Thermometry

In biological tissues, temperature changes act on dipole interactions between molecules that result in spin-lattice relaxation and thereby cause the changes in relaxation time T_1 (Abragam, 1961). The temperature-dependent T_1 can be denoted as:

$$T_1(T) = T_1(T_{ref}) + m \cdot (T - T_{ref}) \tag{2.33}$$

where m = dT_1/dT in ms / °C or %°C is a tissue-dependent parameter that is determined empirically, T_{ref} is the starting temperature. The temperature dependence is generally 1 %/°C, 1 - 2%/°C in liver and 0.97%/°C in fat (Matsumoto et al., 1992; Hynynen et al., 2000). The temperature dependence of T_1 can be detected in T_1-mapping methods and T_1-weighted images (Odéen and Parker, 2019). For T_1 mapping methods, the current temperature can be calculated according to the equation 2.33:

$$T = \frac{T_1(T) - T_1(T_{ref})}{m} + T_{ref} \tag{2.34}$$

Therefore, T_1 mapping is desired to be rapid and accurate. Unfortunately, conventional T_1 mapping methods such as inversion recovery and saturation recovery are time-consuming. The newer methods, such as dual-TR spin echo or variable flip angle gradient echo methods, can overcome this limitation by only acquiring a few measurements (Prato et al., 1986; Fram et al., 1987). For T_1-weighted images, the changes in signal intensity can give a qualitative measurement of temperatures. However, it is still challenging to apply T_1-based thermometry methods. The parameter m in equation 2.33 varies with tissues, and it is very difficult to estimate m for each tissue type. Also, nonlinear effects will occur when the tissue properties change due to heating and then the equation 2.34 becomes problematic. These limitations may lead to erroneous temperature measurements.

In general, T_1-based thermometry is primarily used in adipose tissues. In other cases, the PRF shift thermometry is more frequently because of its robustness, higher accuracy and better resolution.

2.6.2 MR Acoustic Radiation Force Imaging

In MRI, the magnetic field gradients can be used not only in spatial coding but also in sensitizing MRI signals to molecular diffusion or tissue motion, which is used a lot in MR diffusion-weighted imaging and MR elastography. MR-ARFI is a technique that uses motion-encoding gradients (MEGs) to map the tissue displacements during the short-pulsed ultrasound, and it can localize the FUS and evaluate the delivered energy in in vivo imaging. The phase shift (ϕ) of MR signal encoded by MEGs is related to the ultrasound-induced displacements $x(t)$ and the MEG's strength ($G_{enc}(t)$) as the following equation:

$$\phi = \gamma \int_{T_0}^{T_{end}} G_{enc}(t)x(t)dt \tag{2.35}$$

Here, T_0 and T_{end} are the beginning and the end of encoding. The tissue displacement $x(t)$ is related to the acoustic radiation force, depending on the elasticity and viscosity of tissues (Kaye and Pauly, 2013). Provided that the tissue is static during the rectangular encoding gradients, the tissue displacement (Δx) can be calculated from the phase difference (ϕ) between two images with and without ultrasound sonications as the relationship:

$$\Delta x = \frac{\Delta\phi}{2\gamma G_{enc}\tau} \tag{2.36}$$

where γ is the gyromagnetic ratio and τ is the gradient duration. The displacements encoded with trapezoidal gradients can be approximately calculated using the above equation since the rise time is commonly much shorter than the gradient duration and it is negligible.

The variations of both spin-echo and GRE sequences with various MEG schemes have been developed for MR-ARFI. McDannold and Maier (2008) proposed the earliest 2D MR-ARFI spin-echo sequence consisting of a pair of unipolar MEGs placed before and after the 180° refocusing pulse symmetrically, as shown in Figure 2.6. The ultrasound emission was synchronized with the first or second lobe for displacement encoding at each TR. Subsequently, the optimized gradient schemes such as pairs of repeated bipolar and reverted bipolar gradients were reported and demonstrated to improve displacement sensitivity and SNR (Chen et al., 2010). The use of regular 2D GRE sequences with single bipolar (Auboiroux et al., 2012; Vappou et al., 2018) and tripolar (Hertzberg et al., 2010) gradients were also reported in the previous studies, and an example of MR-ARFI GRE sequences with single bipolar gradients is presented in Figure 2.7. Then, Zheng et al. (2018) proposed to use the transition band of balanced steady-state free precession sequence with a higher displacement sensitivities (five times) than conventional 2DFT MR-ARFI GRE sequences. To accelerate the

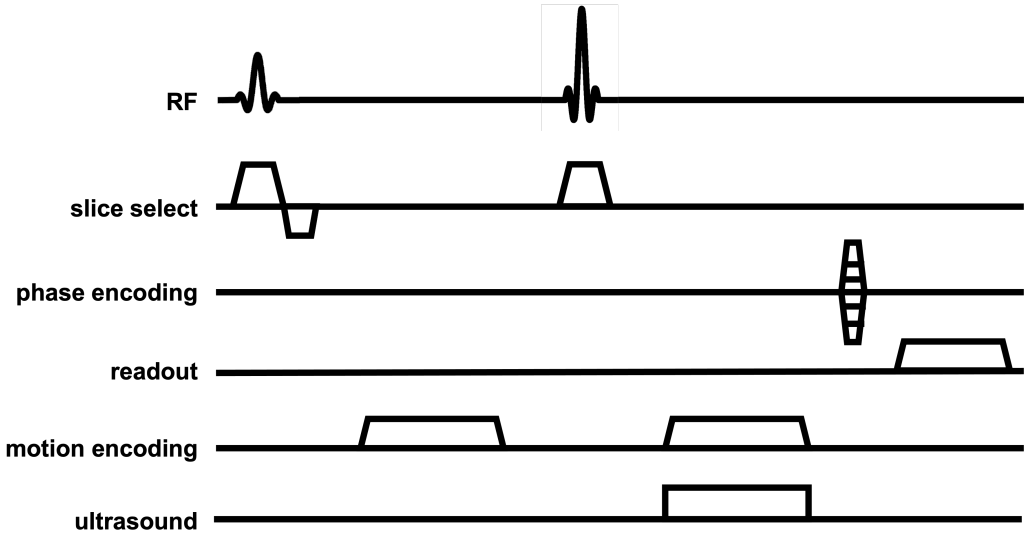

Figure 2.6: Pulse sequence diagram for MR-ARFI spin-echo sequence with a pair of unipolar motion-encoding gradients.

imaging speed and avoid ultrasound-induced heat deposition, EPI readout (Vappou et al., 2018; Hertzberg et al., 2010; Holbrook et al., 2011), spiral readout (Ilovitsh et al., 2019), keyhole (Paquin et al., 2013), partial Fourier sampling and parallel imaging (Odéen et al., 2019; Bour et al., 2018) were reported in 2D applications of MR-ARFI sequence. 3D encoding is less often used because it uses more sonications and needs longer scan times. Some tricks such as using unbalanced gradients (de Bever et al., 2016) and inner volume imaging (Schneider et al., 2013) may reduce 3D scan times and image the FUS beam with contiguous slices. Furthermore, MR-ARFI sequences can be modified to allow simultaneously measure temperature-induced PRF shift and ultrasound-induced displacement, which has been reported in (Auboiroux et al., 2012; Viallon et al., 2010; Qiao et al., 2020).

The MR gradients applied in MR-ARFI for motion encoding can cause diffusion weighting. The SNR of displacement maps is dominated by the tradeoff between displacement encoding sensitivity (α) and the diffusion weighting (b value). For spin-echo sequences, the displacement SNR (SNR_d) calculated by the phase difference of a pair of images is expressed (Chen et al., 2010) as:

$$SNR_d = \sqrt{2}\frac{A}{\sigma} \cdot d\alpha \cdot e^{-bD} e^{(-TE/T_2)} \tag{2.37}$$

where A is the real signal intensity, D is the apparent diffusion coefficient of the voxel, σ is the standard deviation of the gaussian noise. The displacement sensitivity α depends on the gradient strength and the gradient lobe duration δ, that is, $\alpha = 2\gamma G\delta$. The b value of diffusion weighting is determined by the gradient

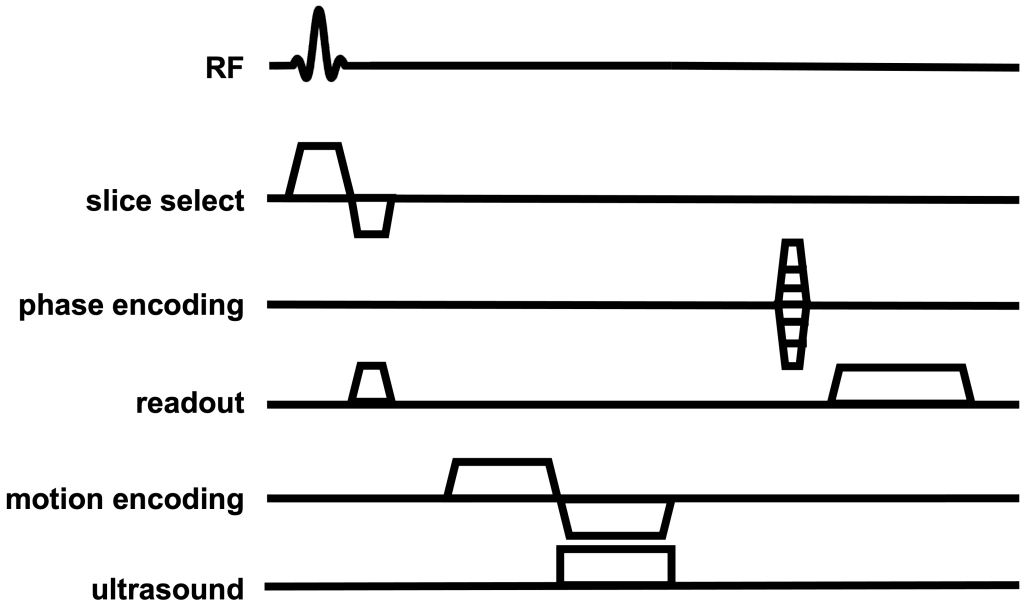

Figure 2.7: Pulse sequence diagram for MR-ARFI gradient-recalled echo sequence with a single bipolar motion-encoding gradient.

strength G, the duration of gradient lobe δ and the time interval Δ between pairs of gradients: $b = \gamma^2 G^2 \delta^2 (\Delta - \frac{\delta}{3})$ for unipolar gradients and $b = \frac{1}{6}\gamma^2 G^2 \delta^2$ for bipolar gradients. If high sensitivity is desired to obtain a higher phase signal, the gradient strength or duration must be increased correspondingly. However, the large gradient strength or the long gradient brings a larger b-value, resulting in low signal intensities. Hence, we should consider the parameters of MEGs carefully when we design MR-ARFI protocols.

MR-ARFI is especially useful for monitoring nonthermal therapies in FUS brain applications since the acoustic waves are shifted and distorted by the skull, and additional energy is not expected for confounding effects. During treatment planning, MR-ARFI can help to verify if the FUS focus is located at the target with little heat induced (Phipps et al., 2019; Gaur et al., 2020) and it can provide the beam information for ultrasonic refocusing in the presence of aberration as well(Hertzberg et al., 2010; Grissom et al., 2012; Mougenot et al., 2016). Apart from FUS localization, MR-ARFI can assess tissue stiffness for ablative applications (Vappou et al., 2018; Hertzberg et al., 2014). It was combined with susceptibility weighted imaging to visualize calcification in ex vivo brain tissue as a clinical indicator for treatment planning in (Bitton and Pauly, 2014).

CHAPTER 3

Rapid quantitative imaging of high intensity ultrasonic pressure fields

3.1 Abstract

High-intensity focused ultrasound (FUS) is a noninvasive technique for treatment of tissues that can lie deep within the body. There is a need for methods to rapidly and quantitatively map FUS pressure beams for quality assurance, and to accelerate development of FUS systems and techniques. However, conventional ultrasound pressure beam mapping instruments including hydrophones and optical techniques are slow, not portable, and expensive, and most cannot map beams at actual therapeutic pressure levels. Here, we report a rapid projection imaging method to quantitatively map FUS pressure beams based on continuous-wave background-oriented schlieren (CW-BOS) imaging. The method requires only a water tank, a background pattern and a camera, and uses a multi-layer deep neural network to reconstruct two-dimensional root-mean-square projected pressure maps that resolve the ultrasound propagation dimension and one lateral dimension. In this work, the method was applied to collect beam maps over a 3×1 cm^2 field-of-view with 0.425 mm resolution for focal pressures up to 9 MPa. Results at two frequencies and comparisons to hydrophone measurements show that CW-BOS imaging produces high-resolution quantitative root-mean-square projected FUS pressure maps in under ten seconds, that the technique is linear and robust to beam rotations and translations, and that it can map aberrated beams.

3.2 Introduction

Focused ultrasound (FUS) is a noninvasive therapeutic modality that has a broad range of established and emerging applications, including tumor (Zhou, 2011), fibroid (Stewart et al., 2003), and desmoid (Ghanouni et al., 2017) ablation, drug delivery (Grüll and Langereis, 2012), brain surgery (Elias et al., 2013a; Ghanouni et al., 2015), blood-brain barrier opening (Lipsman et al., 2018) and neuromodulation (Blackmore et al., 2019). The acoustic waves used in FUS can be focused to a particular location deep in the body, with a spatial resolution on the order of the wavelength of the ultrasound (approximately 1.5 mm at 1 MHz), to thermally or mechanically treat tissues at the focus without affecting intervening tissues. To maximize FUS's therapeutic benefit, it is required to know how much acoustic energy is delivered and where it is delivered, with high spatial accuracy and precision. Furthermore, for therapeutic efficacy and safety it is necessary to assess whether the FUS system output changes between treatments(McDannold and Hynynen, 2006), and to check for system failures which could dangerously alter energy delivery. Experts have recommended that rigorous quantitative pressure beam mapping be performed on clinical systems two to three times monthly(Ter Haar,

2013). For these reasons, the ability to quantitatively map the acoustic pressure beam in two or three spatial dimensions in the clinic is essential, and it is important for the safety and reproducibility of FUS treatments that instruments for rapid field characterization become available. FUS pressure beam mapping is also essential for research and development of new FUS technologies and techniques, such as new therapeutic transducers(Wong et al., 2009), methods to propagate FUS through the skull and other bones(Clement and Hynynen, 2002; Aarnio et al., 2005; Kyriakou et al., 2014), acoustic lenses(Lalonde et al., 1993; Baac et al., 2012; Chang et al., 2014), and FUS-transparent MRI RF coils(Corea et al., 2016). Finally, FUS pressure beam mapping is important for focused imaging transducers, whose output must be characterized to ensure they meet safety guidelines set by the US Food and Drug Administration.

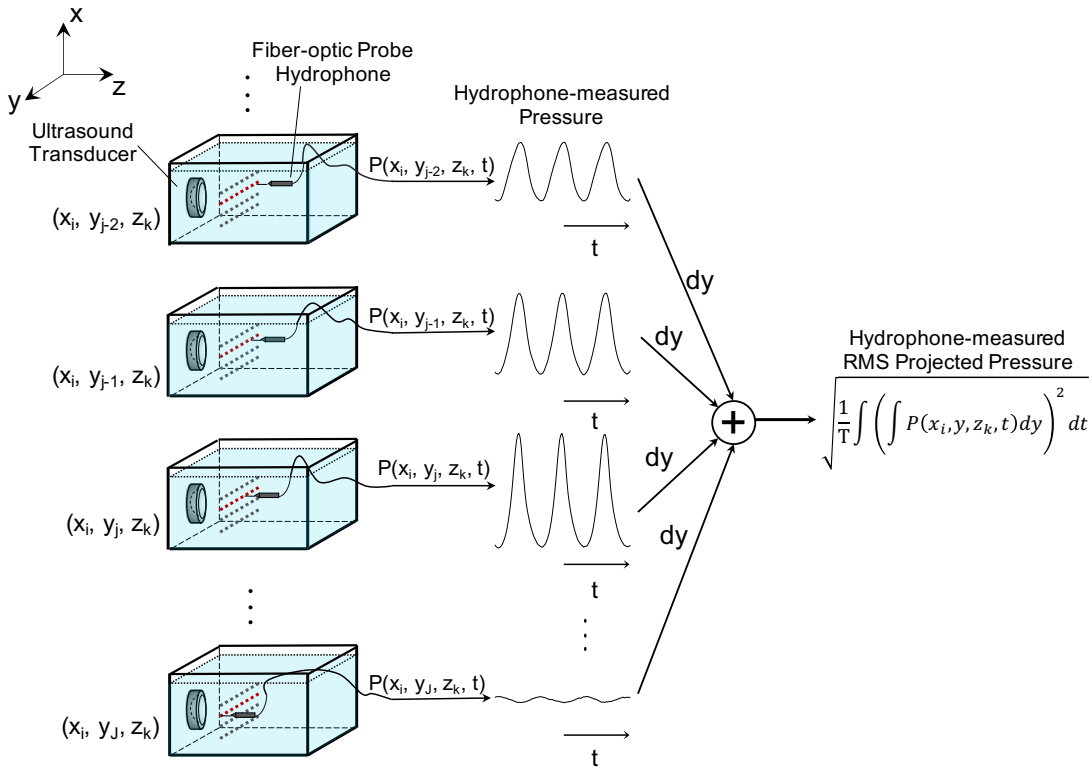

Figure 3.1: 3D ultrasonic pressure beam mapping using a hydrophone probe. The hydrophone probe only samples one spatial location at a time, so it must be translated by a motion stage to obtain a spatially-resolved map, as illustrated by the images on the left. The proposed CW-BOS method produces root-mean-square (RMS) projected pressure beam maps. To obtain the same maps using a hydrophone, 3D hydrophone measurements are integrated along the line-of-sight dimension to obtain projected pressure waveforms, and then the RMS amplitude of the projected waveform is calculated, as illustrated on the right.

The most widely-used FUS pressure beam mapping instruments are hydrophones. They are ill-suited to rapidly mapping the pressure beams produced by FUS transducers, because (as illustrated in Figure 3.1) they only sample one spatial location at a time, and a 3D motion stage must be used to move them through

a tank to produce a spatially-resolved map. This results in long measurement times that even with variable density sampling schemes can take tens of minutes for 2D planes and several hours for 3D volumes, and 1D and 2D hydrophone scans require careful alignment with the ultrasound focus.The long measurement times limit hydrophones' usefulness in measuring beams at multiple power levels or across ranges of experimental variables. Common polyvinylidene fluoride (PVDF) hydrophones are not prohibitively expensive but can only measure sub-therapeutic pressure levels since they are easily damaged by cavitation. To overcome their speed and power limitations, hydrophone measurements can be made at low pressures over a two-dimensional surface close to a transducer, and then serve as source definitions for 3D computational modeling (holography) at different power levels or medium configurations(Canney et al., 2008; Kreider et al., 2013), but these methods still require a large number of hydrophone measurements with a motion stage. Specially designed robust membrane(Bessonova and Wilkens, 2013) and fiber optic hydrophones(Zhou et al., 2006) can withstand higher pressures, but they are more expensive ($>$ \$10k USD) and less sensitive than PVDF hydrophones, and bandwidth limitations at high pressures can be a problem. Any instrument that sits in the focus will experience damage due to cavitation, and will require periodic repair and recalibration, and hydrophone systems with scanning tanks and translation stages lack the portability and ease of setup needed for clinical quality assurance measurements.

Ultrasound pressure beams can also be mapped based on the deflection of light due to the acousto-optic effect, which relates a spatial pressure distribution to index of refraction. Optical ultrasound pressure beam mapping methods such as photographic and laser schlieren methods have been used for more than fifty years to visualize ultrasound pressure fields in two dimensions(Bronson, 1969; Newman, 1973; Smith and Thurstone, 1974; Baborovsky, 1979; Reichel et al., 2005; Zanelli and Howard, 2006; Christensen and Chao, 2007; Johns et al., 2007; Neumann and Ermert, 2006), and laser-based tomographic schlieren methods have been developed for temporally-resolved 3D ultrasound pressure beam mapping(Reichel et al., 2005; Reibold and Molkenstruck, 1984; Hanafy and Zanelli, 1991; Pitts et al., 1994; Charlebois and Pelton, 1995; Schneider and Shung, 1996; Reibold, 1987; Nakamura et al., 2018). The laser-based systems are based on the same physical principle as the technique proposed here, and are capable of impressive spatiotemporal resolution and sensitivity. However, they are limited to small FOVs and are prohibitively expensive ($>$ \$10k USD). Furthermore, to perform 3D mapping they typically require that the transducer itself be rotated, which makes them incompatible with in situ clinical transducers and limits their research utility.

Unlike conventional schlieren systems that require elaborate optical setups involving pulsed light sources, collimating lenses, and filters, background-oriented schlieren (BOS)(Meier, 2002) imaging uses only a camera to image a background pattern through a nonuniform refractive index field. The background pattern is blurred by the nonuniform refractive index field, and cross-correlation of images acquired with and without

the refractive index field in place produces index of refraction maps. In essence, in BOS the conventional sophisticated schlieren optical setup is traded for more sophisticated computation, which is much less expensive and easily replicated. The method has been used tomographically outside of acoustics to map static refractive index fields in 3D(Meier, 2002; Richard and Raffel, 2001; Venkatakrishnan and Meier, 2004; Goldhahn and Seume, 2007; Atcheson et al., 2008, 2009; Tipnis et al., 2013), and it has been used to visualize FUS beams qualitatively in 2D(Butterworth and Shaw, 2010). However, the image formation process in BOS imaging of FUS pressure beams is different from conventional BOS in which the nonuniform refractive index field is static during image acquisition, because the refractive index is proportional to pressure(Waxler and Weir, 1963) which changes dynamically during a typical camera exposure time, so the background image is blurred rather than coherently displaced, and cross-correlation cannot be directly applied to extract refractive index or pressure maps. To freeze time to a fixed phase in the ultrasound cycle, tomographic BOS FUS pressure beam mapping has been performed with a strobed light source(Pulkkinen et al., 2017; Koponen et al., 2019), but these methods have not yet been validated beyond qualitative comparisons to hydrophone measurements, and a strobed light source again complicates the setup and limits signal-to-noise.

Here we describe a rapid projection imaging method to quantitatively map FUS pressure beams based on continuous-wave BOS (CW-BOS) imaging. It requires only a water tank, a background pattern displayed on one side of the tank, and a camera to photograph the pattern through the other side of the tank (Figure 3.2a). The proposed method leverages the recent availability of tablet PCs with high-resolution displays and consumer-grade digital single-lens reflex cameras with high pixel density that can resolve the sub-millimeter blurring of the BOS background pattern at a distance, as well as deep learning techniques that can solve the difficult inverse problem of relating blurred photographs to projected pressure amplitudes. It can be implemented in a small and portable package with no moving parts to rapidly map FUS and focused imaging transducer root-mean-square (RMS) projected pressure beams in 2D, and there are no parts to experience wear from the FUS beam. Illustrated in Figure 3.2b, the background images are bed-of-nails patterns, where each dot is blurred by the ultrasound beam in a distinctive pattern that can be interpreted as a histogram of local image displacement over time and is related to the projected RMS pressure field along the line-of-sight dimension at the position of the dot. An acquisition is performed by taking photographs of blurred background patterns with FUS switched on, and processing them through a deep neural network that relates the blurring pattern at each dot to an RMS projected pressure amplitude. The reconstruction is trained from simulated photographs generated using acoustic simulations of similar FUS transducers. Figure 3.1 defines the RMS projected pressure measurement mathematically, and for illustration shows how the RMS projected pressure amplitude would be obtained using hydrophone measurements with a motion stage. The proposed method produces an RMS projected pressure map in seconds. It was evaluated in experiments using

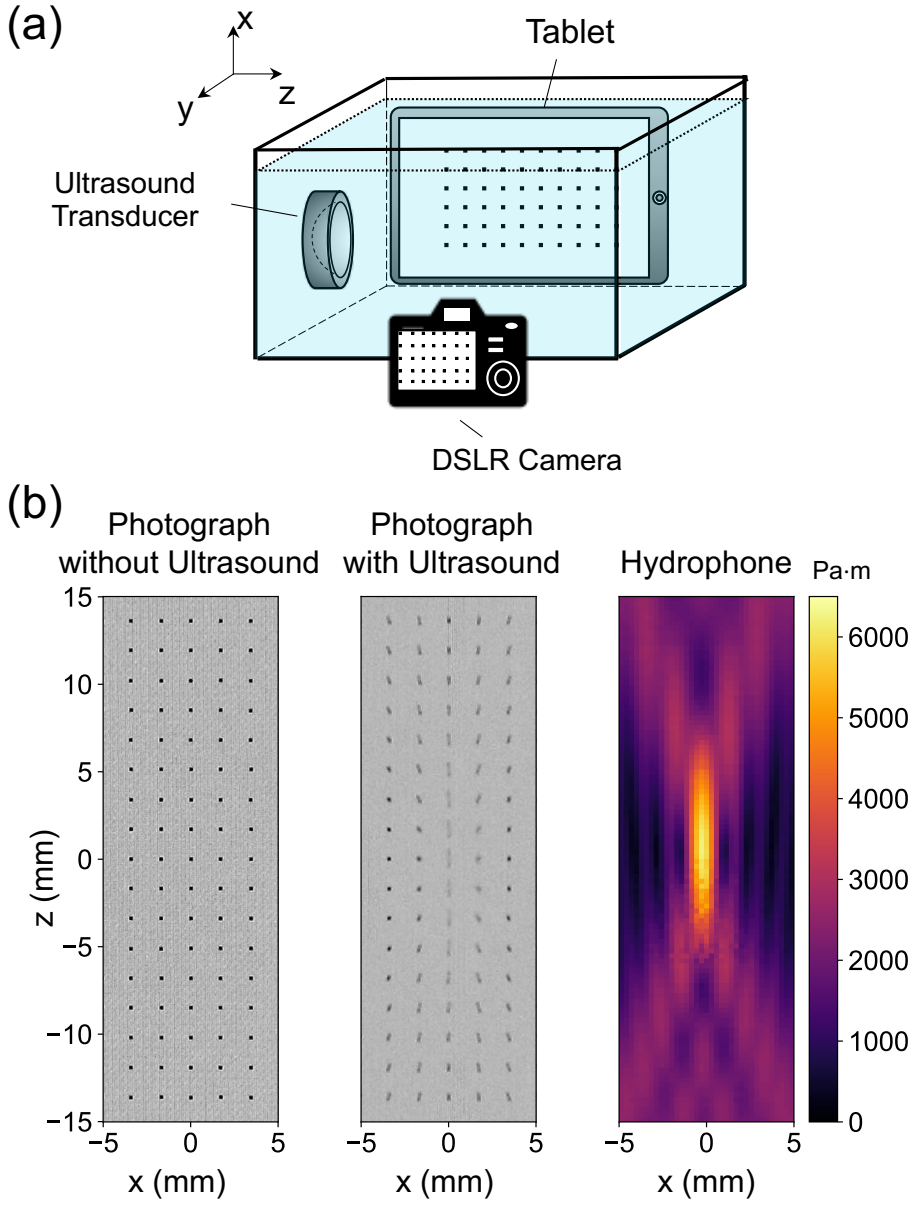

Figure 3.2: The proposed continuous-wave background-oriented schlieren (CW-BOS) projected pressure mapping method displays a bed-of-nails background pattern on one side of a water tank, and photographs it from the other side of the tank. When FUS is switched on, the nails blur in a distinctive pattern that can be related to the projected pressure at each spatial location in the photo. a) A 2D CW-BOS system comprises a glass tank filled with water that is acoustically coupled to the transducer, a tablet displaying a background pattern, and a camera to photograph the blurred pattern. b) Acquired photographs without and with FUS, and a hydrophone-measured RMS projected pressure map of the same FUS beam. In the photographs, the blurred nails are narrower and elongated along the beam propagation direction (bottom to top) in the focus, while the nails are blurred diagonally on either side of the focus. Sound is propagating from bottom to top in these images.

FUS transducers operating at 1.16 and 2.25 MHz, for peak negative pressures ranging from 1 to 4 megapascals (MPa) and associated peak positive pressures ranging from 1.5 to 9 MPa, which overlaps with the range of pressures used in FUS thermal treatments(Ellens and Hynynen, 2014; Wong et al., 2016; White et al., 2008; Poorman et al., 2016) As will be shown, RMS projected pressure follows the contours of the main- and sidelobes of the FUS pressure beam, and is clearly disturbed when the beam is aberrated. The method was implemented and compared to fiber-optic hydrophone RMS projected pressure measurements, to evaluate its feasibility, accuracy and robustness.

3.3 Methods

3.3.1 Optical and FUS Hardware Setup.

Figure 3.3 shows the hardware setup for CW-BOS FUS projected pressure beam mapping, which was built around an ultra-clear rimless water tank (Fragtastic Reef, Mankato, MN, USA) made of 5 mm-thick aquarium-grade glass. The size of the glass tank was $31\times19\times19$ cm^3 (width $\times$ depth $\times$ height), and it was filled with degassed deionized water. To suppress reflections, an acoustic absorber (Aptflex F48, Precision Acoustics Ltd, UK) was placed against the tank wall opposite the FUS transducer. Two FUS transducers were used in this study: a 6.32 cm-diameter 1.16 MHz transducer with focal length 6.3 cm and f-number 1(H101, Sonic Concepts, Bothell, WA, USA), and a 1.91 cm-diameter 2.25 MHz transducer with focal length 5.1 cm and f-number 2.67 (Valpey Fisher IL0206HP, Hopkinton, MA, USA).

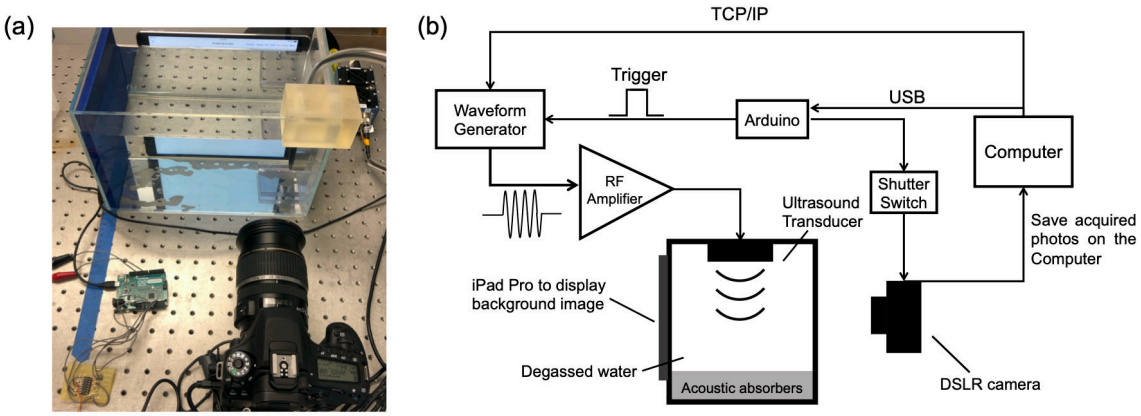

Figure 3.3: a) Photograph of the CW-BOS measurement setup used in this study. The camera is in the lower right and was centered on the nominal FUS beam focus. The iPad was placed against the opposite side of the water tank from the camera, the FUS transducer was mounted on the right side of the tank, and a blue acoustic absorber was mounted on the left side opposite the transducer to suppress reflections. b) Electrical diagram of the setup, including a top-down depiction of the tank. An Arduino was used to open the camera shutter a fixed time period after triggering the waveform generator, so that photos were taken once the FUS beam had reached a steady state. The experiment was coordinated by a MATLAB script which set the waveform generator parameters and initiated an acquisition via the Arduino.

A 10.5” iPad Pro (Apple Inc, Cupertino, CA, USA) was placed against one of the long sides of the tank,

which displayed bed-of-nails background images using a Python script running in the Pythonista app (OMZ Software, Berlin, Germany). The experiment computer told the iPad which background image to display via TCP/IP commands sent over WiFi. An EOS 80D 24.2 megapixel digital single-lens reflex (DSLR) camera with an EF-S 17-55mm f/2.8 IS USM lens (Canon Inc, Tokyo, Japan) was placed so that its body was 20 cm from the outer wall of the tank opposite the iPad, and the aperture was 12 cm from the outer wall of the tank. The camera was connected to the experiment computer via USB. The EOS Utility software (Canon Inc, Tokyo, Japan) was used to control the camera's settings and download photos from it. An Arduino Leonardo R3 microcontroller board (Arduino, Italy) was used to open the camera shutter a fixed delay period after triggering the waveform generator, so that photos were taken once the FUS beam had reached a steady state (timing described further below). The Arduino controlled the shutter via an analog switch (CD74HC4066E, Texas Instruments, Dallas, TX, USA) which electrically closed two switches (focus and shutter) of a modified wired manual shutter release that was connected to the N3 connector of the camera, and it sent a TTL trigger to the external trigger port of the FUS waveform generator (Keysight 33500B series, Santa Rosa, CA, USA) to initiate the ultrasound pulse. The waveform generator's parameters were set using TCP/IP commands sent from the computer via an ethernet connection, and its output was connected to an E&I A-150 amplifier (E&I Ltd, Rochester, NY, USA) with 55 dB gain to drive the transducer.

3.3.2 CW-BOS Acquisition Details

Acquisitions were initiated by the experiment computer. When instructed by the computer, the Arduino opened the camera shutter, waited 50 ms, and then sent a TTL pulse to the waveform generator to generate a 100,000-cycle, 86 ms pulse at 1.16 MHz, and a 150,000-cycle, 67 ms pulse at 2.25 MHz. The 50 ms delay was set based on an observed 75-100 ms delay between when the Arduino commanded the shutter to open and when it actually opened, and the pulse durations were set long enough to accommodate some variability in the shutter delay while ensuring that photos were captured when the pressure field was at steady state. Using a shorter delay caused the shutter to sometimes open after the pulse had already shut off. The camera settings were: image size 4000×6000 pixels, ISO 640, shutter speed 1/800 s (1.25 ms), f-number f/5. The photographs were saved on the computer in the RAW image format. The shutter speed corresponded to 1,450 cycles for the 1.16 MHz transducer, and 2,813 cycles for the 2.25 MHz transducer. During the experiments, the whole measurement setup was covered by a black cloth to suppress ambient light, so the iPad provided the only illumination.

The background images displayed by the iPad were bed-of-nails patterns comprising black dots/nails on a regular grid with a white background. The size of each dot was 2 pixels × 2 pixels. The distance between consecutive dots in each direction was 16 pixels, which corresponded to a physical distance of 1.7 mm,

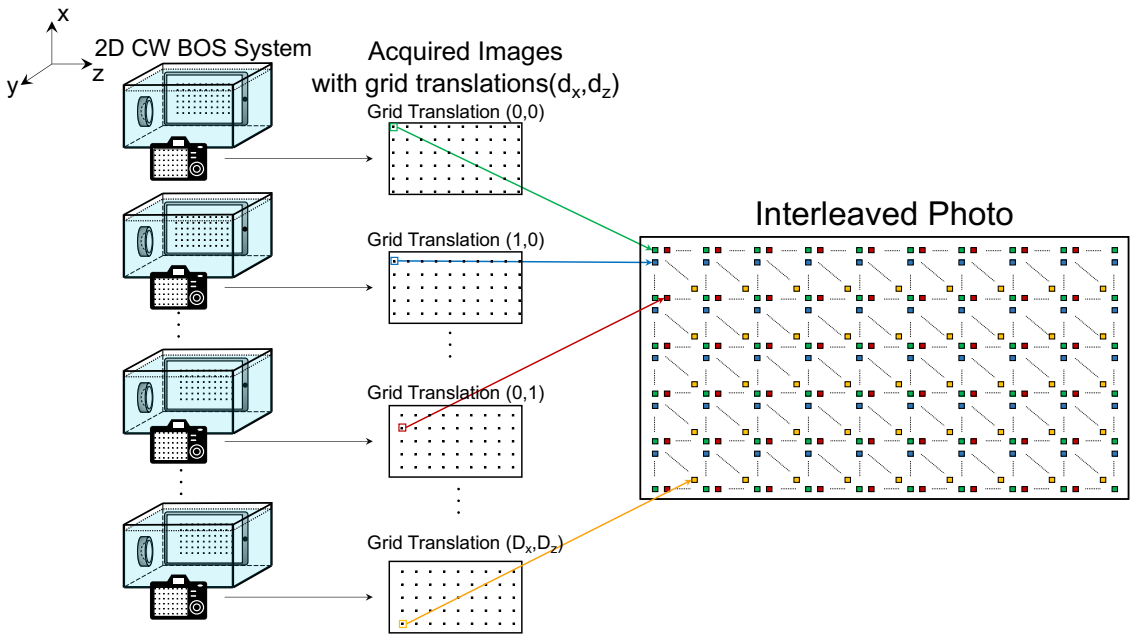

Figure 3.4: To measure high-resolution RMS projected pressure maps, multiple CW-BOS photos were collected over a range of grid translations in the x and z directions. The reconstructed RMS projected pressure values were then tiled into the final map.

and was set based on the maximum expected displacement in the experiments. To obtain a high-resolution projected pressure map, the background image was moved in intervals of 4 pixels in the x and z dimensions as illustrated in Figure 3.4, and a total of 16 photos were acquired, one for each image position. A single high-resolution (0.425 x 0.425 mm^2) RMS projected pressure map was calculated from the 16 photos as described below.

The following acquisitions were performed to evaluate the proposed CW-BOS RMS projected pressure beam mapping method:

- **Two FUS Frequencies.** FUS frequencies range from hundreds of kHz to several MHz. To demonstrate the CW-BOS method at different frequencies, mapping was performed with the 1.16 and 2.25 MHz transducers and compared to optical hydrophone measurements. The waveform generator voltages (before 55 dB power amplifier gain) were 200 millivolts peak-to-peak (mV_{pp}) (1.16 MHz) and 100 mV_{pp} (2.25 MHz). The acquisitions were repeated five times for averaging.

- **Pressure Amplitude.** To evaluate the method across a range of pressure amplitudes, photos were acquired with the 1.16 MHz transducer with waveform generator voltages between 0 and 200 mV_{pp}, in 25 mV_{pp} steps. The acquisitions were repeated five times for averaging.

- **Signal-to-Noise ratio (SNR) and Number of Averages.** To investigate how the number of signal

averages (NSA) affects the SNR of CW-BOS maps, an acquisition was repeated ten times with the 1.16 MHz transducer and waveform generator voltages of 50, 100, 150, and 200 mV_{pp}. Each acquisition was reconstructed separately to an RMS projected pressure map which was then averaged with other reconstructions at the same generator voltage.

- **Rotation and Translation.** User error could introduce rotations and displacements between the camera and the FUS beam, so CW-BOS should be robust to a reasonable range of such errors. To verify the robustness to beam rotations, five averages were acquired with the 1.16 MHz transducer rotated by 15° and 30° about the line-of-sight axis, with a waveform generator voltage of 200 mV_{pp}. Five more averages were acquired with the camera translated +2.5 cm and -2.5 cm along the z-dimension to verify the robustness to beam translations, with a waveform generator voltage of 150 mV_{pp}.

- **Aberrations.** An important potential application of the method is to detect aberrations and measure aberrated beams in research and the clinic. To verify the ability of CW-BOS to detect aberrated beams, an acoustic aberrator(Maimbourg et al., 2018) made from silicone (Elite double 8, Zhermack, Badina Polesine, Italy) was constructed and placed against the bottom half or the left half of the transducer to aberrate the pressure field in the *x*-*z* plane or the *y*-*z* plane, respectively. This material was chosen based on previous experience that it can be molded into the transducer's shape and used to aberrate beams without heating the transducer, and that it stays on the transducer surface when submerged in water. Five averages were acquired for each of these two cases with the 1.16 MHz transducer and waveform generator voltages of 200 mV_{pp}.

The acquired photos were segmented into small rectangular patches around each dot using MATLAB's `bwmorph()` function (Mathworks, Natick, MA, USA), then the RMS projected pressure was calculated by the neural network for each dot as described below, and those values were tiled into the final reconstructed beam map. With the camera placed a total distance of 31 cm from the iPad, each rectangular patch comprised between 42×42 and 46×46 pixels, and was upsampled to 54×54 pixels for reconstruction. To avoid optical color dispersion, only the green channel from the photos was used for reconstruction, which has the largest weight among red, green, and blue channels in the Rec.ITU-R BT.601-7(BT et al., 2011) video standard's luminescence calculation ($0.299R + 0.587G + 0.114B$). The total scan time for 5 averages was 3-5 minutes and was dominated by the time taken for data transfer from the camera to PC. Without these delays, the total scan times were approximately 8 seconds (16 photos × 100 ms of FUS on-time × 5 averages).

3.3.3 Optical Hydrophone Measurements

For validation, pressure maps were also measured using calibrated fiber-optic hydrophone sensors (136-10T and 132-03, Precision Acoustics Ltd, UK) connected to a fiber-optic hydrophone system control unit (Morris et al., 2009). The hydrophone measurements were performed in the same water tank as CW-BOS, using a Picoscope (Model 5242B, Pico Technology, UK) to record data from the output of the system control unit to the computer, and a 3D motion stage (Image Guided Therapy, Bordeaux, France). The motion stage and the Picoscope were both controlled by the experiment computer via USB. The motion stage was fully stopped at each spatial location prior to recording. A 100-cycle pulse was generated by the waveform generator for both 1.16 MHz and 2.25 MHz measurements to produce enough cycles for which the waves from each part of the transducer had reached the measurement volume. The measured voltage waveforms were converted to pressure by multiplying them by the probe sensitivities given below. As illustrated in Figure 3.1, to calculate reference RMS projected pressure maps from the hydrophone data, the synchronized hydrophone measurements were integrated along the line-of-sight (y) dimension to calculate the projected pressure waveforms and RMS projected pressure, using five cycles which were extracted from the hydrophone measurements at a time when the amplitudes at all measurement positions in the 3D volume were stable. The 1.16 MHz maps were measured over a $10\times10\times30$ ($x \times y \times z$) mm^3 volume with waveform generator voltages of 200 mV_{pp} and step sizes of 0.25 mm in x and y, and 0.25 mm in z. The 132-03 probe was used for the 1.16 MHz measurements, and had a sensitivity of 162.27 mV/MPa and a background noise standard deviation of 5.4 mV. The 2.25 MHz map was measured over a $10\times10\times47.5$ mm^3 volume with waveform generator voltages of 100 mV_{pp} and step sizes of 0.25 mm in x and y and 0.5 mm in z. The 136-10T probe was used for the 2.25 MHz measurements, and had a sensitivity of 118.05 mV/MPa and a background noise standard deviation of 3.5 mV. One-dimensional hydrophone measurements were also taken along z with a 0.25 mm step size through the 1.16 MHz transducer's focus with waveform generator voltages of 50, 100, 150, and 200 mV_{pp}, for comparison with CW-BOS acquisitions across pressure amplitudes.

3.3.4 Mathematical Model for CW-BOS Imaging of FUS Pressure Fields.

Figure 3.2a shows that when a background image displayed by the tablet is photographed through the water tank by the camera, the image is distorted due to the refraction of light rays as they travel through the water from the tablet to the camera lens. The refraction angle in each of the photographed dimensions (x and z) is

determined by the refractive index of the water:

$$\varepsilon_x = \frac{1}{n_0}\frac{\partial}{\partial x}\int n(x,y,z,t)dy$$
$$\varepsilon_z = \frac{1}{n_0}\frac{\partial}{\partial z}\int n(x,y,z,t)dy \tag{3.1}$$

where n_0 is the ambient refractive index of water, n is the 3D refractive index field, and y is the projected (line-of-sight) dimension. The 3D refractive index field (n) is proportional to the acoustic pressure p(Waxler and Weir, 1963):

$$n(x,y,z,t) = n_0 + \frac{\partial n}{\partial p}p(x,y,z,t), \tag{3.2}$$

where $\frac{\partial n}{\partial p} = 1.4636 \times 10^{-11}$ Pa^{-1} is the adiabatic piezo-optic coefficient(Raman and Venkataraman, 1939; Riley and Klein, 1967). Assuming the light ray is deflected as it passes through the FUS beam's refractive index field and then continues across a distance D in the y dimension before being recorded by the camera, the image displacement at a location (x,z) in the photograph of the tablet's image is obtained by substituting Equation 3.2 into Equation 3.1 and scaling by D:

$$d_x = K\frac{\partial}{\partial x}\int p(x,y,z,t)dy$$
$$d_z = K\frac{\partial}{\partial z}\int p(x,y,z,t)dy, \tag{3.3}$$

where $K = \frac{D}{n_0}\frac{\partial n}{\partial p}$. In this equation, the integral of the 3D pressure field along the projected dimension (y) is the projected pressure field $P_{proj}(x,z,t)$. This forward model was used to calculate simulated CW-BOS histograms to train the neural network reconstructor as described below.

3.3.5 Numerical FUS Beam Simulations and Training Data Generation.

To generate the FUS-blurred background images used to train the reconstructor, spatially- and temporally-resolved steady-state FUS pressure fields with nonlinearity were simulated using a modified angular spectrum method(Tripathi et al., 2019) with frequency domain attenuation and dispersion, absorbing boundary layers, and an adaptive propagation step size. An operator splitting term was used to separate the terms in the retarded-time formulation of the nonlinear angular spectrum equation(Dagrau et al., 2011). The attenuation and dispersion term was solved directly in the frequency domain using a filtering approach. The nonlinear term was solved in the time domain using a Rusanov scheme to accurately capture the shock front in a flux-conservative fashion(Rusanov, 1970). While the dispersion modeling performed by this general simulation tool was not necessary in water, the attenuation modeling is important to correctly describe the shock wave

physics, particularly at high frequencies. Without it, simulated shock rise times would be significantly larger than reality. A dispersionless boundary with a quartic increase in attenuation was implemented at the boundaries over a region of 10λ. This absorbing boundary layer was placed 20λ away from the outermost edges of the active transducer area so it would not affect the wave propagation in the transducer footprint. This simulation method has been validated experimentally (Pinton, 2007). The simulations used a speed of sound in water of $c_0 = 1500$ m/s, $\lambda/8$ grid spacing in the dimensions transverse to beam propagation (0.16 mm at 1.16 MHz and 0.08 mm at 2.25 MHz), $\lambda/4$ grid spacing in the axial/propagation dimension (0.32 mm at 1.16 MHz and 0.17 mm at 2.25 MHz), a nonlinearity coefficient of $\beta = 3.5$, an equilibrium density $\rho_0 = 1000$ kg/m^3, and a dwell time (temporal step size) of $1/(40 f_0)$ (21.5 ns at 1.16 MHz and 11.1 ns at 2.25 MHz). The beams were simulated over a 9.5×9.5×9.5 cm^3 volume for the larger 1.16 MHz transducer and a 2.86×2.86×7.6 cm^3 volume for the smaller 2.25 MHz transducer. The simulated transducers generated Hamming-windowed 48-cycle pulses, and the middle cycle was saved at each spatial location, representing steady-state. A total of 34 simulations were run for the 1.16 MHz transducer, for focal peak negative pressures (PNPs) between 1 - 11.5 MPa, associated focal peak positive pressures (PPPs) between 1.2 - 21.5 MPa, and f-numbers of 0.5 (focal length = 3.2 cm) and 1 (focal length = 6.3 cm). A total of 36 simulations were run for the 2.25 MHz transducer, for focal PNP between 0.9 - 9.7 MPa, associated focal PPP between 1.3 - 9.7 MPa, and f-numbers of 1.335 (focal length = 2.5 cm) and 2.67 (focal length = 5.1 cm).

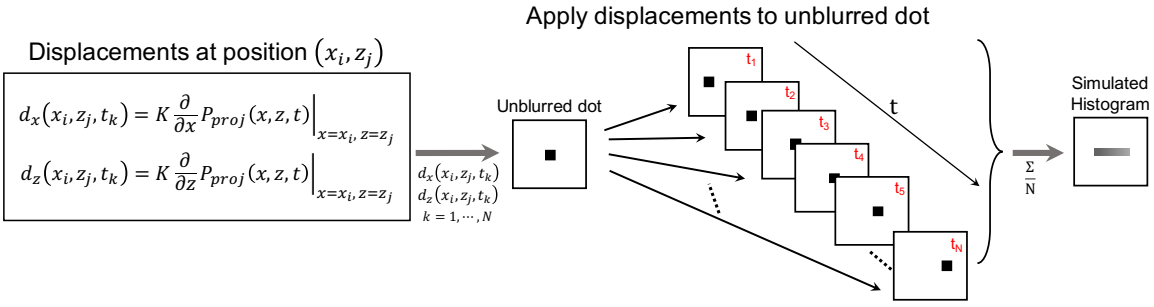

Figure 3.5: Simulated histogram calculation procedure. The background image displacements at position (x_i, z_j) in a simulated FUS pressure field were calculated using the projected pressure waveforms and applied to the unblurred dot to shift it in x and z for each simulated time point t_k. Then, the displaced dot patterns were averaged over one ultrasound cycle to obtain the 2D histogram.

The training data for the reconstructor comprised simulated CW-BOS histograms paired with their RMS projected pressure amplitudes. First, projected pressure waveforms were calculated by integrating the beams along the y dimension, and RMS projected pressure amplitudes were calculated from those waveforms. Then the associated histograms were calculated as illustrated in Figure 3.5. To calculate a histogram for each simulated (x, z) location, projected pressure waveforms were first calculated, then image displacements were calculated using Equation 3.3, which required finite differencing the y-projected pressure fields in the x and

z dimensions and scaling the result by the distance D between the focus and the tablet screen (D = 8.5 cm for our hardware setup). Then, for each time instant, a distorted image was computed by shifting the spatial location's dot by the calculated image displacements in each direction, and the distorted images were averaged over one ultrasound period to obtain a final simulated BOS histogram image. The simulated histograms were convolved with a point spread function measured from an undistorted (no-FUS) photograph taken with our system. The histograms were individually normalized for zero mean and unit standard deviation, and the RMS projected pressures were collectively normalized. The histogram dimensions were 54×54, which corresponded to a spatial area of size 1.7 × 1.7 mm^2 on the screen of the tablet, with a pixel width of 0.024 mm. The 1.16 MHz training data comprised a total of $N = 923174$ examples, and the 2.25 MHz training data comprised a total of $N = 1777987$ examples.

Prior to inputting them to the reconstructor network, the training histograms were compressed to a dimensionality smaller than their number of pixels by projecting them to a subspace derived by singular value decomposition (SVD) truncation(McGivney et al., 2014; Turk and Pentland, 1991). For each FUS frequency, a dictionary was formed from all the training data by reshaping the histograms to length-M row vectors $\mathbf{d} \in R^{1\times M}$, where $M = 54^2 = 2916$, and stacking them into a dictionary matrix $\mathbf{D} \in R^{N\times M}$, where N is the number of training examples. The matrix $\mathbf{D}$ was decomposed by SVD into the product of three matrices, $\mathbf{D} = \mathbf{USV}^T$, where $\mathbf{U} \in R^{N\times M}$ is an orthonormal matrix containing the left singular vectors, $\mathbf{S} \in R^{M\times M}$ is a diagonal matrix containing the singular values, and $\mathbf{V} \in R^{M\times M}$ is an orthonormal matrix of right singular vectors. A lower dimensional compressed subspace was obtained by truncating the SVD to its first K singular values (K = 137 at 1.16 MHz and 97 at 2.25 MHz, where K was set to retain 99.999% of the sum-of-squared singular values compared to no truncation), and the vectors of the resulting truncated right singular vector matrix $\mathbf{V}_K \in R^{M\times K}$ spanned this lower-dimensional subspace. Thereafter, each training and experimental BOS histogram $\mathbf{d}$ was projected to the lower-dimensional subspace by multiplying it with the matrix $\mathbf{V}_K$ to obtain its compressed coefficients $\mathbf{c} = \mathbf{dV}_K$. The coefficient vector $\boldsymbol{c}$ was the input to the neural network which output the RMS projected pressure value corresponding to that histogram, as illustrated in Figure 3.6 and described further below. The matrices $\mathbf{V}_K$ were stored and used to compress experimentally measured histograms prior to reconstruction of their RMS projected pressures.

3.3.6 Neural Network Architecture and Training.

To reconstruct RMS projected pressure maps from a set of photographs, Figure 3.6 shows that each histogram is projected into the compressed SVD subspace, and the resulting length-K vector of coefficients $\mathbf{c}$ is input to a deep neural network comprising three fully connected layers (FC1 to FC3 in Figure 3.6). The input and fully connected layers all have K nodes, and each is followed by a hyperbolic tangent activation function.

The output layer comprises a linear activation function and has one node, the output of which is the RMS projected pressure for the input histogram coefficients.

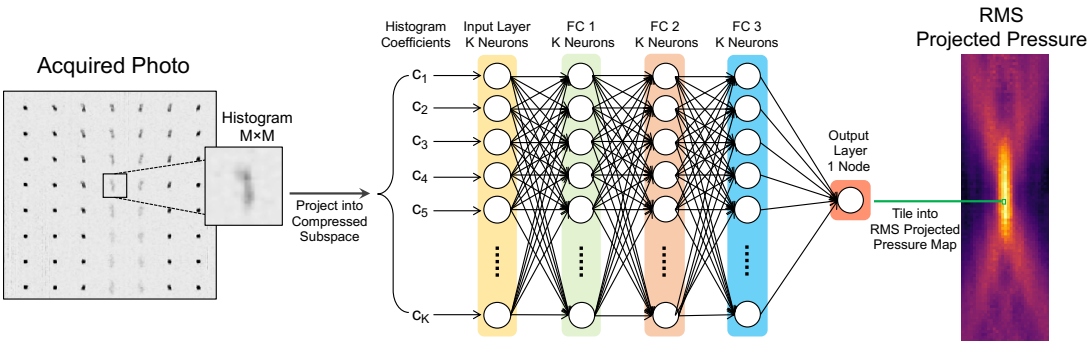

Figure 3.6: Schematic representation of neural network-based pressure reconstruction for each photographed histogram. Each histogram in a photo is segmented into an $M \times M$ sub-image, and then projected to the compressed subspace, and its K ($K \ll M$) coefficients in that subspace are input to a deep neural network with a fully-connected input layer and three fully-connected hidden layers and hyperbolic tangent activations, which feed a single-node layer that outputs the final estimated RMS projected pressure value, which is tiled into the final beam map.

A network was trained for each frequency using the simulated histograms and their associated RMS projected pressures in Keras(Chollet et al., 2015) on the Tensorflow deep learning framework(Abadi et al., 2016) using two NVIDIA graphics processing units (NVIDIA, Santa Clara, CA, USA) for 20 epochs (approximately 1 hour), on Vanderbilt University's parallel computing cluster (Advanced Computing Center for Research and Education, Vanderbilt University, Nashville, TN). Each batch was trained for 400 steps. The optimization algorithm RMSProp(Tieleman and Hinton, 2012) was used with mini-batches of size 1024, a learning rate of 0.00005, momentum 0.0 and decay 0.9. Mean squared error was used as the loss function for training. An additional L_1-norm penalty ($\lambda_1 = 0.00002$) was used to promote sparsity of the weights in the input layer, and an L_2-norm penalty ($\lambda_2 = 0.0002$) was used to prevent overfitting in each layer. Keras's real-time augmentation was used to rotate the training histograms by 0°- 30° to achieve robustness to transducer rotations. The final network weights occupied 662 kB disk space for the 1.16 MHz transducer, and 230 kB disk space for the 2.25 MHz transducer; the sizes differed due to the different sizes of the SVD-compressed subspaces for each frequency. Given all the acquired photos, the beam map reconstructions each took approximately 20 seconds of computation on a desktop computer with a 4.2 GHz Intel Core i7 CPU and 32 GB 2400 MHz DDR4 RAM (iMac, Apple Inc, Cupertino, CA, USA).Note that while hydrophone measurements were used to evaluate the proposed method, they are not required and were not used to calibrate or train it.

3.4 Results

3.4.1 Comparison of FUS Beam Simulations and Hydrophone Measurements

Figure 3.7 shows a comparison of simulated and hydrophone-measured 1.16 MHz PNP maps in *x*-*y* and *x*-*z* planes that cut through the transducer's focus. The hydrophone measurements were taken with a waveform generator voltage of 200 mV_{pp}, and the simulated transducer's source amplitude was adjusted to match the hydrophone-measured focal PNP (4.38 MPa). Table 3.1 lists measured amplitudes and main lobe widths for the simulated and measured beams, which correspond closely, supporting the use of the simulations to train the CW-BOS reconstruction network.

Table 3.1: Quantitative comparisons of simulated and hydrophone-measured 2D pressure fields at 1.16 MHz.

	Simulation	Hydrophone
Focal PNP (MPa)	4.38	4.39
Focal PPP (MPa)	8.04	8.03
PNP Main-lobe FWHM[1] (*x* axis, mm)	2.3	2.2
PNP Main-lobe FWHM[1] (*y* axis, mm)	2.2	2.2
PNP Main-lobe FWHM[1] (*z* axis, mm)	16.2	14.6

3.4.2 Two FUS Frequencies

The hydrophone-measured peak negative pressures produced at 1.16 and 2.25 MHz were 4.5 and 1.4 MPa, respectively, and the peak positive pressures were 8.0 and 2.7 MPa, respectively. Figure 3.8a shows the hydrophone-measured RMS projected pressure map (left), the reconstructed CW-BOS RMS projected pressure map (middle), and their difference (right) for the 1.16 MHz transducer. The amplitudes and shapes of the hydrophone and CW-BOS beams matched closely, with a root-mean-squared error (RMSE) of 316 Pa·m calculated over the whole 2D maps, or 5.1% of the hydrophone-measured peak amplitude, and the difference in spatial peak projected pressure was 239 Pa·m (3.8% of the hydrophone-measured spatial peak). The main-lobe FWHMs were 1.5 mm (hydrophone) versus 1.5 mm (CW-BOS) in the *x* dimension (perpendicular to the beam axis), and 11.4 mm (hydrophone) versus 11.3 mm (CW-BOS) in the *z* dimension (parallel to the beam axis). Figure 3.8b shows the hydrophone (left) and CW-BOS (middle) RMS projected pressure maps and their difference (right), for the 2.25 MHz transducer. The RMSE between the two was 209 Pa·m, or 8.6% of the hydrophone-measured peak amplitude, and the difference in spatial peak projected pressure was 29 Pa·m (0.1% of the hydrophone-measured spatial peak). The main-lobe FWHMs in *x* were 2.1 mm (hydrophone) versus 1.8 mm (CW-BOS), and the main-lobe full width at 75% of maximums in *z* were 31.2 mm (hydrophone) versus 32.2 mm (CW-BOS). Table 3.2 summarizes these comparisons. The total hydrophone scan times to generate these maps were approximately 6.7 hours for the 1.16 MHz transducer (200,000 spatial locations) and 5.5 hours for the 2.25 MHz transducer (160,000 spatial locations).

Table 3.2: Quantitative comparisons of hydrophone and CW-BOS measured RMS projected pressure maps.

	1.16MHz		2.25MHz	
	Hydrophone	CW-BOS	Hydrophone	CW-BOS
RMSE[1] (Pa·m)	316		191	
Percentage RMSE[2] (%)	5.1%		8.6%	
RMS projected pressure amplitude in the focus (Pa·m)	6003	6242	2424	2453
Main-lobe full-width at 50% maximum (x axis, mm)	1.5	1.5	2.1	1.8
Main-lobe full-width at 50% (or 75%) maximum (z axis, mm)	11.4 (50%)	11.3 (50%)	31.2 (75%)	32.2(75%)

3.4.3 Pressure Amplitude.

Figure 3.9a shows reconstructed RMS projected pressure maps across waveform generator driving voltage amplitudes. Figure 3.9b plots the mean across five averages of the RMS projected pressure in the focus (indicated by the arrow in Figure 3.9a) at each amplitude, along with optical hydrophone measurements which were taken at waveform generator voltages of 50, 100, 150, and 200 mV_{pp}. The error bars represent the standard deviation of the values over the five averages. The fitted slopes of the RMS projected pressure amplitudes were 32.2 Pa·m/mV_{pp} (hydrophone) versus 32.3 Pa·m/mV_{pp} (CW-BOS). The Pearson's r-value between the hydrophone and CW-BOS measurements was 0.996. Figure 3.9c plots pressure waveforms measured by the optical hydrophone at the focus. For waveform generator amplitudes of 50, 100, 150, and 200 mV_{pp}, the focal PNPs measured from those waveforms were 1.5, 2.5, 3.6, and 4.5 MPa, respectively, and the PPPs were 1.7, 3.7, 6.4, and 9.2 MPa, respectively.

3.4.4 Signal-to-Noise Ratio and Number of Averages.

Figure 3.10 shows that noise is reduced by averaging reconstructions from repeated CW-BOS acquisitions. Figure 3.10a shows reconstructed CW-BOS RMS projected pressure maps resulting from powers-of-two averages from one to eight (1, 2, 4, and 8), for a waveform generator voltage of 200 mV_{pp}. The map resulting from eight averages is the maximum shown in Figure 3.10a, which was indistinguishable from the map resulting from the maximum ten averages (not shown). The maps became smoother as noise was reduced with increased averaging. Figure 3.10b plots the decremental RMS error in a 5.6×20 mm^2 region centered on the focus between maps reconstructed from one to ten averages, for each waveform generator voltage amplitude. The differences stopped changing significantly after five averages. Figure 3.10c plots the incremental SNR around the focus of reconstructed 200 mV_{pp} maps with one to ten averages; with one acquisition the SNR was 50, but was improved to 80 by five averages. Here, SNR was calculated as the ratio of the signal amplitude in the middle of the focus to the standard deviation in background regions without significant projected pressure.

SNR was improved by 30 (approximately 60%) with five averages, and was improved by only another 10 with ten averages (approximately 10%). For this reason, five averages were used for the other experiments. The SNR of the hydrophone RMS projected pressure map of the 1.16 MHz transducer at 200 mV_{pp} was 407, supporting the use of hydrophone measurements as references for CW-BOS validation.

3.4.5 Rotation and Translation.

Neural networks were trained without and with rotated beams. Figure 3.11a shows CW-BOS RMS projected pressure maps imaged with a 200 mV_{pp} waveform generator voltage, with no transducer rotation (the reference case), and 15° and 30° rotation about the *y* (line-of-sight) axis, where the reconstruction was done using the network that was not trained with rotated beams. The figure shows that the intensity of the rotated pressure fields are different than the reference: the RMS projected pressure amplitudes in the focus were 6007 Pa·m (0°), 5704 Pa·m (15°; 4.0% difference with respect to 0°) and 5184 Pa·m (30°; 13.7% difference with respect to 0°). Figure 3.11b shows reconstructions using the network that was trained with rotated beams, and the shape and intensity of the rotated pressure fields are much closer to the reference: the RMS projected pressure amplitudes in the focus were 6036 Pa·m (0°), 6292 Pa·m (15°; 4.2% difference with respect to 0°) and 6266 Pa·m (30°; 3.8% difference with respect to 0°). FWHMs measured perpendicular to the beam axis were 1.5 mm (0°), 1.7 mm (15°) and 1.4 mm (30°), and FWHMs measured parallel to the beam axis were 11.5 mm (0°), 12.1 mm (15°), and 11.2 mm (30°). Figure 3.11c further shows CW-BOS RMS projected pressure maps measured with the camera translated ±2.5 cm along the z-dimension, with a 150 mV_{pp} waveform generator voltage. The intensity and shape of pressure fields were again unchanged compared to the reference. The projected pressure amplitudes around the focus were 4419 Pa·m (no translation), 4587 Pa·m (-2.5 cm) and 4378 Pa·m (+2.5 cm). The differences of the amplitudes around the focus compared to the reference (0 cm) were 3.8% (-2.5cm) and 0.9% (+2.5cm) of the amplitude with the camera translated 0 cm. FWHMs in the *x* dimension (perpendicular to the beam axis) were 1.5 mm (no translation), 1.6 mm (-2.5 cm and +2.5 cm), and 12.2 mm (no translation), 12.7 mm (-2.5 cm), and 14.0 mm (+2.5 cm) in the *z* dimension (parallel to the beam axis). These comparisons are summarized in Table 3.3.

3.4.6 Aberrations.

Figure 3.12a shows the silicone acoustic aberrator made placed against the bottom half of the 1.16 MHz transducer to aberrate the pressure field in the *x*-*z* plane. CW-BOS RMS projected beam maps, hydrophone beam maps measured with this aberrator configuration, and their difference are shown in Figure 3.12b. The beams' intensities and shapes agree qualitatively and exhibit similar characteristics, and the RMSE between them was 257 Pa·m (10.8% of the hydrophone-measured peak amplitude at x = -2.7 mm, z = -9.5 mm). The

Table 3.3: Quantitative comparisons of CW-BOS pressure maps with the transducer rotated or the camera translated.

	Rotations			Translations		
	0°	15°	30°	0 cm	-2.5 cm	2.5 cm
RMS projected pressure amplitude in the focus (Pa·m)	6036	6292	6266	4419	4587	4378
% error in the focus		4.2%	3.8%		3.8%	0.9%
FWHM[1] (*x* axis, mm)	1.5	1.7	1.4	1.5	1.6	1.6
FWHM[1] (*z* axis, mm)	11.5	12.1	11.2	12.2	12.7	14.0

difference in the peak projected pressure is 141 Pa·m (6.0% of the hydrophone-measured peak amplitude). Figure 3.12c further shows the aberrator placed against the left half of the transducer to aberrate the pressure field in the *y*-*z* plane, and Figure 3.12d shows measured beam maps with this configuration. The maps show similar features, with an RMSE of 380 Pa·m (19.3% of the hydrophone-measured peak amplitude at x = -0.1 mm, z = 5.1 mm). The difference in the peak RMS projected pressure is 236 Pa·m (11.7% of the hydrophone-measured peak amplitude).

3.5 Conclusions

Quantitative and fast mapping of FUS pressure fields is essential for treatment planning, safety, dosimetry, quality assurance and technical research(Ter Haar, 2013). We have proposed and demonstrated a rapid and inexpensive optical projection imaging method that quantitatively maps FUS pressure fields in two dimensions, and requires only a water tank, a tablet to display background patterns, a camera and a PC to reconstruct RMS projected pressure maps. While there are therapeutic ultrasound applications such as histotripsy that use pressures higher than the peak negative pressures in our study, thermal ablation is performed using pressures within the range we studied(Ellens and Hynynen, 2014; Wong et al., 2016; White et al., 2008), and we have observed heating in mouse models using the 1.16 MHz FUS system used in this study, at pressures within the range we evaluated(Poorman et al., 2016). The method could also be used to map the beams of focused imaging transducers, which are capable of generating similar pressure amplitudes to the FUS transducers evaluated here. Unlike previous optical beam mapping methods that used strobed light sources to "freeze" the ultrasound beam at different phases so that it can be reconstructed algebraically(Pulkkinen et al., 2017), we simplified the hardware setup by allowing the beam to run continuously during the acquisition which caused a blur rather than a coherent shift of the background pattern, and then used a deep neural network to solve the difficult inverse problem of reconstructing RMS projected pressure amplitudes from the blurred image at each location in the photographs. We described a complete 2D BOS hardware system and acquisition protocol, described a forward model for image formation, and established a reconstruction. It is

important to note that the reconstruction network operates only on one spatial location at a time, and does not make assumptions about spatial smoothness or structure of the beam in the imaged 2D plane, yet it produced beam maps that closely matched optical hydrophone measurements. This way, the technique maintains generality for important applications where beam structure would be difficult to predict, such as when mapping aberrated fields or when the beam rotates or moves, as were demonstrated here.

CW-BOS is an inexpensive (under $2000 USD) and rapid 2D FUS beam mapping tool based on a consumer-grade tablet and camera, with no moving parts or parts that can experience wear from the FUS beam. To make it portable, the tank could be sealed, the tablet and camera could be rigidly attached to it, and FUS could be coupled into it via a mylar membrane. The result would be a fully portable push-button beam mapping method, which could be set up and performed more easily and faster than QA tests such as MRI temperature measurements in a phantom, without requiring MRI scan time or an MRI-compatible FUS system.Bowl-shaped transducers could be coupled into the tank via a coupling bag. Our total CW-BOS scan times were 3-5 minutes, which was dominated by the time taken for data transfer from the camera to PC, and comprised less than 8 seconds of FUS-on time. We expect that with optimization, the total scan duration could be reduced to less than 10 seconds; reconstruction in MATLAB and Python then took another 20 seconds which could be further optimized, and does not require a high-end computer. Overall, the method achieved an approximate 2000x speedup compared to the time required to obtain the same information (RMS projected pressure over a 3 x 1 cm^2 FOV with 0.425 x 0.425 mm^2 spatial resolution) using a 3D hydrophone scan. While linear hydrophone scans along the axial and focal plane dimensions may suffice for quality assurance, those scans are still slower and involve more delicate and less portable hardware than CW-BOS imaging, and require careful alignment with the ultrasound focus. Overall, the most likely applications for CW-BOS projected pressure mapping will be those that are not well-served by hydrophones and in which speed, simplicity, and low cost are of highest importance, such as measuring changes in overall transducer output and detecting beam aberrations.

There are several possible ways to improve or extend the proposed technique. One potential source of error is the assumed parallel ray geometry between the background pattern and the camera; it may be possible to generate more accurate training histograms using ray tracing and accounting for refraction at the air-glass and glass-water interfaces(Glassner, 1989; Barsky et al., 2003). The dominant noise source in our measurements is likely electronic noise in the camera's detector, but this needs to be characterized and a propagation-of-error analysis should be done to understand noise in the final maps and how to best mitigate it. Another possible source of error would be a mismatch between the assumed and actual distance between the expected transducer focus and the background pattern. The reconstructions are trained using histograms calculated for a specific distance between the midpoint of the nonuniform index of refraction

field and the background pattern, which corresponded in our experimental setup to the distance between the expected focus and the background pattern. This is a parameter that could be optimized: Moving the beam closer to the background pattern would magnify the blurring patterns by a factor < 1, which would enable a larger field-of-view at the cost of reduced sensitivity. Moving the beam farther from the background pattern would magnify the blurring patterns by a factor > 1, which would increase sensitivity at the cost of reduced field-of-view. A larger convolutional neural network that operates on entire photos rather than individual segmented histograms may achieve improved accuracy by learning spatial relationships between blurring patterns and FUS beam features, and it could enable the use of a single, dense background pattern to reduce acquisition times. However, this would require a much larger training corpus to maintain generality, as well as more computation and memory, both for training and reconstruction. RMS projected pressure was used as the reconstructed quantity in this work since it is proportional to transducer output, but it may be possible to extend the method to also reconstruct peak positive and negative pressure, or even a full cycle of the projected pressure waveform at each spatial location, which would be needed to reconstruct 3D beam maps that contain the same information as 3D hydrophone scans. A 3D system would also require the optics and the transducer to be rotated with respect to each other. We have previously developed a qualitative backprojection-based 3D CW-BOS beam mapping system(Kremer et al., 2014, 2015), and will extend the proposed 2D quantitative method to 3D beam mapping in future work. Finally, in this work we trained the reconstruction network from acoustic simulations of transducers at the same frequencies as those used in the experiments, but with two different focal lengths and across a range of peak pressures. This approach resulted in RMS projected pressure reconstructions that closely matched hydrophone measurements, even when an aberrator was placed on the surface of the 1.16 MHz transducer. However, further research is needed to optimize the training data for different applications. For example, it may not be necessary to train for multiple focal lengths when the reconstruction network will be used with just one transducer, but care must be taken to maintain accuracy when the beam is disturbed by an aberration. For such an application it may be better to perform simulations of the same transducer, with different sub-elements on its surface virtually switched off to mimic aberrations. This process would ideally be informed by the types of aberrations (e.g., bones versus failed transducer elements, air bubbles in the beam path, or system calibration errors(McDannold and Hynynen, 2006)) that are most likely to be encountered for a given clinical or research application. If the reconstruction network will be used for just a small range of driving voltages, it may be possible to also reduce the range of simulated pressures. It may also not be necessary to train the network for each transducer frequency, or it may be possible to train a single network across a range of frequencies, without compromising reconstruction accuracy. At the same time, the storage required for each network was small (< 1 MB), so many networks could be trained and stored, and the most appropriate one could be selected for each mapping

task. While the proposed CW-BOS hardware is not currently compatible with very large-aperture transcranial FUS transducers whose foci do not extend beyond their shell, it may be possible to map these systems by projecting background patterns onto the transducer surface. These and related questions will be addressed in future work.

3.6 Acknowledgments

This work was supported by NIH grant R21 EB 024199. The authors would like to thank Charlotte Sappo for help with the shutter switch, and Marshall (Tony) Phipps with help using the optical hydrophone and FUS amplifier.

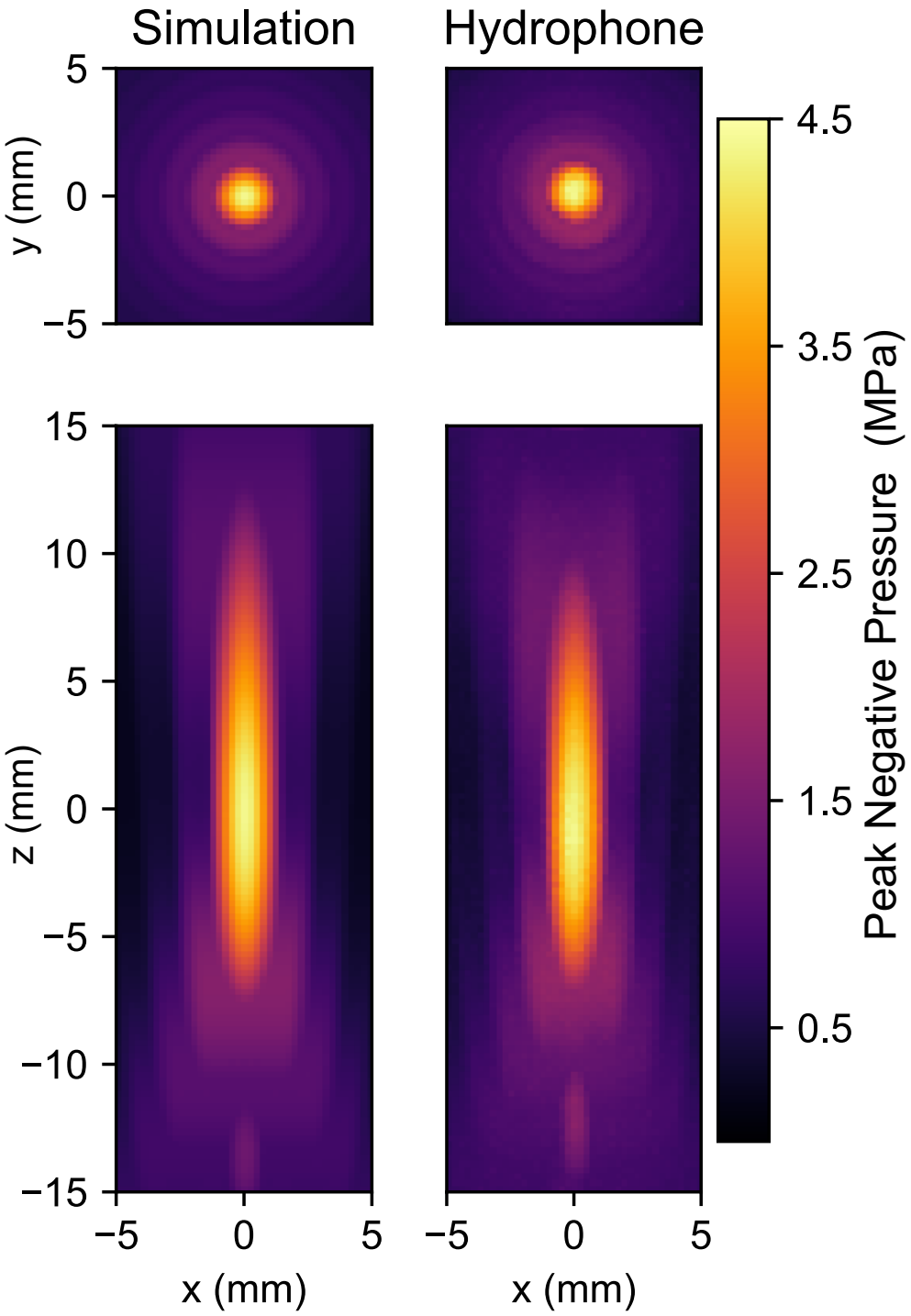

Figure 3.7: Simulated and optical hydrophone-measured 2D peak negative pressure maps at 1.16 MHz. Top: *x*-*y* maps cutting through the peak of the focus in *z*. Bottom: *x*-*z* maps cutting through the peak of the focus in *y*.

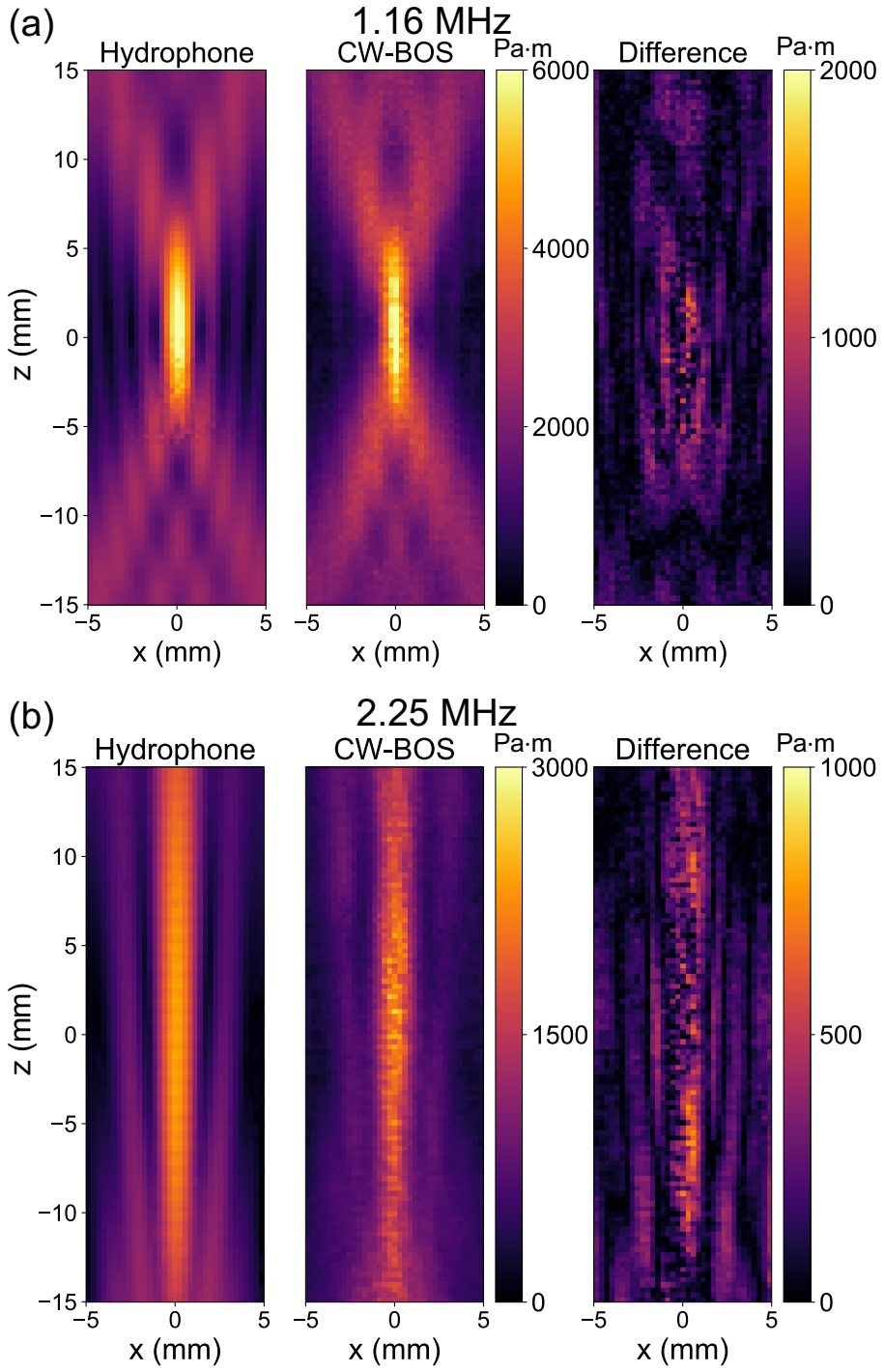

Figure 3.8: Comparison of RMS projected pressure maps measured using an optical hydrophone and CW-BOS for two transducers at different frequencies. The beam propagation direction is from bottom to top. a) Measured maps and their difference for the 1.16 MHz transducer. b) Measured maps and their difference for the 2.25 MHz transducer.

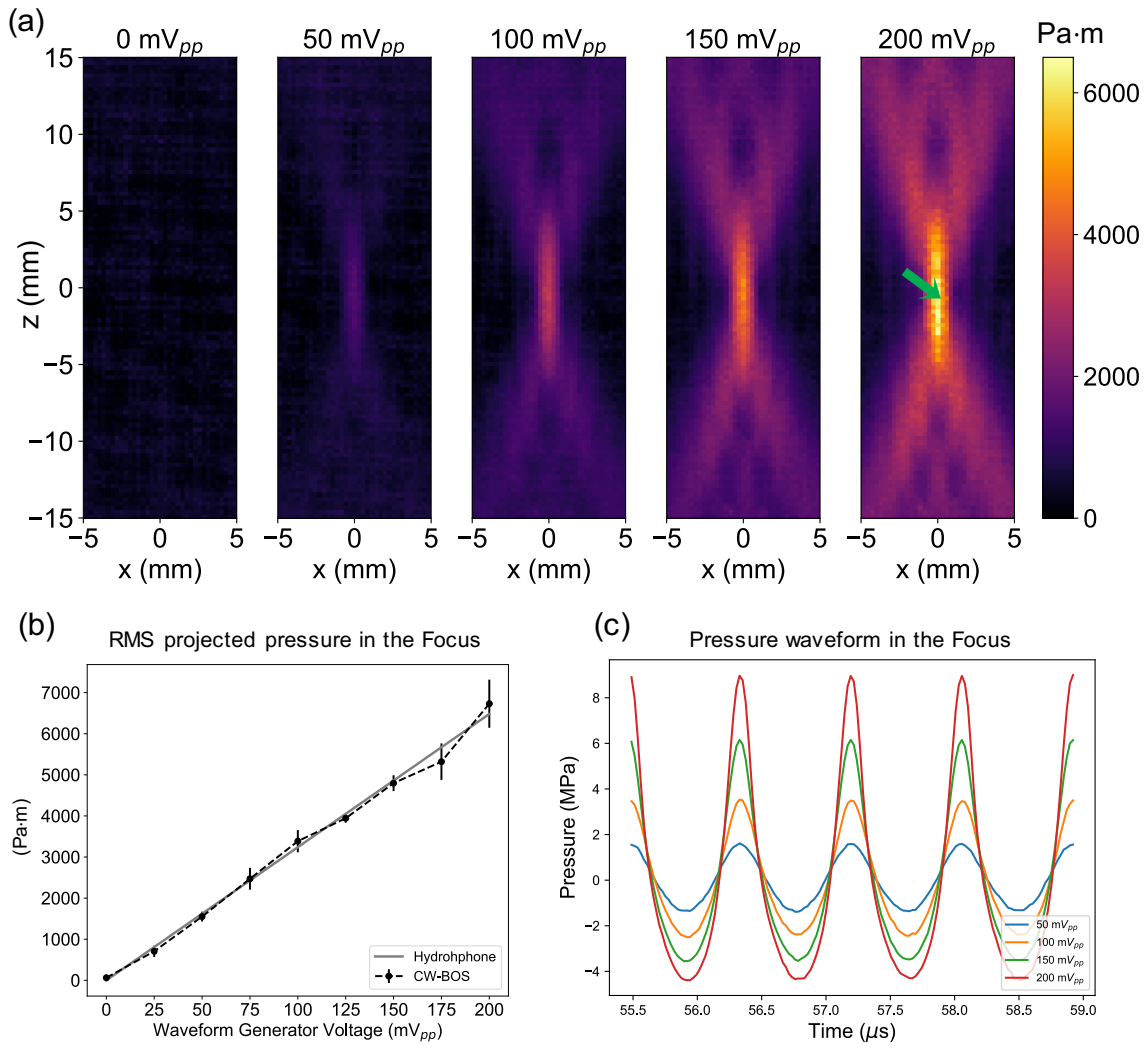

Figure 3.9: CW-BOS pressure maps versus waveform generator driving voltage amplitude. a) Reconstructed RMS projected pressure maps for the 1.16 MHz transducer. b) RMS projected pressure at the focus measured by the hydrophone and CW-BOS, where the CW-BOS values were averaged across five repeated measurements, and the error bars represent standard deviation across the measurements. c) Plots of hydrophone-measured waveforms at the focus, for four waveform generator voltage amplitudes.

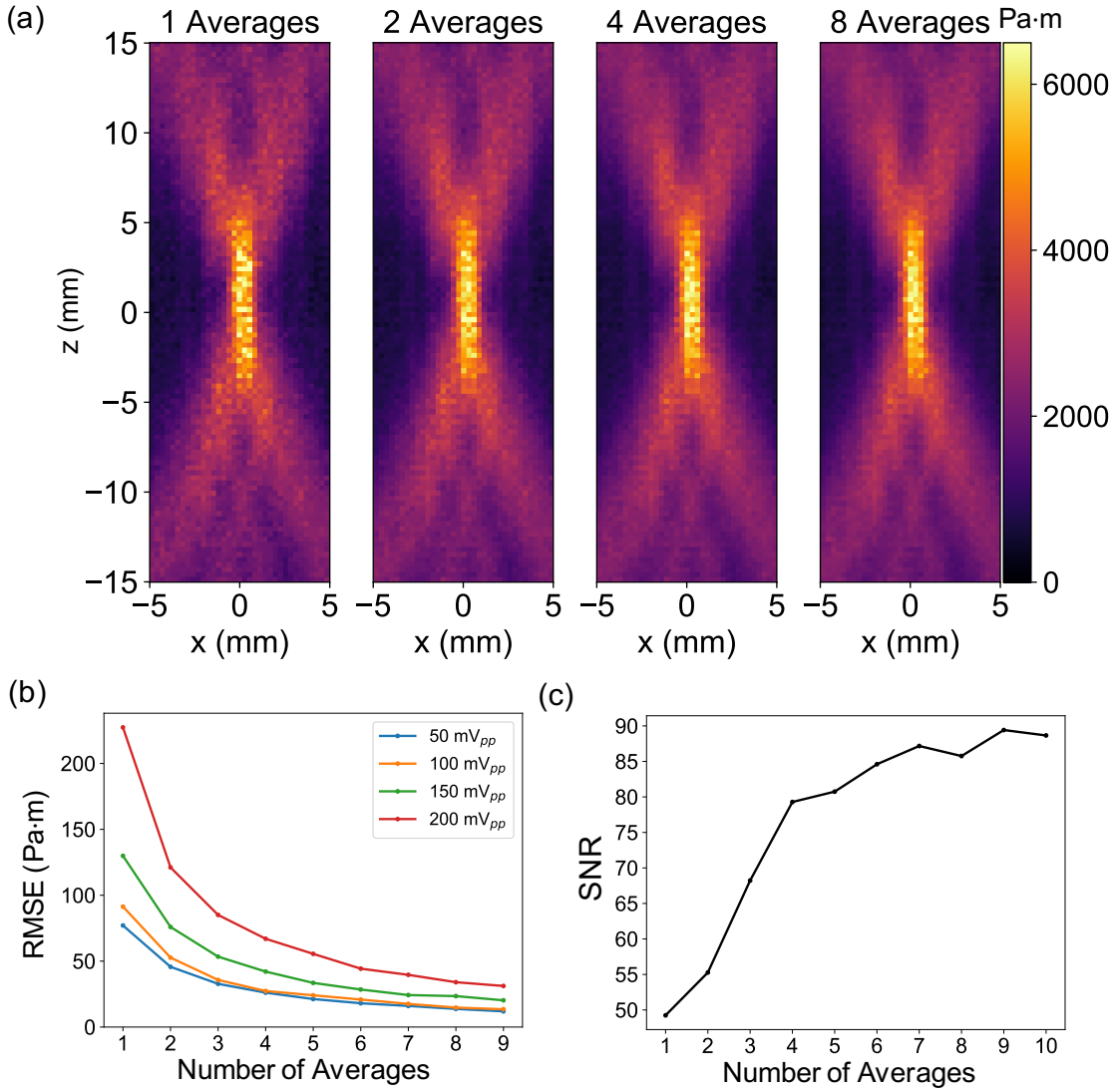

Figure 3.10: Signal-to-noise ratio (SNR) and reconstruction from different numbers of averages. a) Reconstructed RMS projected pressure maps across number of averages in powers of two with a waveform generator voltage of 200 mV_{pp} at 1.16 MHz. b) Mean-squared-error between maps resulting from $i+1$ versus i averages in a 5.6×20 mm^2 region around the focus, for four waveform generator voltage amplitudes. c) SNR around the focus with a waveform generator voltage of 200 mV_{pp} and one to ten averages.

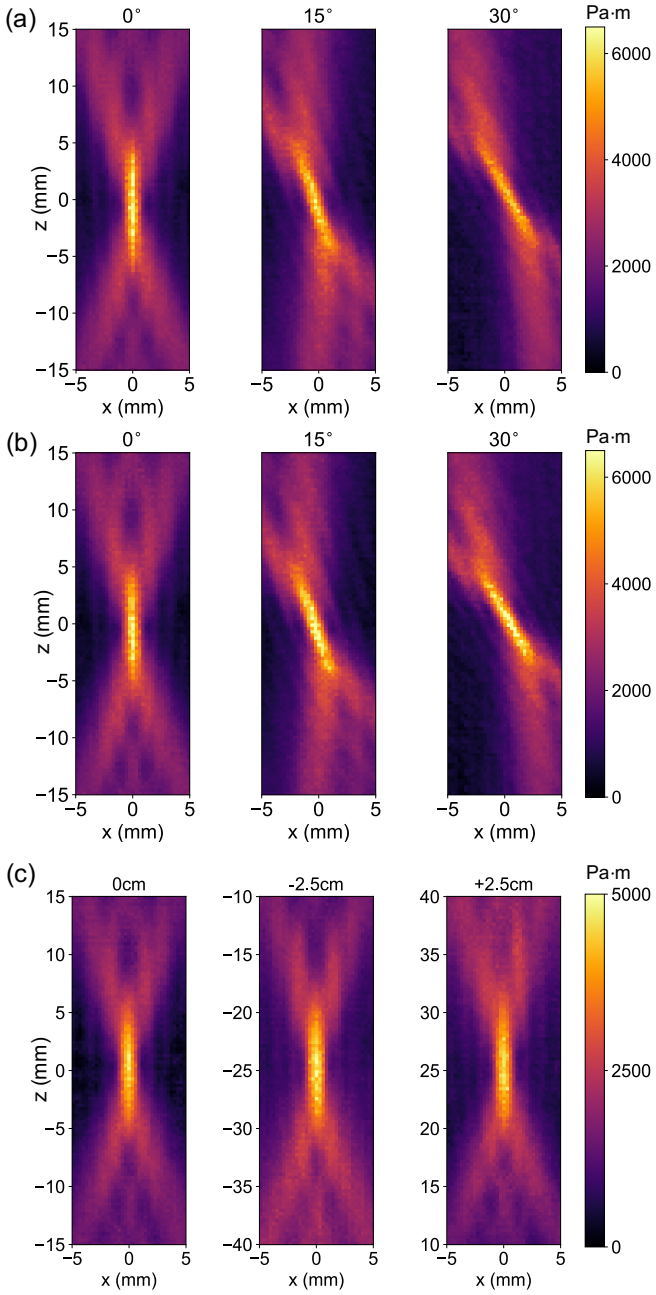

Figure 3.11: Rotational and translational invariance. a,b) RMS projected pressure maps obtained by rotating the 1.16 MHz transducer 0°, 15°, and 30°, and reconstructing maps using networks trained without (a) and with (b) rotated beams. c) Reconstructed RMS projected pressure map obtained with the camera focus centered on the focus, and shifted ±2.5 cm along the z-axis.

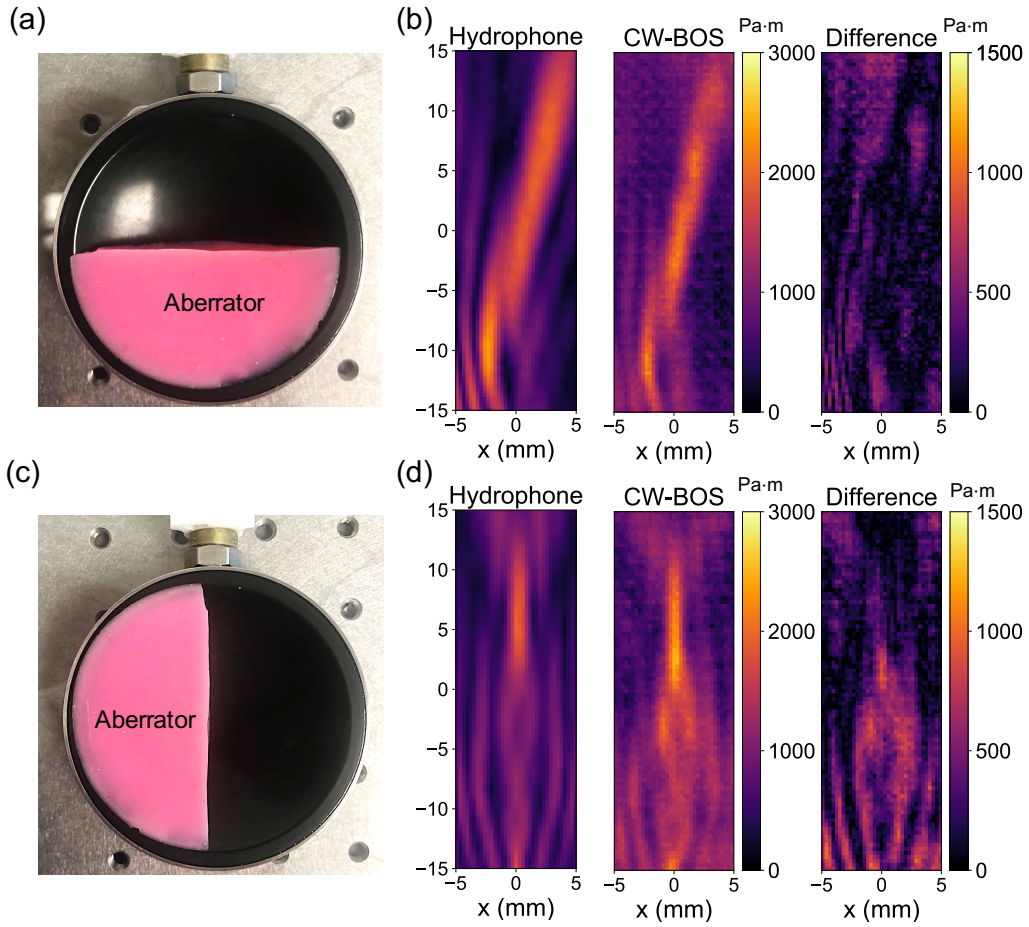

Figure 3.12: Aberrated beam mapping. a) An aberrator made from silicone was placed in front of the bottom half of the 1.16 MHz transducer. b) Optical hydrophone, CW-BOS RMS projected beam maps and the difference map between them measured with the bottom half of the transducer blocked. c) The aberrator positioned to block the left half of the transducer. d) Optical hydrophone, CW-BOS RMS projected beam maps and the difference maps between them measured with the left half of the transducer blocked.

CHAPTER 4

Reduced-FOV 3D MR acoustic radiation force imaging with a low-rank reconstruction for targeting transcranial focused ultrasound

4.1 Abstract

Purpose: To rapidly image and localize the focus in MR-guided FUS while maintaining a low ultrasound duty cycle to minimize tissue effects.

Methods: MR-ARFI is key to targeting FUS procedures such as neuromodulation, and works by encoding ultrasound-induced displacements into the phase of MR images. However, it can require long scan times to cover a volume of tissue, especially when minimizing the FUS dose during targeting is paramount. To simultaneously minimize scan time and the FUS duty cycle, a two-minute 3D reduced-FOV spin echo ARFI scan with two-dimensional undersampling was implemented at 3T with a FUS duty cycle of 0.85%. The 3D k-space sampling scheme incorporated uniform undersampling in one phase-encoded axis and partial Fourier sampling in the other. The scan interleaved FUS-on and FUS-off data collection to improve displacement map quality via a joint low-rank image reconstruction. Experiments in agarose phantoms and living macaque brains studied the effects of the sampling and reconstruction strategy on the acquisition, and evaluated its repeatability and accuracy.

Results: In phantom, the distances between displacement centroids of ten prospective reconstructions and the fully-sampled reference were below 1 mm. In in vivo brain, the distances between centroids ranged from 1.3 mm to 2.1 mm. Results in phantom and in vivo brain both showed that the proposed method can recover the FUS focus compared to slower fully sampled scans.

Conclusion: The proposed 3D MR-ARFI rFOV method enables rapid imaging of the FUS focus while maintaining a low FUS duty cycle.

4.2 Introduction

Magnetic resonance imaging-guided focused ultrasound (MRgFUS) is a noninvasive and spatially precise therapeutic technique that targets acoustic energy to the tissue deep inside the body, using MRI to target the focus and monitor treatment. MRgFUS has been widely applied to thermally ablate tissue for treatment of uterine fibroids, bone metastases, neurological disorders, prostate and breast cancer (Lozinski et al., 2021; Sridhar and Kohi, 2018; Catane et al., 2007; Elias et al., 2013b; Stavarache et al., 2021; Kobus and McDannold, 2015). Non-ablative brain applications of MRgFUS such as neuromodulation and blood-brain barrier opening (BBBO) are being increasingly studied (Li et al., 2020; Darrow, 2019; Abrahao et al., 2019).

However, when ultrasound waves propagate through tissue or skull bone with acoustic inhomogeneities, the ultrasonic waves are distorted, which leads to attenuation and spatial shifts of the FUS focus. Therefore, before applying high FUS energy for treatment, it is essential to verify if the FUS focus is positioned at the correct target.

MR acoustic radiation force imaging (MR-ARFI) images the FUS focal spot (Sarvazyan et al., 1998; McDannold and Maier, 2008; Pauly, 2015) by using motion-encoding gradients (MEGs) synchronized with FUS bursts to encode micron-level FUS-induced tissue displacements into phase shifts in MR images. Displacement maps are obtained by phase subtraction. MR-ARFI sequences usually use FUS bursts of 1 - 20 ms for each TR and a long TR to maintain a FUS duty cycle of 0.5% - 10%. While the basic safety of MR-ARFI at low duty cycle has been established in histology (Gaur et al., 2020) and simulation (Phipps et al., 2019; Ozenne et al., 2020) studies, the deposited heat and mechanical effects on neurons due to MR-ARFI's powerful and frequent FUS bursts could generate unwanted neuromodulatory effects (Wang et al., 2014) since the brain is very sensitive to even small temperature rises. Thus, the FUS-duty cycle of MR-ARFI should be kept as low as possible. As a result, long TRs corresponding to long delays between FUS bursts must be used which results in long scan times. In addition, it is necessary to cover the entire volume of the FUS focus to verify its center position and three-dimensional (3D) shape.

Full coverage of the focus lengthens the scan time, which limits MR-ARFI's use in iteratively identifying and re-steering the focus during treatment planning. To accelerate MR-ARFI, multishot EPI sequences (Phipps et al., 2019; Kaye et al., 2011) have been reported, as well as approaches to reduce k-space coverage such as outer volume suppression (reduced-FOV), partial Fourier (PF) imaging and keyhole imaging (Kaye et al., 2011; Holbrook et al., 2011; Odéen et al., 2019; Paquin et al., 2013). Existing MR-ARFI sequences are either 2D, 2D reduced-FOV, or 3D, where the 3D methods (de Bever et al., 2016) encode a whole brain volume in two dimensions. Parallel imaging (Deshmane et al., 2012) has also been used in MR-ARFI sequences (Odéen et al., 2019), but there are two major challenges associated with this: i) It is difficult to position multi-channel RF coils around bulky focused ultrasound transducers which must be in direct contact with the body; ii) The relatively small three-dimensional fields-of-view (not more than several centimeters in each dimension) over which the FUS beam needs to be mapped are not amenable to encoding with coil sensitivities which vary smoothly over space. Therefore, there is a need for an MR-ARFI technique that can cover a small 3D FOV with a short scan time and minimal FUS duty cycle, which does not rely on parallel imaging.

To cover the entire FUS focus and minimize the FUS duty-cycle and scan time in MR-ARFI, this work integrated reduced-FOV imaging with an undersampled 3D scan and a low-rank reconstruction algorithm to achieve a 3D reduced-FOV (rFOV) SE MR-ARFI pulse sequence with a scan time of 2 minutes and 20

seconds, which images a FOV of 160×40×40 mm^3 with 2 mm isotropic resolution. The frequency encoding direction was aligned with the ultrasound propagation direction, and the FOV was reduced in the two orthogonal dimensions by applying selective 90° and 180° pulses in those dimensions, which minimized the required phase-encoding steps. The FUS duty cycle was minimized by combining a long repetition time (TR) with alternate collection of FUS-ON and FUS-OFF data each TR, where the FUS-OFF image data were collected with a complimentary k-space sampling pattern and the FUS-OFF image was jointly reconstructed with the two FUS-ON images (with opposite displacement phase shifts) to improve their quality. To reduce the scan time, the scan used a small EPI factor with uniform undersampling in the EPI phase-encoded dimension and PF sampling in the other phase-encoded dimension. A low-rank reconstruction algorithm based on self-consistency with acquired k-space data and matching image magnitudes was implemented to reconstruct three images (two FUS-ON with opposite displacement phase shifts, and one FUS-OFF), and displacement maps were calculated from the two FUS-ON images. To evaluate the proposed technique, experiments were performed in a brain tissue-mimicking phantom and in two macaque brain studies. In the macaque brain, the focus was targeted in two different locations: one in cortical grey matter for BBBO, and one in the periaqueductal gray (PAG) in the midbrain for neuromodulation. Results in the phantom and in vivo brains show the proposed MR-ARFI scan recovered the FUS focus with high fidelity compared to full sampling. Retrospectively undersampled phantoms were also use to study the effect of undersampling in each dimension and characterize its repeatability. The reported technique could improve the efficiency of MRgFUS brain applications, especially when MR-ARFI needs to be repeated several times for finding, steering or phase-correcting the focus.

4.3 Methods

4.3.1 Pulse Sequence

The 3D rFOV SE MR-ARFI sequence was implemented on a 3.0-Tesla (T) human MRI scanner (Philips Elition, Philips Healthcare, Best, Netherlands). As the pulse sequence diagram in Figure 4.1b depicts, the two phase-encoded FOV's were reduced by applying the selective excitation pulse along the slow phase-encoded dimension (k_z), and the selective refocusing pulse along the EPI phase-encoded axis (k_y), enabling the excitation of a rectangular slab which covers the entire focus (Figure 4.1a). Selective minimum-phase excitation and linear phase refocusing pulses were designed by the Shinnar-Le Roux algorithm (Pauly et al., 1991). Root-flipping (Sharma et al., 2016) was applied to the refocusing pulse to limit its peak amplitude to 12.87 μT while shortening its duration to 4.12 ms. Without root-flipping, its duration would be 14.0 ms for the same peak amplitude. The time-bandwidth products of 90° and 180° pulses were 7.0 and 5.0, respectively. For ARFI displacement encoding, a pair of unipolar trapezoidal MEGs were placed before and

after the refocusing pulse. k-Space data collection with and without FUS bursts were alternated between TRs to maintain a low FUS duty-cycle with a period of 2 TRs. The FUS emission was synchronized with the first MEG (odd k_y lines) or second MEG (even k_y lines) (Mougenot et al., 2015).

The sequence's k-space sampling scheme is illustrated in Figure 4.1c. As illustrated in Figure 4.1d, the root-flipped refocusing pulse applies approximately quadratic phase across the refocused slab which broadens the k-space signal along the k_y direction. This suggests an acquisition in which uniform undersampling is applied along the k_y direction, and partial Fourier undersampling is applied along the k_z direction. The sequence acquires subsampled data of three 3D rFOV images: two with opposite polarities of the motion-encoded phase shifts by changing the timing of FUS emission (x^{ON+} and x^{ON-}), and with FUS off (x^{OFF}). The timing of ultrasound emission was alternated between odd and even k_y lines to obtain complementary k-space data between the two FUS-ON images. The acquired k-space data of images x^{ON+} and x^{ON-} were undersampled uniformly in the k_y-direction by an acceleration factor (R) of 2 with complementary sampling patterns. Partial Fourier (PF) encoding was applied in the k_z-direction to reduce the scan time further, with a factor of 0.67. Additionally, the FUS-ON and FUS-OFF k-space datasets were acquired with opposite PF directions to obtain complementary k-space data (FUS-ON: 'left half', FUS-OFF: 'right half' in Figure 4.1c).

4.3.2 Image Reconstruction

The flowchart in Figure 4.2 shows the image reconstruction algorithm. The unsampled k-space data points were recovered with a low-rank reconstruction using annihilating filters (Haldar, 2013; Jin et al., 2016) with a data consistency constraint and a constraint that all three images have the same magnitude, since the acoustic radiation force applied by the FUS beam is expected to only change image phase. The virtual conjugate coil concept (Blaimer et al., 2009) was also applied by treating the three images as different 'coils' whose conjugate symmetric k-space signals were used as to generate virtual coil signals. The reconstruction algorithm solves the following nuclear norm-regularized least-squares optimization problem:

$$\min_{x_+,x_-,x_0} \|y_+ - P_+Fx_+\|_2^2 + \|y_- - P_-Fx_-\|_2^2 + \|y_0 - P_0Fx_0\|_2^2 + \lambda\|H(x_+,x_-,x_0)\|_*, \tag{4.1}$$

where the '$+$', '$-$', and '0' subscripts respectively represent positive and negative FUS-ON and FUS-OFF, the x are the reconstructed images, the y are the collected k-space data, and the P are the k-space sampling patterns. F is a Fourier transform operator, and λ is a regularization parameter that balances data consistency with the nuclear norm of the block-Hankel matrix $H(x_+,x_-,x_0)$. As illustrated in Figure 4.2, in each iteration of the reconstruction the 3D datasets are extracted as blocks which are stretched to form rows of the Hankel matrix for each dataset, which are then concatenated into $H(x_+,x_-,x_0)$. That matrix is singular

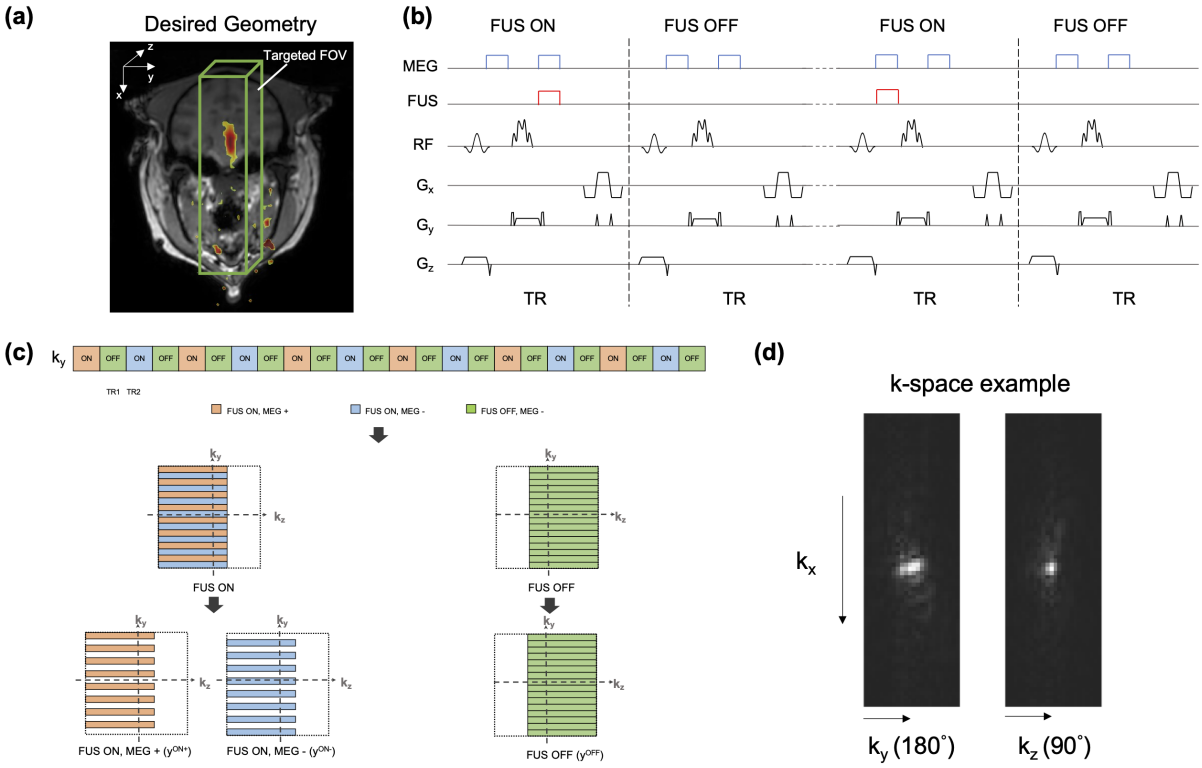

Figure 4.1: **a**: The proposed 3D rFOV MR-ARFI sequence images a rectangular cube sized to cover the entire focus along the FUS axial dimension. **b**: Timing diagram of the 3D reduced-FOV (rFOV) spin-echo ARFI pulse sequence: unipolar motion-encoding gradients (MEGs) are placed before and after 180° pulse, the 180° pulse was applied to the in-plane EPI phase-encoded dimension (y) to reduce the FOV, and the ultrasound emission was alternated on or off between TRs. **c**: The proposed k-space undersampling scheme: the FUS pulses were synchronized with the first MEG (odd k_y lines) or the second MEG (even k_y lines) to obtain positive and negative motion-encoded phases. The partial Fourier direction was alternated between TRs. Three 3D k-space datasets (y^{ON+}, y^{ON-} and y^{OFF}) with complementary undersampling patterns were acquired for each ARFI scan. **d**: Perpendicular k-space dataset slices illustrate how the root-flipped refocusing pulse applied an approximately quadratic phase that spread out k-space energy in the k_y direction, making that dimension amenable to uniform R = 2 undersampling, while the k_z dimension was better suited to partial Fourier sampling.

value-thresholded, and the thresholded matrix is converted back to k-space data and then images. To constrain the images to have the same magnitude, a single magnitude image I_m is calculated from the first component of the SVD of the $N_x \times 3$ matrix formed from the current image estimates $\hat{x}^{ON+}$, $\hat{x}^{ON-}$ and $\hat{x}^{OFF}$. Then, the magnitudes of $\hat{x}^{ON+}$, $\hat{x}^{ON-}$ and $\hat{x}^{OFF}$ are replaced with I_m but their phases are left unmodified. Finally, data consistency is enforced by replacing the sampled data in the reconstructed data arrays.

Image reconstructions were performed in MATLAB 2020b (Mathworks, Natick, MA, USA). Coil compression (Zhang et al., 2013) was first applied to the raw data acquired from the scanner before reconstruction, to compress data to a single channel. The displacements Δd were calculated by complex phase subtraction of FUS-ON images with positive and negative displacement encoding phases to cancel out the background phases:

$$\Delta d = \frac{\angle(x^{ON+} \cdot (x^{ON-})^*)}{2\gamma G \tau} \tag{4.2}$$

where γ is the gyro-magnetic ratio, G is the gradient strength and τ is the gradient duration.

4.3.3 Experiments

rFOV MR-ARFI images were acquired in 2 minutes 20 seconds with imaging parameters of FOV (x/y/z) 160×40×40 mm^3, 2×2×2 mm^3 isotropic resolution, flip angle 90°, TE/TR 38 ms/500 ms, and EPI factor of 3 echoes per TR. The effective echo spacing was 0.0625 ms and the oversampling factors along the two phase-encoded dimensions were both 1.2 to account for transition bands of the selective excitations, i.e., the encoded FOVs in the two phase-encoded dimensions were 48 mm, to account for transitions of the 40 mm-wide excitation and refocusing profiles. Unipolar MEGs with strength 40 mT/m and duration 8 ms were used for ARFI displacement encoding with a trigger delay of -1.5 ms. The same scan was also collected with full sampling for reference, with the same parameters and a scan time of 6 minutes 28 seconds. High-resolution large-FOV T_1-weighted images were acquired in the same sessions with a T_1-weighted GRE sequence. The parameters of that sequence were: in-plane FOV 18.1 × 18.1 cm^2, in-plane reconstructed resolution 0.42 × 0.42 mm^2, and TE/TR 3.7 ms/8 ms.

The phantom experimental setup is shown in Figure 4.3 (left). An MR-compatible single-element transducer (H115MR, Sonic Concepts, Bothell, WA, USA) was used to generate ultrasound emissions at 850 kHz with a low duty-cycle (8.5 ms per 1000 ms / 2 TRs, free field pressure 2.7 MPa) for all phantom experiments. A custom 3D-printed coupling cone with a 3 cm-aperture held the transducer and was filled with agar (1% weight by volume). The cone was connected to a 3D-printed cylindrical phantom container with a diameter of 8 cm. The remaining space in the cone and the phantom holder was filled with an agar-graphite phantom (1% agar/4% graphite weight by volume) to mimic brain tissue acoustic properties (Phipps et al., 2019; Madsen

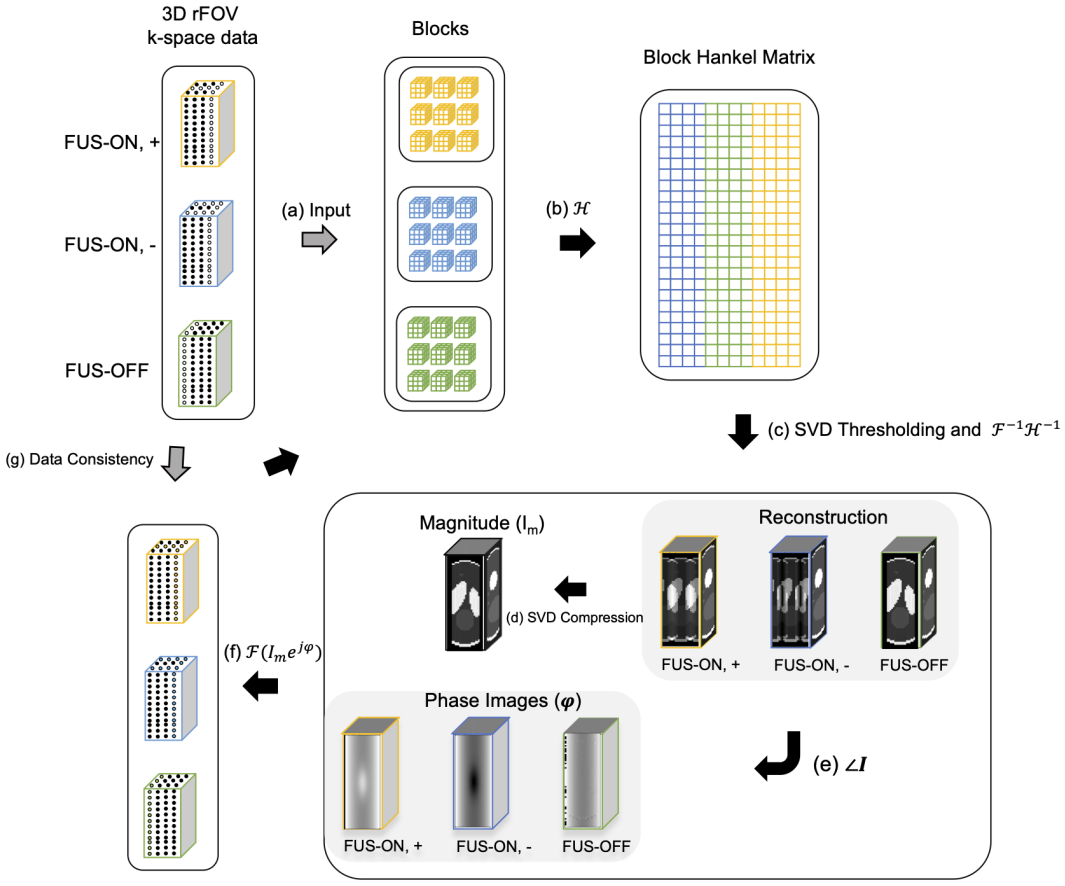

Figure 4.2: Flowchart of Low-rank image reconstruction. Step a - b: At each iteration the k-space datasets for the three images are segmented into blocks that are stretched to form a Block Hankel matrix; Step c: That matrix is singular value-thresholded and converted back to estimated images; Step d - f: One magnitude image I_m was calculated by taking the first singular component of SVD of three images (FUS ON, +; FUS ON, -; FUS-OFF) and then was applied to replace the magnitudes of the current image estimates with unchanging phases; Step g: The originally acquired k-space data were reinserted into the recovered data to enforce data self-consistency.

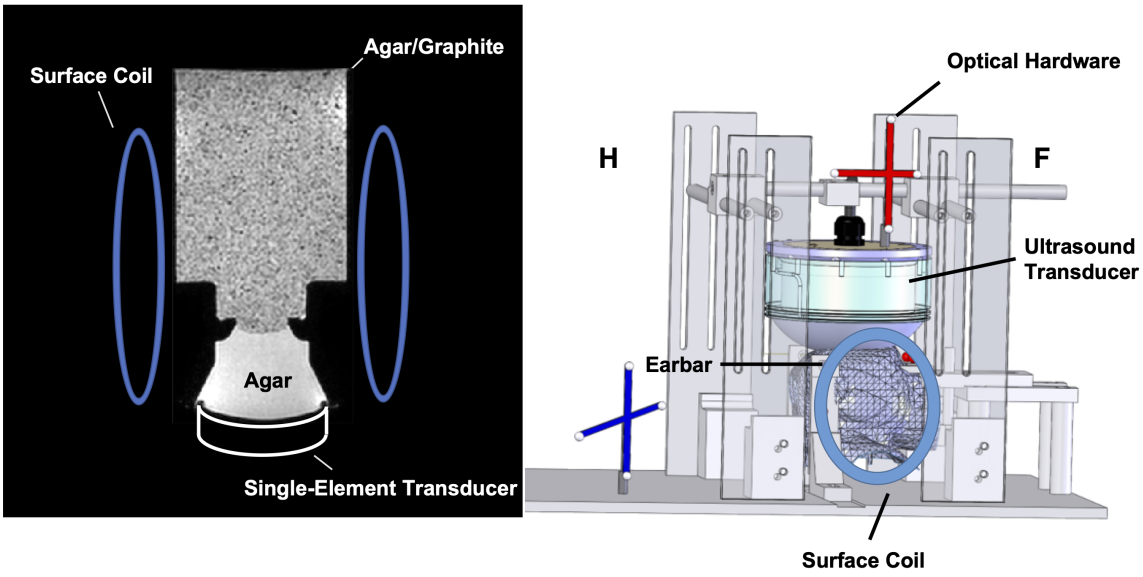

Figure 4.3: Experimental setup for phantom (left) and macaque imaging (right).

et al., 1978). A pair of 2-channel phased-array coils (Flex-L; Philips Healthcare) were placed on either side of the phantom. The volumetric FOV was aligned with the ultrasound beam by finding the geometric focus according to the transducer's 64 mm focal length. The MEGs were aligned with the ultrasound propagation direction (anterior-posterior). The fully-sampled and accelerated rFOV MR-ARFI scans were repeated ten times to obtain a high-SNR averaged reference and study repeatability of the acquisitions. The mean and standard deviations around the focus were calculated for the displacements in a $3\times3\times3$-voxel ($6\times6\times6$-mm^3) region centered at the voxel with maximum displacement. The displacement SNR was calculated as the ratio of peak displacement at the focus and the standard deviation of background displacements. In addition, we calculated the distances between the displacement centroid for each individual reconstruction and the centroid of the averaged fully-sampled reference, where centroids were calculated according to:

$$\bar{r} = \frac{\sum_i \bar{r}_i d_i}{\sum_i d_i} \tag{4.3}$$

where $\bar{r}$ is the position of the displacement centroid, $\bar{r}_i$ is the position of each voxel and d_i is the displacement at voxel $\bar{r}_i$.

Two sets of in vivo MR-ARFI scans were performed in a healthy adult female macaque monkey weighing 4.2 kilograms. Imaging procedures were approved by the Institutional Animal Care and Use Committee (IACUC) at Vanderbilt University and are in agreement with all guidelines and regulations. The animal was anesthetized with 1-1.5% isoflurane and mechanically ventilated. The Monkey head was positioned in

an MRI-compatible stereotaxic frame. Physiological vital signs (heart rate, end-tidal Co2, and SpO2) were consistently monitored and maintained at stable ranges. Figure 4.3 (right) illustrates the experimental setup for these experiments, in which the focus was positioned in the periaqueductal grey for neuromodulation, and in cortical grey matter for blood-brain barrier opening (BBBO). The optical tracking method described in Ref. (Phipps et al., 2019) was used to align the FOV with the ultrasound beam. The direction of MEGs was aligned with the vertical dimension. For neuromodulation, a custom-designed phased-array transducer at 650 kHz described in Ref. (Chaplin et al., 2018) was used to generate ultrasound emissions with a duration of 8.5 ms per 1000 ms/2 TRs, with an estimated free-field pressure of 6.4 MPa. Measurements though an ex vivo nonhuman primate skull with that transducer estimated the focal pressure to be 28 percent of the free field pressure (Chaplin et al., 2018) resulting in an estimated in situ pressure of 1.8 MPa. For ARFI acquired during BBBO procedures, the ultrasound emissions were generated by a 1 MHz phased-array transducer (Imasonic, France) with 128 elements with the same duty cycle and an estimated in situ pressure of 1.5 MPa with an estimated 20 percent of free field pressure transmission through the skull. The transmission estimate is based on hydrophone measurements through an ex vivo NHP skull and acoustic simulations using k-Wave (Treeby and Cox, 2010). The BBBO was performed at the target, and then gadolinium contrast agent (Gadavist) was injected. Two T_1 weighted images were collected before injection and after the Gadavist perfused into the target spot. A pair of two-channel phased-array coils (Flex-S; Philips Healthcare) were placed on either side of the macaque's head. Due to inter-scan differences between the reference in vivo fully-sampled scans and the undersampled scans, displacement map reconstructions were performed from both retrospectively undersampled and prospectively undersampled data. The mean ($\pm$ standard deviation) displacements at the maximum displacement, the maximum displacement, and the full-widths-at-half-maximums (FWHMs) of the displacement profiles along US-x/y/z direction were calculated. The FWHM's of the FUS focus along the long axis (US-x) and two short axes (US-y and US-z) were measured by Gaussian fitting of the displacement profiles across the point with the maximum displacement with the least-squares curve fitting using MATLAB function "lsqcurvefit".

4.4 Results

Figure 4.4 shows the middle axial and sagittal slices of full-FOV T_1-weighted images (reference) and rFOV ARFI magnitude images in the macaque brain (top) and phantom (bottom) experiments, respectively. The blue boxes indicate the positions of the rFOV images in the full-FOV reference images.

Figure 4.5 shows axial, sagittal, and coronal slices through the point with maximum displacement with R = 2 undersampling alone, R = 2 undersampling and partial Fourier together, and R = 2 undersampling and partial Fourier together but without joint reconstruction of the FUS-OFF image. These phantom results

were obtained by retrospectively undersampling one of fully-sampled phantom datasets. The displayed displacement maps were cropped in the frequency encoded dimension to a FOV of $64\times48\times48$ mm^3. The right subfigure illustrates the position of zoomed-in displacement maps in the full-FOV reference. The reconstructions from the undersampled data of R = 2 only (2nd row), R = 2 and PF sampling (3rd row) recovered the displacement maps successfully, with root-mean-squared errors (RMSEs) of 0.257 μm and 0.268 μm compared with the reference. The fourth row shows the reconstructed maps of undersampled data without jointly reconstructing the FUS-OFF images, with led to a high RMSE of 3.893 μm. The reconstruction algorithm failed in this case due to the lack of the FUS-OFF image's k-space data in the joint reconstruction.

Figure 4.6 shows the repeatability results, reported as boxplots of mean and peak displacement, Euclidean distances to the centroid of the averaged fully-sampled reference, and FWHMs in three directions across ten repeated prospectively undersampled acquisitions. The reference metrics from the ten averaged fully-sampled datasets were 1.55 μm (displacement mean), 2.36 μm (peak displacement), and 6.09/20.31/6.01 mm (FWHMs in the US-x/US-y/Us-z directions). The image SNR was 48.2, the background standard deviation of displacement maps was 0.11 μm, and the displacement SNR was 20.9.

Figure 4.7 shows reconstructed displacement maps in the slices with maximum displacement in the macaque brain in the neuromodulation experiment. The displayed images with FOV $54\times48\times48$ mm^3 are cropped in the fully sampled frequency encoding dimension (the axial FUS dimension). The axial slice shown on the right illustrates the location of the focus and sub-images on a full-FOV reference image. The second row shows a reconstruction from retrospective undersampling of the fully sampled dataset and the third row shows a reconstruction from a prospectively undersampled scan. These displacement maps illustrate the differences between the fully-sampled and undersampled scan that arise from the undersampling and reconstruction alone, versus the differences that arise from inter-scan variation. The displacements (mean$\pm$std) in an ROI of size $6\times6\times6$ mm^3 with the maximum displacement were 2.25 ± 0.75 μm (fully-sampled), 2.02 ± 0.86 μm (retrospectively undersampled), and $2.51 \pm 0.78\mu$m (prospectively undersampled). The peak displacements were 4.04 μm (fully-sampled), 4.26 μm (retrospectively undersampled), and 4.24 μm (prospectively undersampled). FWHM's in the US-x/US-y/Us-z direction were 11.54/5.80/6.18 mm, 12.63/5.59/5.96 mm, and 11.36/6.13/6.34 mm. The distance between displacement centroids of undersampled reconstructions and the fully sampled reference were 2.02 mm (retrospectively undersampled) and 2.17 mm (prospectively undersampled). The background standard deviation of displacement maps was measured as 0.11 μm. The measured image SNR was 89.63 and the displacement SNR was 38.49.

Figure 4.8 shows the same reconstructed displacement maps with a FOV of $50\times48\times48$ mm^3 in the slices with maximum displacement in the macaque brain in the BBBO experiment. The axial slice shown on the right illustrates the location of the focus and sub-images on a full-FOV reference image. In the displace-

ment maps from fully-sampled, retrospectively-sampled and prospectively-sampled data, the displacements (mean±std) in the ROI of size 6×6×6 mm^3 with the maximum displacement were, respectively, 1.28 ± 0.40 μm, 1.37 ± 0.44 μm and 1.25 ± 0.45μm. The peak displacements were 2.19 μm, 2.41 μm and 2.40 μm, and FWHM's in the US-x/US-y/Us-z directions were 11.50/5.37/6.39 mm, 14.31/5.90/6.28 mm, and 11.71/5.85/5.93 mm. The distances between displacement centroids of undersampled reconstructions and the fully sampled reference were 1.36 mm (retrospectively undersampled) and 1.74 mm (prospectively undersampled). The background standard deviation of displacement maps was measured as 0.08 μm. The measured image SNR was 65.99 and the displacement SNR was 29.27. Figure 4.9 shows the gadolinium-based percentage signal change (%) at region of blood-brain barrier disruption ranging from 5% to 35%, overlaid on an axial T_1-weighted image. The contour of the focus in Figure 4.8 is marked by the blue contour. An additional BBBO case without a corresponding contrast-enhanced imaging is shown in Figure 4.10.

4.5 Discussion

The main goal of this work was to develop an MR-ARFI pulse sequence and image reconstruction that simultaneously minimized scan time and FUS duty cycle, so that the FUS focus can be localized repeatedly in-between targeting adjustments while reducing the effect of FUS on tissue,to compensate focus position errors and distortions caused by the skull and other acoustic inhomogeneities. To this end, a reduced-FOV 3D spin echo MR-ARFI sequence with 2 mm isotropic spatial resolution and 160×40×40 mm^3 FOV was described and validated in phantom and macaque brain experiments. The scan is ultimately intended for human use, where the long (frequency encoded) axis of the 3D volume should be aligned with the FUS propagation direction, with the nominal focus centered. The sequence used root-flipping to minimize the duration of the refocusing pulse and reduce TE compared to a conventional linear phase refocusing pulse. Images were reconstructed using a k-space low-rank reconstruction algorithm that jointly reconstructs undersampled k-spaces for two FUS-ON images with opposite ARFI phase shift polarities, and a third FUS-OFF image. The third FUS-OFF image data were collected 'for-free' in-between the FUS-ON segments of the sequence, to maintain a minimal FUS duty cycle. Collecting the FUS-OFF image data improved conditioning of the FUS-ON image reconstruction problem, enabling a shortened scan time with undersampling of the FUS-ON image data. With an overall acceleration factor of 2 × 1 / 0.67 = 3, a scan time of 2 minutes 20 second was achieved. Matching duty cycle, spatial resolution, and EPI factor with the described sequence, and accounting for the fact that existing 3D or 2D multislice-compatible scans would need to encode the entire brain volume in one phase-encoded dimension, the shortest scan time achievable with existing scans is approximately 7 minutes 30 seconds (Mougenot et al., 2015).

The phantom results from retrospectively undersampled data described the effects of sampling schemes

on the performance of the reconstruction. Those results showed that it is necessary to utilize the spare time to acquire FUS-OFF images as a reference to improve the reconstruction of the FUS-ON images (Figure 4.5). We found that too large a PF factor can lead to blurring of the focus in the z dimension; at the same time, using an opposite PF sampling pattern in the FUS-OFF acquisition mitigated this blurring. These considerations led to the selection of the PF factor of 0.67 to safely visualize the focus. In vivo macaque imaging results were also shown: one for a focus position determined for a neuromodulation experiment in which the MEGs and imaging volume were well-aligned with the FUS axial dimension, and one in which the MEGs and imaging volume were intentionally misaligned with the FUS axial dimension. In each case the FUS beam was well-localized, and undersampling the k-space data prospectively had minimal effect on the focus characteristics.

There are variations on the proposed sequence that may achieve shorter scan times or improved displacement SNR. For example, we used a low EPI factor of 3 to minimize distortions due to bulk off-resonance. If off-resonance were not a concern, the EPI factor could be increased and the scan time would shorten in proportion to that increase. 8 ms MEGs and FUS pulses with a 0.85% duty cycle were used in this work, which produced peak displacement phase shifts of approximately 0.20 radians in the phantom scans and 0.18 to 0.24 radians in the macaque scans. However, there remained considerable 'dead time' in the scan (specifically, almost 450 ms of every 500 ms TR) which could be used for additional data collection, at the cost of reduced signal due to reduced longitudinal relaxation between excitations. For example, if the duty cycle could be increased or if the pulses could be driven with higher power and shortened, then additional FUS-ON measurements could be made in the same scan time which could enable reduction in the PF factor or the undersampling (R) factor, without compromising the displacement phase shift. Shorter FUS pulses would also enable a shorter TE in the sequence which would increase SNR further. The reconstruction approach described here would not need to be modified to accommodate these variations.

4.6 Conclusion

In conclusion, the presented 3D rFOV MR-ARFI pulse sequence and the low-rank reconstruction method enables rapid acquisition of a volumetric view of an ultrasound beam with a low FUS duty cycle and while preserving the visibility of the FUS beam focus, with a scan time of two minutes twenty seconds and 2 mm isotropic resolution. The presented work with a short scan time will enhance the procedure of targeting the focus, especially when it needs to be repeated many times when finding, steering, or phase-correcting the focus.

4.7 Acknowledgements

The authors would like to thank Abitha Srinivas in Grissom Lab for help with the phantom holder.

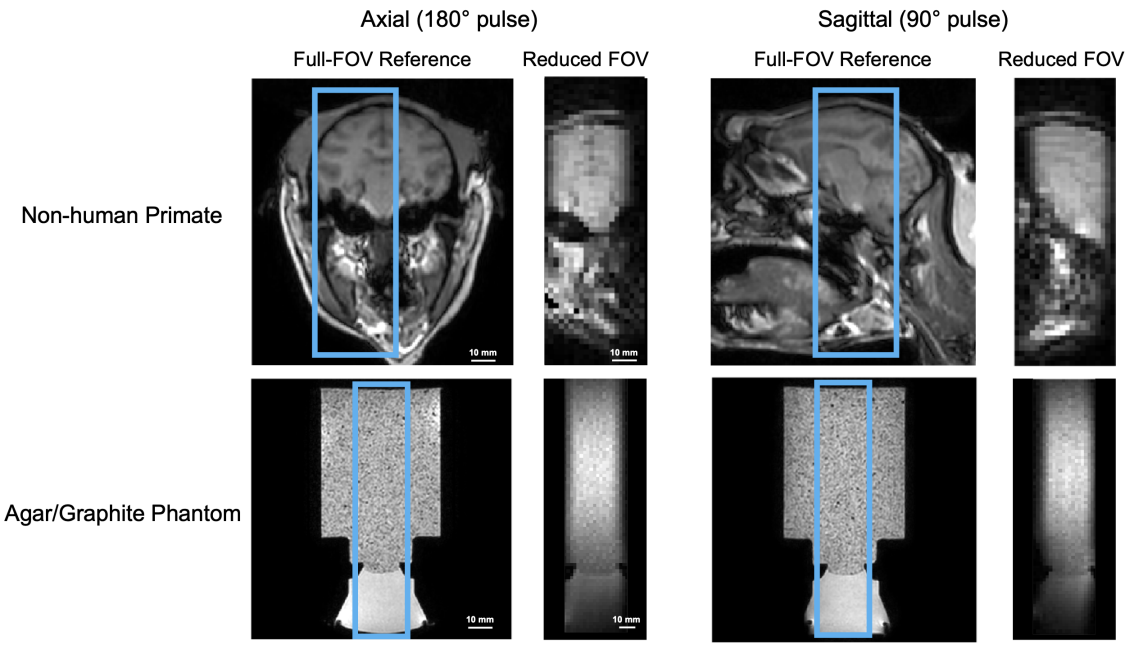

Figure 4.4: Middle axial and sagittal slices of reduced-FOV images compared with full-FOV high-resolution structural scans of in vivo macaque brain (top) and a brain-tissue mimicking phantom (bottom). The axial plane was selected by 180° RF pulse and the sagittal plane was selected by 90° RF pulse.

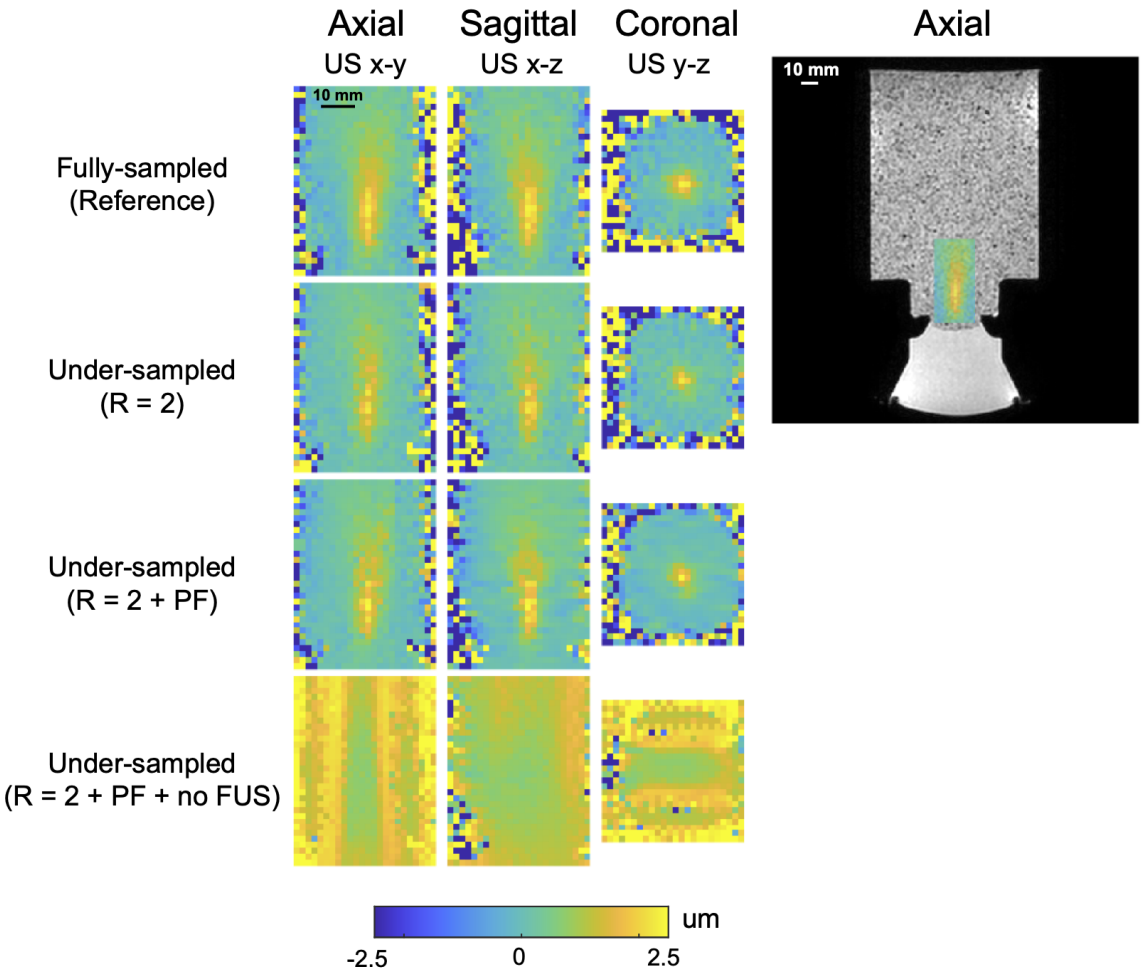

Figure 4.5: Phantom displacement maps reconstructed from retrospectively undersampled data with different sampling settings (from top to bottom): Fully-sampled, R = 2 only, R = 2 and PF = 0.67, R = 2 and PF = 0.67 but without FUS-OFF images. The subfigure on the right shows the position of the displacement maps shown on the left in the larger phantom, overlaid on a full-FOV axial image.

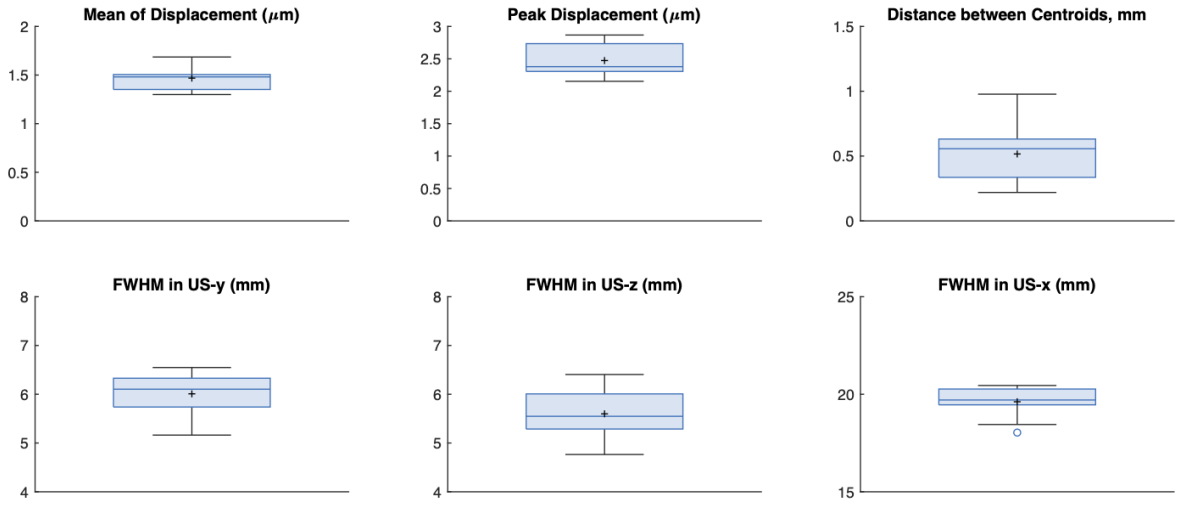

Figure 4.6: Boxplots of mean and peak displacements in a 6×6×6 mm^3 ROI centered at the voxel with the maximum displacement, Euclidean distances to the centroid of the averaged fully-sampled reference and FWHMs in three directions for reconstructions of ten repeated phantom scans. The line inside the boxes are the median values. The '+"s represent the mean value. The lower and upper box boundaries are the 25th and 75th percentiles, and the whiskers represent the minimum and the maximum values.

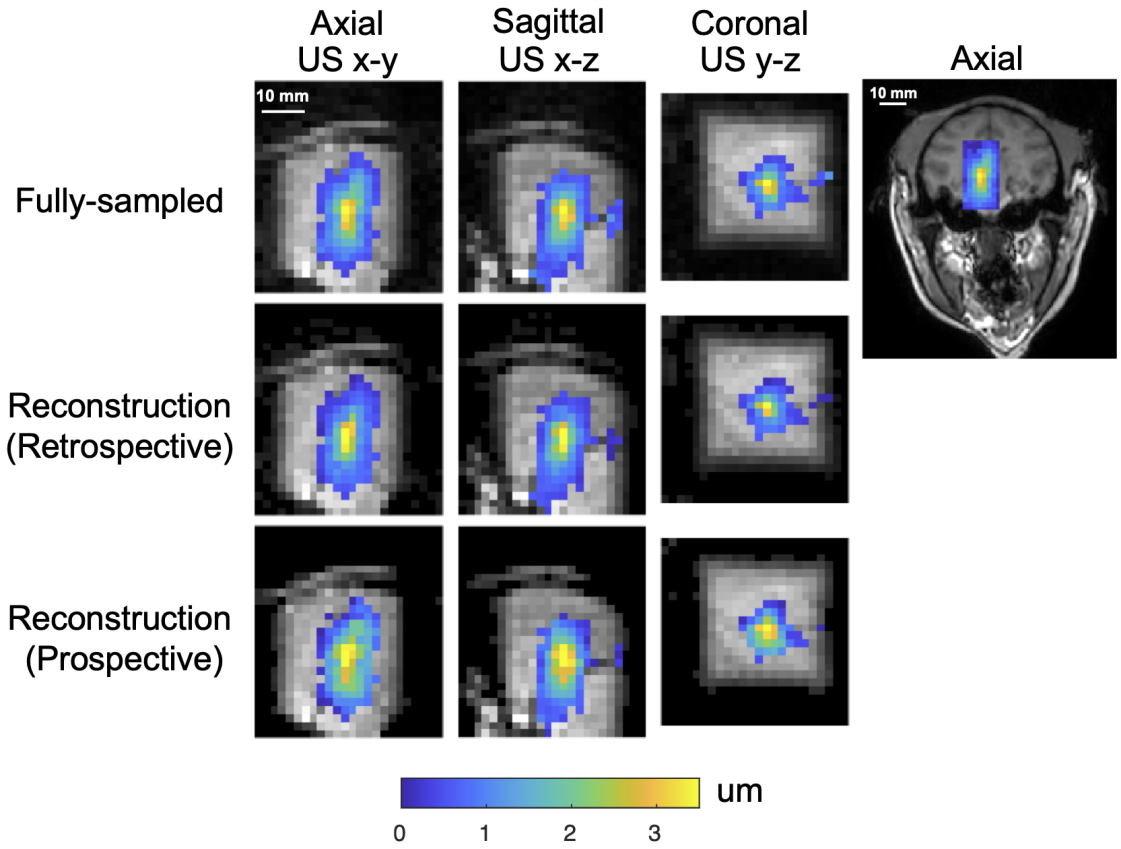

Figure 4.7: Macaque displacement maps overlaid on reconstructed magnitude images with a midbrain focus for neuromodulation. The right figure shows the position of zoomed-in displacement maps on the left in the axial plane (US x-y) of whole brain.

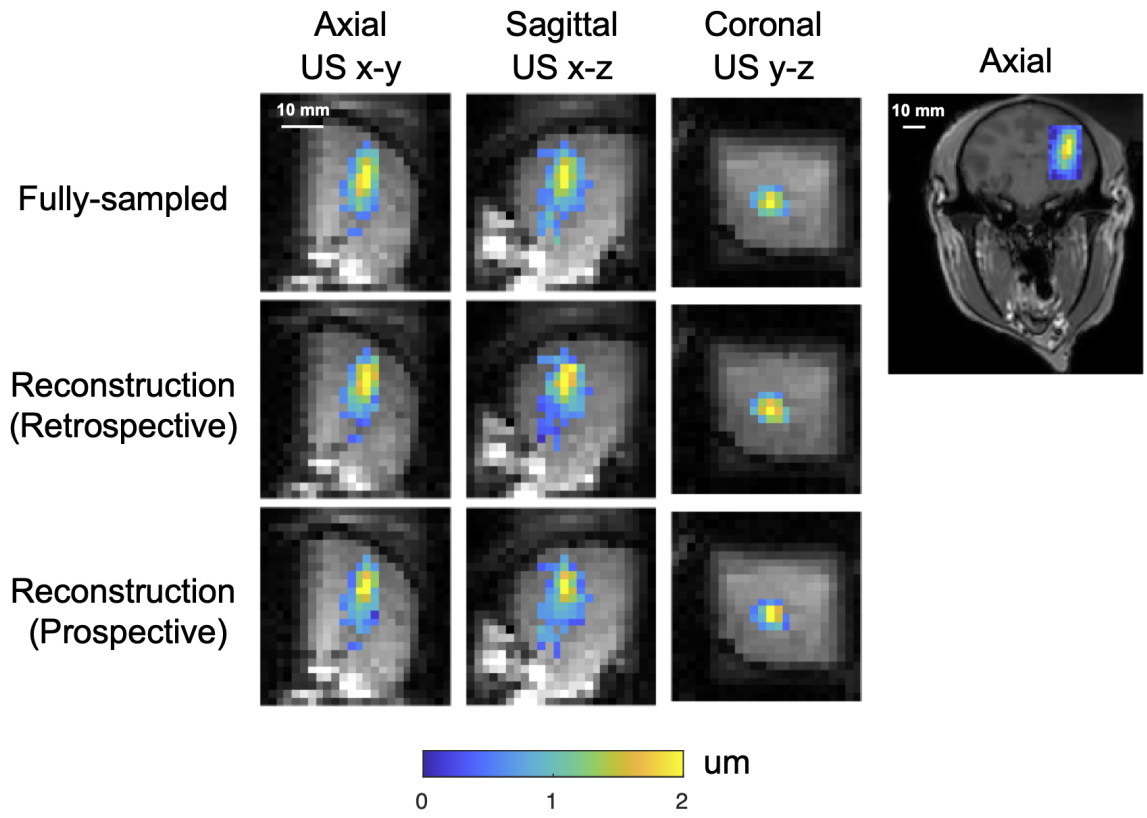

Figure 4.8: Macaque displacement maps overlaid on reconstructed magnitude images with a focus positioned in cortical grey matter for blood brain barrier opening. The right figure shows the position of zoomed-in displacement maps on the left in the axial plane (US x-y) of whole brain.

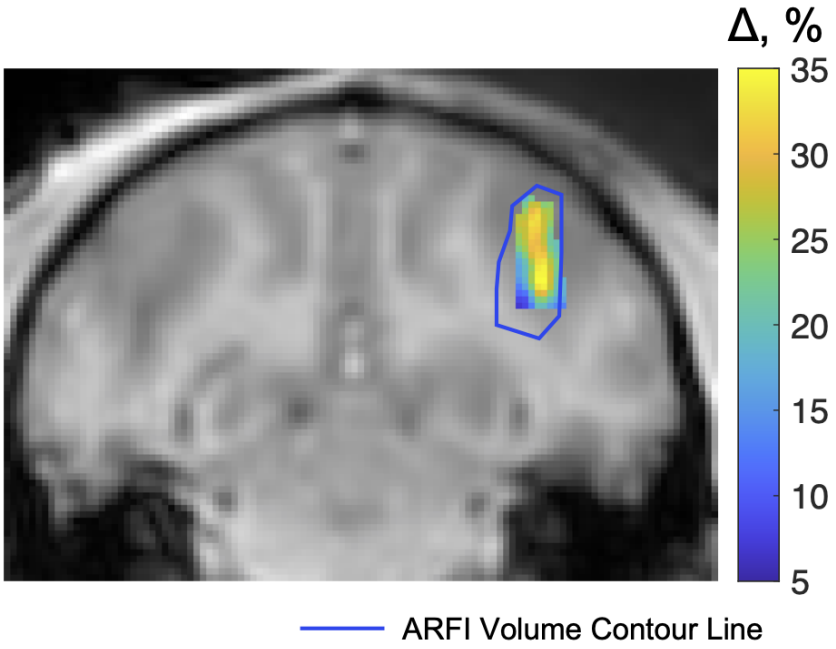

Figure 4.9: Gadolinium-based signal changes at region of blood-brain barrier disruption overlaid on a T_1-weighted image. The blue contour line indicates the 0.5-μm isocontour of the focus shown in Figure 4.8.

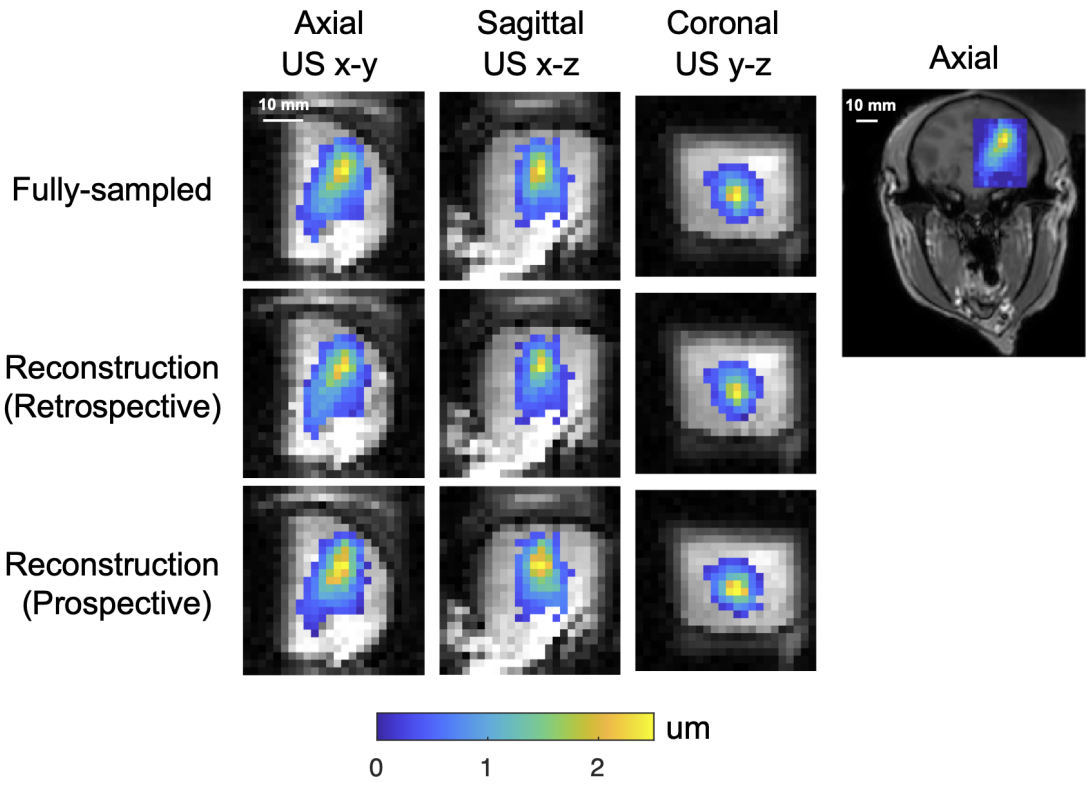

Figure 4.10: Another example of macaque displacement maps overlaid on reconstructed magnitude images with a focus positioned in cortical grey matter for blood brain barrier opening. The right figure shows the position of zoomed-in displacement maps on the left in the axial plane (US x-y) of whole brain.

CHAPTER 5

Conclusion and Future Work

5.1 Summary and Contributions

This work is aimed to further innovate and improve the techniques that visualize the therapeutic ultrasound in two different situations: free field measurements for safety and quality assurance of ultrasound transducers and beam visualization in in vivo brains for treatment planning.

Ahead of setting up FUS surgeries, it is required to know the information of the acoustic output of ultrasound transducers and check the consistency of the acoustic field for the safety and credibility of FUS treatments. Conventional instruments have several limitations. Hydrophones requires long measurement times, 3D translation stages as well as measured conditions such as temperature and water purity, and they are easily damaged. Radiation force balances cannot provide the acoustic pressure measurements, are limited to small FOV and erroneous at low acoustic power. Optical methods require sophisticated and expensive setup and can only provide qualitative measurements of acoustic pressure fields. In order to address these limitations, Chapter 3 describes a rapid imaging method that quantitatively characterizes the ultrasonic pressure fields of the ultrasound transducer. This method was demonstrated to map the RMS projected pressures in two dimensions under 10 s with the peak negative pressure varying from 1.5 to 9 MPa. The results showed that it could produce beam maps that closely matched optical hydrophone measurements that are thought to be the gold standard measurements in the field. The proposed method is based on the relatively new technique - BOS imaging. The hardware is simplified by allowing the beam to run continuously during acquisition. Deep learning techniques are used to solve the different inverse problem between blurring patterns and the projected pressure amplitudes. The developed technique provides an inexpensive, portable, and rapid 2D FUS beam mapping tool for quality assurance and developments in FUS systems and techniques. It offers substantial potentials for applications that are not well served by hydrophones when we are concerned about the speed, simplicity and low cost, such as measuring quickly changes in overall transducer output and detecting beam aberrations.

During the FUS surgery, ultrasound waves are distorted and shifted when the waves propagate through tissue or skull bones due to acoustical inhomogeneities. The distortion is likely to lead to the partial or complete destruction of the focal spot. Verifying if the FUS beam's focus is placed at the targeted spot is essential because off-target heating in the near- and far-fields of the ultrasound transducer can have deleterious effects. MRI can localize the focal spot with its good contrast, adequate spatial resolution and sensitivity to

temperatures. Taking account of the effects of distorted or shifted waves, we need to image a view that can cover the entire focus for the success of treatment with MRI. However, such a volumetric view requires long scan times. In addition, the brain is very sensitive to even small temperature rises, so heat deposition is a primary concern in applications of transcranial focused ultrasound. This dissertation tackled the above-described challenges. To enhance FUS procedures during treatment for nonthermal applications in the brain, Chapter 4 developed and validated a reduced-FOV 3D MR-ARFI pulse sequence jointly with a low-rank reconstruction for targeting transcranial focused ultrasound. It applied selective 90° and 180° RF pulses in two orthogonal dimensions to reduce FOV for minimized phase-encoding steps. The 'dead' time in the long TRs was used for the alternate acquisition of FUS-ON and FUS-OFF data, with a complementary k-space sampling pattern. The partial Fourier sampling and uniform undersampling were performed in two phase-encoding dimensions, which minimized the FUS duty cycle and further reduced scan times. A structured low-rank algorithm based on self-consistency and matching MR-ARFI image magnitudes was implemented to reconstruct images and calculate displacement maps in phantoms and living macaques' brains. This technique can image the entire focus in 3D within two minutes and keep a low FUS duty cycle of 0.85% to avoid heat deposition and undesirable bioeffects. It will improve the efficiency of targeting the FUS focus for the finding, resteering, and phase correction of the focus.

5.2 Future Work

5.2.1 CW-BOS System for Rapid FUS Beam Mapping

The developed CW-BOS system in Chapter 3 comprises only a water tank, a tablet and a camera for measurement of the RMS projected pressures. In future work, we can revise this system to make it portable by sealing the water tank and rigidly attaching the camera and the tablet to the tank, which could be set up and performed easily and faster than other conventional methods. The method has been proved to enable rapid and quantitative mapping of RMS projected pressure in two dimensions. One possible extension of this work is to reconstruct peak positive and negative pressures or a full cycle of the projected pressure waves at each spatial location in three dimensions. The modification of the system from 2D to 3D may require the background patterns displayed on the tablet rotated based on the back projection (Kremer et al., 2014, 2015).

Further, there are two potential sources of errors. Firstly, the proposed method assumed parallel rays between the background pattern and the camera without considering the refraction of light. Ray tracing algorithms (Glassner, 1989) and existing camera models (Barsky et al., 2003) may help to improve the generation of training sets and reduce the reconstruction errors. Secondly, the distance between the transducer focus and the background pattern may cause the mismatch of blurring patterns of training sets and actual acquired images, further leading to errors because of underfitting. The inputs of the current reconstruction approach

are single blurring patterns. One thing that may reduce errors is considering an entire photo containing a grid of blurring patterns as input and taking advantage of convolutional neural networks that can capture the complex spatial relationships between blurring patterns.

The CW-BOS system can enable rapidly repeated measurements across different experimental parameters when current methods are limited. It will optimize the routine to calibrate the ultrasound transducer, detect the aberrated ultrasound beams and check the consistency between different experiments. Moreover, it will facilitate the development of FUS research and techniques. For instance, ultrasound beam maps with and without skull aberration in ex vivo can be obtained with the established system, and the relation between two maps can be studied for acoustic properties of the skull.

5.2.2 Reduced-FOV 3D MR-ARFI

The reduced-FOV 3D MR-ARFI sequence and image reconstruction were come up with to minimize the time and FUS duty cycle for targeting the ultrasound focus. The scan time was two minutes and twenty seconds, and the FUS duty cycle was 0.85%. The displacement SNR and the scan efficiency could be further improved in the following ways. First, adjusting some scan parameters may achieve shorter scan times or improve the displacement SNR. For instance, the EPI factor of 3 can be increased to shorten scan time if off-resonance effects due to EPI can be ignored. Second, the combinations of the duration of MEGs, the time intervals between the gradient lobes, and the MEG strength may be further optimized for a higher displacement SNR according to the equation 2.37. Third, if a larger duty cycle or a higher acoustic power is allowed, the 'dead' time (450 ms) in each TR (500 ms) can be further utilized to acquire additional FUS-ON images. In this way, the effects of partial Fourier sampling or equidistant undersampling are likely to be alleviated, resulting in reduced errors of displacement measurements.

In future, the implemented 3D MR-ARFI sequence could be incorporated with optical tracking procedures(Phipps et al., 2019) to accurately place the FUS focus in the tissues, which will significantly increase the chances of success of MRgFUS treatments. The obtained displacement maps can also be used to refocus the beam in the presence of defocusing of FUS resulting from phase aberrations and attenuations caused by the bone for phase-arrayed transducers. The relative tissue displacement generated by each transducer element can be measured, and the corrective adjustments of phase and amplitude can be calculated to refocus the FUS beam (Grissom et al., 2012). Furthermore, the aberrated beam maps produced in phantoms or tissues, combined with the measured acoustic output in the free field, may be exploited to study the acoustic properties of tissues, which will be beneficial to treatment planning and treatment delivery during the clinic MRgFUS workflow, and the innovation and development of FUS techniques.

References

Aarnio, J., Clement, G. T., and Hynynen, K. (2005). A new ultrasound method for determining the acoustic phase shifts caused by the skull bone. *Ultrasound in medicine & biology*, 31(6):771–780.

Abadi, M., Barham, P., Chen, J., Chen, Z., Davis, A., Dean, J., Devin, M., Ghemawat, S., Irving, G., Isard, M., et al. (2016). Tensorflow: A system for large-scale machine learning. In *12th {USENIX} Symposium on Operating Systems Design and Implementation ({OSDI} 16)*, pages 265–283.

Abragam, A. (1961). *The principles of nuclear magnetism*. Number 32. Oxford university press.

Abrahao, A., Meng, Y., Llinas, M., Huang, Y., Hamani, C., Mainprize, T., Aubert, I., Heyn, C., Black, S. E., Hynynen, K., et al. (2019). First-in-human trial of blood–brain barrier opening in amyotrophic lateral sclerosis using mr-guided focused ultrasound. *Nature communications*, 10(1):1–9.

Arif, W. M., Elsinga, P. H., Gasca-Salas, C., Versluis, M., Martínez-Fernández, R., Dierckx, R. A., Borra, R. J., and Luurtsema, G. (2020). Focused ultrasound for opening blood-brain barrier and drug delivery monitored with positron emission tomography. *Journal of controlled release*, 324:303–316.

Aryal, M., Vykhodtseva, N., Zhang, Y.-Z., Park, J., and McDannold, N. (2013). Multiple treatments with liposomal doxorubicin and ultrasound-induced disruption of blood–tumor and blood–brain barriers improve outcomes in a rat glioma model. *Journal of controlled release*, 169(1-2):103–111.

Atcheson, B., Heidrich, W., and Ihrke, I. (2009). An evaluation of optical flow algorithms for background oriented schlieren imaging. *Experiments in fluids*, 46(3):467–476.

Atcheson, B., Ihrke, I., Heidrich, W., Tevs, A., Bradley, D., Magnor, M., and Seidel, H.-P. (2008). Time-resolved 3d capture of non-stationary gas flows. *ACM transactions on graphics (TOG)*, 27(5):1–9.

Auboiroux, V., Viallon, M., Roland, J., Hyacinthe, J.-N., Petrusca, L., Morel, D. R., Goget, T., Terraz, S., Gross, P., Becker, C. D., et al. (2012). Arfi-prepared mrghifu in liver: simultaneous mapping of arfi-displacement and temperature elevation, using a fast gre-epi sequence. *Magnetic resonance in medicine*, 68(3):932–946.

Baac, H. W., Ok, J. G., Maxwell, A., Lee, K.-T., Chen, Y.-C., Hart, A. J., Xu, Z., Yoon, E., and Guo, L. J. (2012). Carbon-nanotube optoacoustic lens for focused ultrasound generation and high-precision targeted therapy. *Sci Rep*, 2:989.

Baborovsky, V. M. (1979). Visualisation of ultrasound in solids. *Physics in Technology*, 10(4):171.

Bakay, L., Hueter, T., Ballantine, H., and Sosa, D. (1956). Ultrasonically produced changes in the blood-brain barrier. *AMA Archives of Neurology & Psychiatry*, 76(5):457–467.

Ballantine, H., Bell, E., and Manlapaz, J. (1960). Progress and problems in the neurological applications of focused ultrasound. *Journal of neurosurgery*, 17(5):858–876.

Bamber, J. C. and Hill, C. (1979). Ultrasonic attenuation and propagation speed in mammalian tissues as a function of temperature. *Ultrasound in medicine & biology*, 5(2):149–157.

Barsky, B. A., Horn, D. R., Klein, S. A., Pang, J. A., and Yu, M. (2003). Camera models and optical systems used in computer graphics: Part I, object-based techniques. In *International conference on computational science and its applications*, pages 246–255. Springer.

Benabid, A. L., Pollak, P., Hoffmann, D., Gervason, C., Hommel, M., Perret, J., De Rougemont, J., and Gao, D. (1991). Long-term suppression of tremor by chronic stimulation of the ventral intermediate thalamic nucleus. *The Lancet*, 337(8738):403–406.

Bergey, G. K., Morrell, M. J., Mizrahi, E. M., Goldman, A., King-Stephens, D., Nair, D., Srinivasan, S., Jobst, B., Gross, R. E., Shields, D. C., et al. (2015). Long-term treatment with responsive brain stimulation in adults with refractory partial seizures. *Neurology*, 84(8):810–817.

Bessonova, O. V. and Wilkens, V. (2013). Membrane hydrophone measurement and numerical simulation of HIFU fields up to developed shock regimes. *IEEE transactions on ultrasonics, ferroelectrics, and frequency control*, 60(2):290–300.

Bitton, R. R. and Pauly, K. R. B. (2014). Mr-acoustic radiation force imaging (mr-arfi) and susceptibility weighted imaging (swi) to visualize calcifications in ex vivo swine brain. *Journal of Magnetic Resonance Imaging*, 39(5):1294–1300.

Blackmore, J., Shrivastava, S., Sallet, J., Butler, C. R., and Cleveland, R. O. (2019). Ultrasound neuromodulation: a review of results, mechanisms and safety. *Ultrasound in medicine & biology*, 45(7):1509–1536.

Blaimer, M., Gutberlet, M., Kellman, P., Breuer, F. A., Köstler, H., and Griswold, M. A. (2009). Virtual coil concept for improved parallel MRI employing conjugate symmetric signals. *Magnetic Resonance in Medicine: An Official Journal of the International Society for Magnetic Resonance in Medicine*, 61(1):93–102.

Blana, A., Walter, B., Rogenhofer, S., and Wieland, W. F. (2004). High-intensity focused ultrasound for the treatment of localized prostate cancer: 5-year experience. *Urology*, 63(2):297–300.

Bloch, F. (1946). Nuclear induction. *Physical review*, 70(7-8):460.

Bloembergen, N., Purcell, E. M., and Pound, R. V. (1948). Relaxation effects in nuclear magnetic resonance absorption. *Physical review*, 73(7):679.

Bour, P., Ozenne, V., Rapacchi, S., Delcey, M., Schneider, R., Ben Hassen, W., et al. (2018). Volumetric and rapid mr-acoustic radiation force imaging using simultaneous multi-slice imaging. *International Society of Magnetic Resonance in Medicine, Paris*.

Bronson, N. R. (1969). An inexpensive schlieren apparatus. *Ultrasonics*, 7(1):67–70.

Brown, R. W., Cheng, Y.-C. N., Haacke, E. M., Thompson, M. R., and Venkatesan, R. (2014). *Magnetic resonance imaging: physical principles and sequence design*. John Wiley & Sons.

BT, R. I.-R. et al. (2011). Studio encoding parameters of digital television for standard 4: 3 and wide-screen 16: 9 aspect ratios.

Burgess, A., Shah, K., Hough, O., and Hynynen, K. (2015). Focused ultrasound-mediated drug delivery through the blood–brain barrier. *Expert review of neurotherapeutics*, 15(5):477–491.

Butterworth, I. and Shaw, A. (2010). Realtime acousto-optical QA methods for high intensity fields. In *Proceedings of the 39th Annual Symposium of the Ultrasonic Industry Association*, pages 1–5. IEEE.

Callé, S., Remenieras, J.-P., Bou Matar, O., Hachemi, M. E., and Patat, F. (2005). Temporal analysis of tissue displacement induced by a transient ultrasound radiation force. *The Journal of the Acoustical Society of America*, 118(5):2829–2840.

Canney, M. S., Bailey, M. R., Crum, L. A., Khokhlova, V. A., and Sapozhnikov, O. A. (2008). Acoustic characterization of high intensity focused ultrasound fields: A combined measurement and modeling approach. *The Journal of the Acoustical Society of America*, 124(4):2406–2420.

Catane, R., Beck, A., Inbar, Y., Rabin, T., Shabshin, N., Hengst, S., Pfeffer, R., Hanannel, A., Dogadkin, O., Liberman, B., et al. (2007). MR-guided focused ultrasound surgery (MRgFUS) for the palliation of pain in patients with bone metastases—preliminary clinical experience. *Annals of Oncology*, 18(1):163–167.

Chang, C., Firouzi, K., Park, K. K., Sarioglu, A. F., Nikoozadeh, A., Yoon, H.-S., Vaithilingam, S., Carver, T., and Khuri-Yakub, B. T. (2014). Acoustic lens for capacitive micromachined ultrasonic transducers. *Journal of Micromechanics and Microengineering*, 24(8):085007.

Chaplin, V., Phipps, M. A., and Caskey, C. F. (2018). A random phased-array for MR-guided transcranial ultrasound neuromodulation in Non-human Primates. *Physics in Medicine & Biology*, 63(10):105016.

Charlebois, T. and Pelton, R. (1995). Quantitative 2D and 3D Schlieren imaging for acoustic power and intensity measurements. *Medical Electronics*, pages 789–792.

Chaussy, C. and Thüroff, S. (2003). The status of high-intensity focused ultrasound in the treatment of localized prostate cancer and the impact of a combined resection. *Current Urology Reports*, 4(3):248–252.

Chen, J., Watkins, R., and Pauly, K. B. (2010). Optimization of encoding gradients for MR-ARFI. *Magnetic Resonance in Medicine: An Official Journal of the International Society for Magnetic Resonance in Medicine*, 63(4):1050–1058.

Chollet, F. et al. (2015). Keras.

Christensen, D. A. and Chao, A. (2007). A Pulsed Schlieren System for Visualizing Beams from Phased-Array HIFU Applicators. In *AIP Conference Proceedings*, volume 911, pages 15–19. American Institute of Physics.

Clement, G. and Hynynen, K. (2002). A non-invasive method for focusing ultrasound through the human skull. *Physics in Medicine & Biology*, 47(8):1219.

Cline, H. E., Hynynen, K., Schneider, E., Hardy, C. J., Maier, S. E., Watkins, R. D., and Jolesz, F. A. (1996). Simultaneous magnetic resonance phase and magnitude temperature maps in muscle. *Magnetic resonance in medicine*, 35(3):309–315.

Cline, H. E., Schenek, J., Hynynen, K., and Watkins, R. D. (1992). Mr-guided focused ultrasound surgery. *Journal of computer assisted tomography*, 16:956–956.

Corea, J. R., Flynn, A. M., Lechêne, B., Scott, G., Reed, G. D., Shin, P. J., Lustig, M., and Arias, A. C. (2016). Screen-printed flexible mri receive coils. *Nature communications*, 7:10839.

Curie, J. and Curie, P. (1881). Contractions et dilatations produites par des tensions électriques dans les cristaux hémièdres à faces inclinées. *Compt. Rend*, 93:1137–1140.

Dagrau, F., Rénier, M., Marchiano, R., and Coulouvrat, F. (2011). Acoustic shock wave propagation in a heterogeneous medium: A numerical simulation beyond the parabolic approximation. *The Journal of the Acoustical Society of America*, 130(1):20–32.

Dalecki, D. (2004). Mechanical bioeffects of ultrasound. *Annu. Rev. Biomed. Eng.*, 6:229–248.

Darrow, D. P. (2019). Focused ultrasound for neuromodulation. *Neurotherapeutics*, 16(1):88–99.

de Bever, J. T., Odéen, H., Todd, N., Farrer, A. I., and Parker, D. L. (2016). Evaluation of a three-dimensional MR acoustic radiation force imaging pulse sequence using a novel unbalanced bipolar motion encoding gradient. *Magnetic resonance in medicine*, 76(3):803–813.

Deffieux, T., Younan, Y., Wattiez, N., Tanter, M., Pouget, P., and Aubry, J.-F. (2013). Low-intensity focused ultrasound modulates monkey visuomotor behavior. *Current Biology*, 23(23):2430–2433.

Depoorter, J., Dewagter, C., Dedeene, Y., Thomsen, C., Stahlberg, F., and Achten, E. (1994). The proton-resonance-frequency-shift method compared with molecular diffusion for quantitative measurement of two-dimensional time-dependent temperature distribution in a phantom. *Journal of Magnetic Resonance, Series B*, 103(3):234–241.

Deshmane, A., Gulani, V., Griswold, M. A., and Seiberlich, N. (2012). Parallel MR imaging. *Journal of Magnetic Resonance Imaging*, 36(1):55–72.

Dewhirst, M. W., Viglianti, B., Lora-Michiels, M., Hanson, M., and Hoopes, P. (2003). Basic principles of thermal dosimetry and thermal thresholds for tissue damage from hyperthermia. *International journal of hyperthermia*, 19(3):267–294.

Di Biase, L., Falato, E., and Di Lazzaro, V. (2019). Transcranial focused ultrasound (tfus) and transcranial unfocused ultrasound (tus) neuromodulation: from theoretical principles to stimulation practices. *Frontiers in neurology*, page 549.

E Konofagou, E., Tunga, Y.-S., Choia, J., Deffieuxa, T., Baseria, B., and Vlachosa, F. (2012). Ultrasound-induced blood-brain barrier opening. *Current pharmaceutical biotechnology*, 13(7):1332–1345.

El-Sharkawy, A. M., Schär, M., Bottomley, P. A., and Atalar, E. (2006). Monitoring and correcting spatio-temporal variations of the mr scanner's static magnetic field. *Magnetic resonance materials in Physics, Biology and Medicine*, 19(5):223–236.

Elder, S. A. (1959). Cavitation microstreaming. *The Journal of the Acoustical Society of America*, 31(1):54–64.

Elhelf, I. S., Albahar, H., Shah, U., Oto, A., Cressman, E., and Almekkawy, M. (2018). High intensity focused ultrasound: the fundamentals, clinical applications and research trends. *Diagnostic and interventional imaging*, 99(6):349–359.

Elias, W. J., Huss, D., Voss, T., Loomba, J., Khaled, M., Zadicario, E., Frysinger, R. C., Sperling, S. A., Wylie, S., Monteith, S. J., Druzgal, J., Shah, B. B., Harrison, M., and Wintermark, M. (2013a). A Pilot Study of Focused Ultrasound Thalamotomy for Essential Tremor. *New Engl J Med*, 369(7):640–648.

Elias, W. J., Huss, D., Voss, T., Loomba, J., Khaled, M., Zadicario, E., Frysinger, R. C., Sperling, S. A., Wylie, S., Monteith, S. J., et al. (2013b). A pilot study of focused ultrasound thalamotomy for essential tremor. *New England Journal of Medicine*, 369(7):640–648.

Ellens, N. and Hynynen, K. (2014). Simulation study of the effects of near-and far-field heating during focused ultrasound uterine fibroid ablation using an electronically focused phased array: A theoretical analysis of patient safety. *Medical physics*, 41(7):072902.

Fahy, F. and Walker, J. (1998). *Fundamentals of noise and vibration*. CRC Press.

Fishman, P. S. and Frenkel, V. (2017). Focused ultrasound: an emerging therapeutic modality for neurologic disease. *Neurotherapeutics*, 14(2):393–404.

Flynn, H. (1964). Physical acoustics, ed. wp mason, 1b.

Fomenko, A., Neudorfer, C., Dallapiazza, R. F., Kalia, S. K., and Lozano, A. M. (2018). Low-intensity ultrasound neuromodulation: An overview of mechanisms and emerging human applications. *Brain stimulation*, 11(6):1209–1217.

Fowlkes, J. B., Abramowicz, J. S., Church, C. C., Holland, C. K., Miller, D. L., O'Brien, W. D., Sanghvi, N. T., Stratmeyer, M. E., Zachary, J. F., Deng, C. X., et al. (2008). American institute of ultrasound in medicine consensus report on potential bioeffects of diagnostic ultrasound: executive summary. *Journal of Ultrasound in Medicine*, 27(4):503–515.

Fram, E. K., Herfkens, R. J., Johnson, G. A., Glover, G. H., Karis, J. P., Shimakawa, A., Perkins, T. G., and Pelc, N. J. (1987). Rapid calculation of t1 using variable flip angle gradient refocused imaging. *Magnetic resonance imaging*, 5(3):201–208.

Fregni, F. and Pascual-Leone, A. (2007). Technology insight: noninvasive brain stimulation in neurology—perspectives on the therapeutic potential of rTMS and tDCS. *Nature clinical practice Neurology*, 3(7):383–393.

Freundlich, H., Söllner, K., and Rogowski, F. (1932). Einige biologische wirkungen von ultraschallwellen. *Klinische Wochenschrift*, 11(36):1512–1513.

Fry, F. J. and Barger, J. E. (1978). Acoustical properties of the human skull. *The Journal of the Acoustical Society of America*, 63(5):1576–1590.

Fry, W. J., Fry, F., Barnard, J., Krumins, R., and Brennan, J. (1955). Ultrasonic lesions in the mammalian central nervous system. *Science*, 122(3168):517–518.

Furusawa, H., Namba, K., Thomsen, S., Akiyama, F., Bendet, A., Tanaka, C., Yasuda, Y., and Nakahara, H. (2006). Magnetic resonance–guided focused ultrasound surgery of breast cancer: reliability and effectiveness. *Journal of the American College of Surgeons*, 203(1):54–63.

Gaur, P., Casey, K. M., Kubanek, J., Li, N., Mohammadjavadi, M., Saenz, Y., Glover, G. H., Bouley, D. M., and Pauly, K. B. (2020). Histologic safety of transcranial focused ultrasound neuromodulation and magnetic resonance acoustic radiation force imaging in rhesus macaques and sheep. *Brain stimulation*, 13(3):804–814.

Ghanouni, P., Butts Pauly, K., Elias, W. J., Henderson, J., Sheehan, J., Monteith, S., and Wintermark, M. (2015). Transcranial MRI-guided focused ultrasound: A review of the technologic and neurologic applications. *Am J Roentegnol*, 205(1):150–159.

Ghanouni, P., Dobrotwir, A., Bazzocchi, A., Bucknor, M., Bitton, R., Rosenberg, J., Telischak, K., Busacca, M., Ferrari, S., Albisinni, U., et al. (2017). Magnetic resonance-guided focused ultrasound treatment of extra-abdominal desmoid tumors: a retrospective multicenter study. *European radiology*, 27(2):732–740.

Glassner, A. S. (1989). *An introduction to ray tracing*. Elsevier.

Goldhahn, E. and Seume, J. (2007). The background oriented schlieren technique: Sensitivity, accuracy, resolution and application to a three-dimensional density field. *Experiments in Fluids*, 43(2-3):241–249.

Gopinath, R., Srinivasan, K., Umchid, S., Bansal, L., Daryoush, A., Lewin, P., and El-Sherif, M. (2007). P5f-2 improved fiber optic hydrophone sensors. In *2007 IEEE Ultrasonics Symposium Proceedings*, pages 2319–2322. IEEE.

Goss, S., Frizzell, L., and Dunn, F. (1979). Ultrasonic absorption and attenuation in mammalian tissues. *Ultrasound in medicine & biology*, 5(2):181–186.

Grissom, W. A., Kaye, E., Pauly, K. B., Zur, Y., Yeo, D., Medan, Y., and Davis, C. (2012). Rapid hifu autofocusing using the entire mr-arfi image. In *AIP Conference Proceedings*, volume 1503, pages 162–167. American Institute of Physics.

Grissom, W. A., Rieke, V., Holbrook, A. B., Medan, Y., Lustig, M., Santos, J., McConnell, M. V., and Pauly, K. B. (2010). Hybrid referenceless and multibaseline subtraction mr thermometry for monitoring thermal therapies in moving organs. *Medical physics*, 37(9):5014–5026.

Grüll, H. and Langereis, S. (2012). Hyperthermia-triggered drug delivery from temperature-sensitive liposomes using mri-guided high intensity focused ultrasound. *Journal of Controlled Release*, 161(2):317–327.

Haldar, J. P. (2013). Low-rank modeling of local k-space neighborhoods (LORAKS) for constrained MRI. *IEEE transactions on medical imaging*, 33(3):668–681.

Haller, J., Jenderka, K.-V., Durando, G., and Shaw, A. (2012). A comparative evaluation of three hydrophones and a numerical model in high intensity focused ultrasound fields. *The Journal of the Acoustical Society of America*, 131(2):1121–1130.

Hanafy, A. and Zanelli, C. (1991). Quantitative real-time pulsed schlieren imaging of ultrasonic waves. In *IEEE 1991 Ultrasonics Symposium*, pages 1223–1227. IEEE.

Hertzberg, Y., Hugeri, M., Navon, G., and Azhari, H. (2014). Rapid method for assessing relative tissue stiffness using mr acoustic radiation force imaging. *International journal of imaging systems and technology*, 24(1):103–110.

Hertzberg, Y., Volovick, A., Zur, Y., Medan, Y., Vitek, S., and Navon, G. (2010). Ultrasound focusing using magnetic resonance acoustic radiation force imaging: application to ultrasound transcranial therapy. *Medical physics*, 37(6Part1):2934–2942.

Hesley, G. K., Gorny, K. R., and Woodrum, D. A. (2013). Mr-guided focused ultrasound for the treatment of uterine fibroids. *Cardiovascular and interventional radiology*, 36(1):5–13.

Hill, C. (1972). Ultrasonic exposure thresholds for changes in cells and tissues. *The Journal of the Acoustical Society of America*, 52(2B):667–672.

Hindman, J. (1966). Proton resonance shift of water in the gas and liquid states. *The Journal of Chemical Physics*, 44(12):4582–4592.

Hocker, G. (1979). Fiber-optic sensing of pressure and temperature. *Applied optics*, 18(9):1445–1448.

Holbrook, A. B., Ghanouni, P., Santos, J. M., Medan, Y., and Butts Pauly, K. (2011). In vivo MR acoustic radiation force imaging in the porcine liver. *Medical physics*, 38(9):5081–5089.

Horn, B. K. and Schunck, B. G. (1981). Determining optical flow. *Artificial intelligence*, 17(1-3):185–203.

Horodyckid, C., Canney, M., Vignot, A., Boisgard, R., Drier, A., Huberfeld, G., François, C., Prigent, A., Santin, M. D., Adam, C., et al. (2017). Safe long-term repeated disruption of the blood-brain barrier using an implantable ultrasound device: a multiparametric study in a primate model. *Journal of Neurosurgery*, 126(4):1351–1361.

Huang, Y., Curiel, L., Kukic, A., Plewes, D. B., Chopra, R., and Hynynen, K. (2009). Mr acoustic radiation force imaging: in vivo comparison to ultrasound motion tracking. *Medical physics*, 36(6Part1):2016–2020.

Huber, P. E., Jenne, J. W., Rastert, R., Simiantonakis, I., Sinn, H.-P., Strittmatter, H.-J., von Fournier, D., Wannenmacher, M. F., and Debus, J. (2001). A new noninvasive approach in breast cancer therapy using magnetic resonance imaging-guided focused ultrasound surgery. *Cancer research*, 61(23):8441–8447.

Hynynen, K., McDannold, N., Mulkern, R. V., and Jolesz, F. A. (2000). Temperature monitoring in fat with mri. *Magnetic resonance in medicine*, 43(6):901–904.

Ilovitsh, A., Fite, B. Z., Ilovitsh, T., and Ferrara, K. W. (2019). Acoustic radiation force imaging using a single-shot spiral readout. *Physics in Medicine & Biology*, 64(12):125004.

Ishihara, Y., Calderon, A., Watanabe, H., Okamoto, K., Suzuki, Y., Kuroda, K., and Suzuki, Y. (1995). A precise and fast temperature mapping using water proton chemical shift. *Magnetic resonance in medicine*, 34(6):814–823.

Jacob, M., Mani, M. P., and Ye, J. C. (2020). Structured low-rank algorithms: Theory, magnetic resonance applications, and links to machine learning. *IEEE Signal Processing Magazine*, 37(1):54–68.

Jang, H. J., Lee, J.-Y., Lee, D.-H., Kim, W.-H., and Hwang, J. H. (2010). Current and future clinical applications of high-intensity focused ultrasound (hifu) for pancreatic cancer. *Gut and liver*, 4(Suppl 1):S57.

Jiang, X., Savchenko, O., Li, Y., Qi, S., Yang, T., Zhang, W., and Chen, J. (2018). A review of low-intensity pulsed ultrasound for therapeutic applications. *IEEE Transactions on Biomedical Engineering*, 66(10):2704–2718.

Jin, K. H., Lee, D., and Ye, J. C. (2016). A general framework for compressed sensing and parallel MRI using annihilating filter based low-rank Hankel matrix. *IEEE Transactions on Computational Imaging*, 2(4):480–495.

Johns, L. D., Straub, S. J., and Howard, S. M. (2007). Analysis of effective radiating area, power, intensity, and field characteristics of ultrasound transducers. *Archives of physical medicine and rehabilitation*, 88(1):124–129.

Jolesz, F. A. (2009). Mri-guided focused ultrasound surgery. *Annual review of medicine*, 60:417–430.

Jolesz, F. A. and Hynynen, K. H. (2007). *MRI-guided focused ultrasound surgery*. CRC Press.

Kaye, E. A., Chen, J., and Pauly, K. B. (2011). Rapid MR-ARFI method for focal spot localization during focused ultrasound therapy. *Magnetic resonance in medicine*, 65(3):738–743.

Kaye, E. A. and Pauly, K. B. (2013). Adapting MRI acoustic radiation force imaging for in vivo human brain focused ultrasound applications. *Magnetic resonance in medicine*, 69(3):724–733.

Khraiche, M. L., Phillips, W. B., Jackson, N., and Muthuswamy, J. (2008). Ultrasound induced increase in excitability of single neurons. In *2008 30th Annual International Conference of the IEEE Engineering in Medicine and Biology Society*, pages 4246–4249. IEEE.

Kim, H., Chiu, A., Lee, S. D., Fischer, K., and Yoo, S.-S. (2014). Focused ultrasound-mediated non-invasive brain stimulation: examination of sonication parameters. *Brain stimulation*, 7(5):748–756.

Kim, S. J., Roh, D., Jung, H. H., Chang, W. S., Kim, C.-H., and Chang, J. W. (2018). A study of novel bilateral thermal capsulotomy with focused ultrasound for treatment-refractory obsessive–compulsive disorder: 2-year follow-up. *Journal of Psychiatry and Neuroscience*, 43(5):327–337.

King, R. L., Brown, J. R., Newsome, W. T., and Pauly, K. B. (2013). Effective parameters for ultrasound-induced in vivo neurostimulation. *Ultrasound in medicine & biology*, 39(2):312–331.

Kinoshita, M., McDannold, N., Jolesz, F. A., and Hynynen, K. (2006). Targeted delivery of antibodies through the blood–brain barrier by mri-guided focused ultrasound. *Biochemical and biophysical research communications*, 340(4):1085–1090.

Kobus, T. and McDannold, N. (2015). Update on Clinical Magnetic Resonance–Guided Focused Ultrasound Applications. *Magnetic Resonance Imaging Clinics*, 23(4):657–667.

Koponen, E., Leskinen, J. J., Tarvainen, T., and Pulkkinen, A. (2019). Acoustic pressure field estimation methods for synthetic schlieren tomography. *J Acoust Soc Am*, 145:2470.

Kreider, W., Yuldashev, P. V., Sapozhnikov, O. A., Farr, N., Partanen, A., Bailey, M. R., and Khokhlova, V. A. (2013). Characterization of a multi-element clinical HIFU system using acoustic holography and nonlinear modeling. *IEEE transactions on ultrasonics, ferroelectrics, and frequency control*, 60(8):1683–1698.

Kremer, M., Caskey, C., and Grissom, W. (2014). Background-oriented schlieren imaging and tomography for rapid measurement of fus pressure fields: initial results. *Proceedings 4th Int Symp on Focused Ultrasound*, 3(1):1–2.

Kremer, M., Caskey, C., and Grissom, W. (2015). Rapid characterization of focused ultrasound pressure fields using background-oriented schlieren tomography. *Proceedings BMES*, 3(1):1–2.

Kubanek, J. (2018). Neuromodulation with transcranial focused ultrasound. *Neurosurgical focus*, 44(2):E14.

Kuroda, K. (2005). Non-invasive mr thermography using the water proton chemical shift. *International journal of hyperthermia*, 21(6):547–560.

Kuroda, K., Mulkern, R., Oshio, K., Panych, L., Nakai, T., Moriya, T., Okuda, S., Hynynen, K., and Joles, F. (2000). Temperature mapping using the water proton chemical shift: self-referenced method with echo-planar spectroscopic imaging. *Magnetic Resonance in Medicine: An Official Journal of the International Society for Magnetic Resonance in Medicine*, 43(2):220–225.

Kyriakou, A., Neufeld, E., Werner, B., Paulides, M. M., Szekely, G., and Kuster, N. (2014). A review of numerical and experimental compensation techniques for skull-induced phase aberrations in transcranial focused ultrasound. *International Journal of Hyperthermia*, 30(1):36–46.

Lalonde, R. J., Worthington, A., and Hunt, J. W. (1993). Field conjugate acoustic lenses for ultrasound hyperthermia. *IEEE transactions on ultrasonics, ferroelectrics, and frequency control*, 40(5):592–602.

Lauterbur, P. C. (1973). Image formation by induced local interactions: examples employing nuclear magnetic resonance. *nature*, 242(5394):190–191.

Lee, H.-L., Kuo, C.-C., Tsai, J.-T., Chen, C.-Y., Wu, M.-H., and Chiou, J.-F. (2017). Magnetic resonance-guided focused ultrasound versus conventional radiation therapy for painful bone metastasis: a matched-pair study. *JBJS*, 99(18):1572–1578.

Lele, P. (1977). Thresholds and mechanisms of ultrasonic damage to "organized" animal tissues. In *Symposium on biological effects and characterizations of ultrasound sources*, volume 78, page 8048. US Department of Health, Education, and Welfare HEW Publication (FDA) 78-8048.

Li, Y., Lee, J., Long, X., Qiao, Y., Ma, T., He, Q., Cao, P., Zhang, X., and Zheng, H. (2020). A Magnetic Resonance-guided Focused Ultrasound Neuromodulation System with a Whole Brain Coil Array for Nonhuman Primates at 3 T. *IEEE Transactions on Medical Imaging*, 39(12):4401–4412.

Liang, H., Tang, J., and Halliwell, M. (2010). Sonoporation, drug delivery, and gene therapy. *Proceedings of the Institution of Mechanical Engineers, Part H: Journal of Engineering in Medicine*, 224(2):343–361.

Lighthill, J. (1978). Acoustic streaming. *Journal of sound and vibration*, 61(3):391–418.

Lipsman, N., Meng, Y., Bethune, A. J., Huang, Y., Lam, B., Masellis, M., Herrmann, N., Heyn, C., Aubert, I., Boutet, A., Smith, G. S., Hynynen, K., and Black, S. E. (2018). Blood–brain barrier opening in Alzheimer's disease using MR-guided focused ultrasound. *Nat Comm*, 9:2336.

Lozinski, T., Filipowska, J., Pyka, M., Baczkowska, M., and Ciebiera, M. (2021). Magnetic resonance-guided high-intensity ultrasound (MR-HIFU) in the treatment of symptomatic uterine fibroids—five-year experience. *Ginekologia Polska*.

Lynn, J. G. and Putnam, T. J. (1944). Histology of cerebral lesions produced by focused ultrasound. *The American journal of pathology*, 20(3):637.

Lynn, J. G., Zwemer, R. L., Chick, A. J., and Miller, A. E. (1942). A new method for the generation and use of focused ultrasound in experimental biology. *The Journal of general physiology*, 26(2):179.

Madsen, E. L., Zagzebski, J. A., Banjavie, R. A., and Jutila, R. E. (1978). Tissue mimicking materials for ultrasound phantoms. *Medical physics*, 5(5):391–394.

Magara, A., Bühler, R., Moser, D., Kowalski, M., Pourtehrani, P., and Jeanmonod, D. (2014). First experience with mr-guided focused ultrasound in the treatment of parkinson's disease. *Journal of Therapeutic Ultrasound*, 2(1):1–8.

Maimbourg, G., Houdouin, A., Deffieux, T., Tanter, M., and Aubry, J.-F. (2018). 3d-printed adaptive acoustic lens as a disruptive technology for transcranial ultrasound therapy using single-element transducers. *Physics in Medicine & Biology*, 63(2):025026.

Mainprize, T., Lipsman, N., Huang, Y., Meng, Y., Bethune, A., Ironside, S., Heyn, C., Alkins, R., Trudeau, M., Sahgal, A., et al. (2019). Blood-brain barrier opening in primary brain tumors with non-invasive mr-guided focused ultrasound: a clinical safety and feasibility study. *Scientific reports*, 9(1):1–7.

Maruvada, S., Harris, G. R., Herman, B. A., and King, R. L. (2007). Acoustic power calibration of high-intensity focused ultrasound transducers using a radiation force technique. *The Journal of the Acoustical Society of America*, 121(3):1434–1439.

Matsumoto, R., Oshio, K., and Jolesz, F. A. (1992). Monitoring of laser and freezinginduced ablation in the liver with t1-weighted mr imaging. *Journal of Magnetic Resonance Imaging*, 2(5):555–562.

McDannold, N. and Hynynen, K. (2006). Quality assurance and system stability of a clinical MRI-guided focused ultrasound system: Four-year experience. *Medical physics*, 33(11):4307–4313.

McDannold, N. and Maier, S. E. (2008). Magnetic resonance acoustic radiation force imaging. *Medical physics*, 35(8):3748–3758.

McDannold, N., Vykhodtseva, N., Raymond, S., Jolesz, F. A., and Hynynen, K. (2005). Mri-guided targeted blood-brain barrier disruption with focused ultrasound: histological findings in rabbits. *Ultrasound in medicine & biology*, 31(11):1527–1537.

McGivney, D. F., Pierre, E., Ma, D., Jiang, Y., Saybasili, H., Gulani, V., and Griswold, M. A. (2014). Svd compression for magnetic resonance fingerprinting in the time domain. *IEEE transactions on medical imaging*, 33(12):2311–2322.

Meier, G. E. A. (2002). Computerized background-oriented schlieren. *Experiments in Fluids*, 33(1):181–187.

Meng, Y., Hynynen, K., and Lipsman, N. (2021). Applications of focused ultrasound in the brain: from thermoablation to drug delivery. *Nature Reviews Neurology*, 17(1):7–22.

Meng, Y., Pople, C. B., Lea-Banks, H., Abrahao, A., Davidson, B., Suppiah, S., Vecchio, L. M., Samuel, N., Mahmud, F., Hynynen, K., et al. (2019). Safety and efficacy of focused ultrasound induced blood-brain barrier opening, an integrative review of animal and human studies. *Journal of Controlled Release*, 309:25–36.

Miller, D. B. and O'Callaghan, J. P. (2017). New horizons for focused ultrasound (fus)–therapeutic applications in neurodegenerative diseases. *Metabolism*, 69:S3–S7.

Miller, D. L., Smith, N. B., Bailey, M. R., Czarnota, G. J., Hynynen, K., Makin, I. R. S., and of the American Institute of Ultrasound in Medicine, B. C. (2012). Overview of therapeutic ultrasound applications and safety considerations. *Journal of ultrasound in medicine*, 31(4):623–634.

Moosa, S., Martínez-Fernández, R., Elias, W. J., Del Alamo, M., Eisenberg, H. M., and Fishman, P. S. (2019). The role of high-intensity focused ultrasound as a symptomatic treatment for parkinson's disease. *Movement Disorders*, 34(9):1243–1251.

Morris, P., Hurrell, A., Shaw, A., Zhang, E., and Beard, P. (2009). A fabry–pérot fiber-optic ultrasonic hydrophone for the simultaneous measurement of temperature and acoustic pressure. *The Journal of the Acoustical Society of America*, 125(6):3611–3622.

Mougenot, C., Pichardo, S., Engler, S., Waspe, A., Colas, E. C., and Drake, J. M. (2016). A rapid magnetic resonance acoustic radiation force imaging sequence for ultrasonic refocusing. *Physics in Medicine & Biology*, 61(15):5724.

Mougenot, C., Waspe, A., Looi, T., and Drake, J. M. (2015). Variable ultrasound trigger delay for improved magnetic resonance acoustic radiation force imaging. *Physics in Medicine & Biology*, 61(2):712.

Nakamura, T., Iwasaki, R., Yoshizawa, S., and Umemura, S.-i. (2018). Quantitative measurement of ultrasonic pressure field using combination of optical phase contrast and nonlinear acoustic holography methods. *Japanese Journal of Applied Physics*, 57(7S1):07LB13.

Naor, O., Krupa, S., and Shoham, S. (2016). Ultrasonic neuromodulation. *Journal of neural engineering*, 13(3):031003.

Neumann, T. and Ermert, H. (2006). Schlieren visualization of ultrasonic wave fields with high spatial resolution. *Ultrasonics*, 44:e1561–e1566.

Newman, D. R. (1973). Ultrasonic schlieren system using a pulsed gas laser. *IEEE Transactions on Sonics and Ultrasonics*, 20(3):282–284.

Nightingale, K. (2011). Acoustic radiation force impulse (arfi) imaging: a review. *Current medical imaging*, 7(4):328–339.

Odéen, H., de Bever, J., Hofstetter, L. W., and Parker, D. L. (2019). Multiple-point magnetic resonance acoustic radiation force imaging. *Magnetic resonance in medicine*, 81(2):1104–1117.

Odéen, H. and Parker, D. L. (2019). Magnetic resonance thermometry and its biological applications–physical principles and practical considerations. *Progress in nuclear magnetic resonance spectroscopy*, 110:34–61.

Ongie, G. and Jacob, M. (2015). Recovery of piecewise smooth images from few fourier samples. In *2015 International Conference on Sampling Theory and Applications (SampTA)*, pages 543–547. IEEE.

Ongie, G. and Jacob, M. (2016). A fast algorithm for structured low-rank matrix recovery with applications to undersampled mri reconstruction. In *2016 IEEE 13th International Symposium on Biomedical Imaging (ISBI)*, pages 522–525. IEEE.

Ongie, G. and Jacob, M. (2017). A fast algorithm for convolutional structured low-rank matrix recovery. *IEEE transactions on computational imaging*, 3(4):535–550.

Ozenne, V., Constans, C., Bour, P., Santin, M. D., Valabrègue, R., Ahnine, H., Pouget, P., Lehéricy, S., Aubry, J.-F., and Quesson, B. (2020). Mri monitoring of temperature and displacement for transcranial focus ultrasound applications. *Neuroimage*, 204:116236.

O'Reilly, M. A. and Hynynen, K. (2010). A pvdf receiver for ultrasound monitoring of transcranial focused ultrasound therapy. *IEEE transactions on Biomedical Engineering*, 57(9):2286–2294.

Palmeri, M. L. and Nightingale, K. R. (2011). Acoustic radiation force-based elasticity imaging methods. *Interface focus*, 1(4):553–564.

Paquin, R., Vignaud, A., Marsac, L., Younan, Y., Lehéricy, S., Tanter, M., and Aubry, J.-F. (2013). Keyhole acceleration for magnetic resonance acoustic radiation force imaging (MR ARFI). *Magnetic resonance imaging*, 31(10):1695–1703.

Parker, D. L. (1984). Applications of nmr imaging in hyperthermia: an evaluation of the potential for localized tissue heating and noninvasive temperature monitoring. *IEEE transactions on biomedical engineering*, (1):161–167.

Parsons, J. E., Cain, C. A., and Fowlkes, J. B. (2006). Cost-effective assembly of a basic fiber-optic hydrophone for measurement of high-amplitude therapeutic ultrasound fields. *The Journal of the Acoustical Society of America*, 119(3):1432–1440.

Patrick, J. T., Nolting, M. N., Goss, S. A., Dines, K. A., Clendenon, J. L., Rea, M. A., and Heimburger, R. F. (1990). Ultrasound and the blood-brain barrier. In *Consensus on Hyperthermia for the 1990s*, pages 369–381. Springer.

Pauly, J., Le Roux, P., Nishimura, D., and Macovski, A. (1991). Parameter relations for the Shinnar-Le Roux selective excitation pulse design algorithm (NMR imaging). *IEEE transactions on medical imaging*, 10(1):53–65.

Pauly, K. B. (2015). Magnetic resonance acoustic radiation force (impulse) imaging (MR-ARFI). *Journal of Therapeutic Ultrasound*, 3(1):1–1.

Payne, A., Chopra, R., Ellens, N., Chen, L., Ghanouni, P., Sammet, S., Diederich, C., Ter Haar, G., Parker, D., Moonen, C., et al. (2021). Aapm task group 241: A medical physicist's guide to mri-guided focused ultrasound body systems. *Medical physics*, 48(9):e772–e806.

Phillips, R. L. (1980). Proposed fiber-optic acoustical probe. *Optics letters*, 5(7):318–320.

Phipps, M. A., Jonathan, S. V., Yang, P.-F., Chaplin, V., Chen, L. M., Grissom, W. A., and Caskey, C. F. (2019). Considerations for ultrasound exposure during transcranial MR acoustic radiation force imaging. *Scientific reports*, 9(1):1–11.

Pinton, G. F. (2007). *Numerical methods for nonlinear wave propagation in ultrasound*. Duke University.

Pitts, T. A. and Greenleaf, J. F. (2000). Three-dimensional optical measurement of instantaneous pressure. *The Journal of the Acoustical Society of America*, 108(6):2873–2883.

Pitts, T. A., Greenleaf, J. F., Lu, J.-Y. L. J.-Y., and Kinnick, R. R. (1994). Tomographic Schlieren imaging for measurement of beam pressure and intensity. In *1994 Proceedings of IEEE Ultrasonics Symposium*, volume 3, pages 1665–1668. IEEE.

Pitts, T. A., Sagers, A., and Greenleaf, J. F. (2001). Optical phase contrast measurement of ultrasonic fields. *IEEE transactions on ultrasonics, ferroelectrics, and frequency control*, 48(6):1686–1694.

Poorman, M. E., Chaplin, V. L., Wilkens, K., Dockery, M. D., Giorgio, T. D., Grissom, W. A., and Caskey, C. F. (2016). Open-source, small-animal magnetic resonance-guided focused ultrasound system. *Journal of therapeutic ultrasound*, 4(1):1–16.

Poorter, J. D., Wagter, C. D., Deene, Y. D., Thomsen, C., Ståhlberg, F., and Achten, E. (1995). Noninvasive mri thermometry with the proton resonance frequency (prf) method: in vivo results in human muscle. *Magnetic resonance in medicine*, 33(1):74–81.

Prato, F., Drost, D., Keys, T., Laxon, P., Comissiong, B., and Sestini, E. (1986). Optimization of signal-to-noise ratio in calculated t1 images derived from two spin-echo images. *Magnetic resonance in medicine*, 3(1):63–75.

Pulkkinen, A., Leskinen, J. J., and Tiihonen, A. (2017). Ultrasound field characterization using synthetic schlieren tomography. *The Journal of the Acoustical Society of America*, 141(6):4600–4609.

Purcell, E. M., Torrey, H. C., and Pound, R. V. (1946). Resonance absorption by nuclear magnetic moments in a solid. *Physical review*, 69(1-2):37.

Qiao, Y., Zou, C., Cheng, C., Tie, C., Wan, Q., Peng, H., Liang, D., Liu, X., and Zheng, H. (2020). Simultaneous acoustic radiation force imaging and mr thermometry based on a coherent echo-shifted sequence. *Quantitative Imaging in Medicine and Surgery*, 10(9):1823.

Quesson, B., de Zwart, J. A., and Moonen, C. T. (2000). Magnetic resonance temperature imaging for guidance of thermotherapy. *Journal of Magnetic Resonance Imaging: An Official Journal of the International Society for Magnetic Resonance in Medicine*, 12(4):525–533.

Raffel, M. (2015). Background-oriented schlieren (bos) techniques. *Experiments in Fluids*, 56(3):1–17.

Raman, C. and Nagendra Nath, N. (1935). The diffraction of light by sound waves of high frequency: Part ii. In *Proceedings of the Indian Academy of Sciences-Section A*, volume 2, pages 413–420. Springer.

Raman, C. V. and Venkataraman, K. (1939). Determination of the adiabatic piezo-optic coefficient of liquids. *Proceedings of the Royal Society of London. Series A. Mathematical and Physical Sciences*, 171(945):137–147.

Reibold, R. (1987). Light diffraction tomography applied to the investigation of ultrasonic fields. Part II: Standing waves. *Acta Acustica united with Acustica*, 63(4):283–289.

Reibold, R. and Molkenstruck, W. (1984). Light diffraction tomography applied to the investigation of ultrasonic fields. Part I: Continuous waves. *Acta Acustica united with Acustica*, 56(3):180–192.

Reichel, E. K., Schneider, S. C., and Zagar, B. G. (2005). Characterization of ultrasonic transducers using the Schlieren–technique. In *2005 IEEE Instrumentationand Measurement Technology Conference Proceedings*, volume 3, pages 1956–1960. IEEE.

Richard, H. and Raffel, M. (2001). Principle and applications of the background oriented Schlieren (BOS) method. *Measurement Science and Technology*, 12(9):1576.

Rieke, V. (2011). Mr thermometry. *Interventional Magnetic Resonance Imaging*, pages 271–288.

Rieke, V., Kinsey, A. M., Ross, A. B., Nau, W. H., Diederich, C. J., Sommer, G., and Pauly, K. B. (2007). Referenceless mr thermometry for monitoring thermal ablation in the prostate. *IEEE transactions on medical imaging*, 26(6):813–821.

Riley, W. A. and Klein, W. R. (1967). Piezo-optic coefficients of liquids. *The Journal of the Acoustical Society of America*, 42(6):1258–1261.

Ringold, S. (2004). Fda approves ultrasound fibroid therapy. *Jama*, 292(23):2826–2826.

Rusanov, V. (1970). On difference schemes of third order accuracy for nonlinear hyperbolic systems. *Journal of Computational Physics*, 5(3):507–516.

Sarvazyan, A. P., Rudenko, O. V., Swanson, S. D., Fowlkes, J. B., and Emelianov, S. Y. (1998). Shear wave elasticity imaging: a new ultrasonic technology of medical diagnostics. *Ultrasound in medicine & biology*, 24(9):1419–1435.

Schlesinger, D., Benedict, S., Diederich, C., Gedroyc, W., Klibanov, A., and Larner, J. (2013). Mr-guided focused ultrasound surgery, present and future. *Medical physics*, 40(8):080901.

Schmitz, A., Gianfelice, D., Daniel, B., Mali, W., and Van den Bosch, M. (2008). Image-guided focused ultrasound ablation of breast cancer: current status, challenges, and future directions. *European radiology*, 18(7):1431–1441.

Schneider, B. and Shung, K. K. (1996). Quantitative analysis of pulsed ultrasonic beam patterns using a Schlieren system. *IEEE transactions on ultrasonics, ferroelectrics, and frequency control*, 43(6):1181–1186.

Schneider, J. T., Kalayciyan, R., Haas, M., Herrmann, S. R., Ruhm, W., Hennig, J., and Ullmann, P. (2013). Inner-volume imaging in vivo using three-dimensional parallel spatially selective excitation. *Magnetic resonance in medicine*, 69(5):1367–1378.

Sharma, A., Lustig, M., and Grissom, W. A. (2016). Root-flipped multiband refocusing pulses. *Magnetic resonance in medicine*, 75(1):227–237.

Sheikov, N., McDannold, N., Sharma, S., and Hynynen, K. (2008). Effect of focused ultrasound applied with an ultrasound contrast agent on the tight junctional integrity of the brain microvascular endothelium. *Ultrasound in medicine & biology*, 34(7):1093–1104.

Sheybani, N. D. and Price, R. J. (2019). Perspectives on recent progress in focused ultrasound immunotherapy. *Theranostics*, 9(25):7749.

Shin, P. J., Larson, P. E., Ohliger, M. A., Elad, M., Pauly, J. M., Vigneron, D. B., and Lustig, M. (2014). Calibrationless parallel imaging reconstruction based on structured low-rank matrix completion. *Magnetic resonance in medicine*, 72(4):959–970.

Shou, W., Huang, X., Duan, S., Xia, R., Shi, Z., Geng, X., and Li, F. (2006). Acoustic power measurement of high intensity focused ultrasound in medicine based on radiation force. *Ultrasonics*, 44:e17–e20.

Skudrzyk, E. (1971). The wave equation in cylindrical coordinates and its applications. In *The foundations of acoustics*, pages 423–454. Springer.

Smith, S. W. and Thurstone, F. L. (1974). Schlieren study of pulsed ultrasound transmission through human skull. *Journal of Clinical Ultrasound*, 2(1):55–59.

Souchon, R., Salomir, R., Beuf, O., Milot, L., Grenier, D., Lyonnet, D., Chapelon, J.-Y., and Rouvière, O. (2008). Transient mr elastography (t-mre) using ultrasound radiation force: theory, safety, and initial experiments in vitro. *Magnetic Resonance in Medicine: An Official Journal of the International Society for Magnetic Resonance in Medicine*, 60(4):871–881.

Sridhar, D. and Kohi, M. P. (2018). Updates on MR-guided focused ultrasound for symptomatic uterine fibroids. In *Seminars in interventional radiology*, volume 35, pages 017–022. Thieme Medical Publishers.

Stavarache, M. A., Chazen, J. L., and Kaplitt, M. G. (2021). Innovative Applications of MR-Guided Focused Ultrasound for Neurological Disorders. *World Neurosurgery*, 145:581–589.

Stewart, E. A., Gedroyc, W. M., Tempany, C. M., Quade, B. J., Inbar, Y., Ehrenstein, T., Shushan, A., Hindley, J. T., Goldin, R. D., David, M., et al. (2003). Focused ultrasound treatment of uterine fibroid tumors: safety and feasibility of a noninvasive thermoablative technique. *American journal of obstetrics and gynecology*, 189(1):48–54.

Stewart, E. A., Rabinovici, J., Tempany, C. M., Inbar, Y., Regan, L., Gastout, B., Hesley, G., Kim, H. S., Hengst, S., and Gedroye, W. M. (2006). Clinical outcomes of focused ultrasound surgery for the treatment of uterine fibroids. *Fertility and sterility*, 85(1):22–29.

Szabo, T. L. (2004). *Diagnostic ultrasound imaging: inside out*. Academic press.

Temkin, S. and Temkin, S. (1981). *Elements of acoustics*. Wiley New York.

Ter Haar, G. (1999). Therapeutic ultrasound. *European Journal of ultrasound*, 9(1):3–9.

Ter Haar, G. (2013). Safety first: Progress in calibrating high-intensity focused ultrasound treatments. *Imaging in Medicine*, 5(6):567–575.

Thüroff, Stefan and Chaussy, Christian and Vallancien, Guy and Wieland, Wolfgang and Kiel, Hans J and Le Duc, Alain and Desgrandchamps, François and De La Rosette, Jean JMCH and Gelet, Albert, j. (2003). High-intensity focused ultrasound and localized prostate cancer: efficacy results from the European multicentric study. 17(8):673–677.

Tieleman, T. and Hinton, G. (2012). Lecture 6.5-rmsprop: Divide the gradient by a running average of its recent magnitude. *COURSERA: Neural networks for machine learning*, 4(2):26–31.

Tipnis, T. J., Finnis, M. V., Knowles, K., and Bray, D. (2013). Density measurements for rectangular free jets using background-oriented schlieren. *The Aeronautical Journal*, 117(1194):771–785.

Todd, N., McDannold, N., and Borsook, D. (2020). Targeted manipulation of pain neural networks: The potential of focused ultrasound for treatment of chronic pain. *Neuroscience & Biobehavioral Reviews*, 115:238–250.

Torr, G. (1984). The acoustic radiation force. *American Journal of Physics*, 52(5):402–408.

Treeby, B. E. and Cox, B. T. (2010). k-Wave: MATLAB toolbox for the simulation and reconstruction of photoacoustic wave fields. *Journal of biomedical optics*, 15(2):021314.

Tripathi, B. B., Espíndola, D., and Pinton, G. F. (2019). Piecewise parabolic method for propagation of shear shock waves in relaxing soft solids: One-dimensional case. *International journal for numerical methods in biomedical engineering*, 35(5):e3187.

Tufail, Y., Matyushov, A., Baldwin, N., Tauchmann, M. L., Georges, J., Yoshihiro, A., Tillery, S. I. H., and Tyler, W. J. (2010). Transcranial pulsed ultrasound stimulates intact brain circuits. *Neuron*, 66(5):681–694.

Tung, Y.-S., Vlachos, F., Feshitan, J. A., Borden, M. A., and Konofagou, E. E. (2011). The mechanism of interaction between focused ultrasound and microbubbles in blood-brain barrier opening in mice. *The Journal of the Acoustical Society of America*, 130(5):3059–3067.

Turk, M. and Pentland, A. (1991). Eigenfaces for recognition. *Journal of cognitive neuroscience*, 3(1):71–86.

Tyler, W. J., Tufail, Y., Finsterwald, M., Tauchmann, M. L., Olson, E. J., and Majestic, C. (2008). Remote excitation of neuronal circuits using low-intensity, low-frequency ultrasound. *PloS one*, 3(10):e3511.

Vappou, J., Bour, P., Marquet, F., Ozenne, V., and Quesson, B. (2018). Mr-arfi-based method for the quantitative measurement of tissue elasticity: application for monitoring hifu therapy. *Physics in Medicine & Biology*, 63(9):095018.

Venkatakrishnan, L. and Meier, G. E. A. (2004). Density measurements using the background oriented Schlieren technique. *Experiments in Fluids*, 37(2):237–247.

Vetterli, M., Marziliano, P., and Blu, T. (2002). Sampling signals with finite rate of innovation. *IEEE transactions on Signal Processing*, 50(6):1417–1428.

Viallon, M., Hyacinthe, J., Goget, T., Baboi, L., Gross, P., Becker, C., and Salomir, R. (2010). Simultaneous acoustic radiation force imaging and prfs thermal monitoring at 3t for mrghifu focusing. In *Proceedings of the 18th Scientific Meeting and Exhibition of ISMRM, Stockholm*, page 247.

Vlaardingerbroek, M. T. and Boer, J. A. (2013). *Magnetic resonance imaging: theory and practice*. Springer Science & Business Media.

Vykhodtseva, N., Hynynen, K., and Damianou, C. (1994). Pulse duration and peak intensity during focused ultrasound surgery: theoretical and experimental effects in rabbit brain in vivo. *Ultrasound in medicine & biology*, 20(9):987–1000.

Vykhodtseva, N., Hynynen, K., and Damianou, C. (1995). Histologic effects of high intensity pulsed ultrasound exposure with subharmonic emission in rabbit brain in vivo. *Ultrasound in medicine & biology*, 21(7):969–979.

Vykhodtseva, N., McDannold, N., and Hynynen, K. (2008). Progress and problems in the application of focused ultrasound for blood–brain barrier disruption. *Ultrasonics*, 48(4):279–296.

Vykhodtseva, N., Sorrentino, V., Jolesz, F. A., Bronson, R. T., and Hynynen, K. (2000). Mri detection of the thermal effects of focused ultrasound on the brain. *Ultrasound in medicine & biology*, 26(5):871–880.

Wang, H., Wang, B., Normoyle, K. P., Jackson, K., Spitler, K., Sharrock, M. F., Miller, C. M., Best, C., Llano, D., and Du, R. (2014). Brain temperature and its fundamental properties: a review for clinical neuroscientists. *Frontiers in neuroscience*, 8:307.

Waxler, R. M. and Weir, C. E. (1963). Effect of pressure and temperature on the refractive indices of benzene, carbon tetrachloride, and water. *Precision Meas and Calibration*, 10(2):52–60.

Wear, K. A., Liu, Y., and Harris, G. R. (2017). Pressure pulse distortion by needle and fiber-optic hydrophones due to nonuniform sensitivity. *IEEE transactions on ultrasonics, ferroelectrics, and frequency control*, 65(2):137–148.

Webb, H., Lubner, M. G., and Hinshaw, J. L. (2011). Thermal ablation. In *Seminars in roentgenology*, volume 46, pages 133–141. Elsevier.

White, P. J., von Pattenberg, P., and Clement, G. T. (2008). A nonlinear method for high-intensity focused ultrasound (hifu) aberration reduction. In *2008 IEEE Ultrasonics Symposium*, pages 2059–2061. IEEE.

Wilkens, V. (2017). Basic ultrasonic field measurement: Overview of standardized methods and expected developments. *The Journal of the Acoustical Society of America*, 141(5):4007–4007.

Wong, A. W., Fite, B. Z., Liu, Y., Kheirolomoom, A., Seo, J. W., Watson, K. D., Mahakian, L. M., Tam, S. M., Zhang, H., Foiret, J., et al. (2016). Ultrasound ablation enhances drug accumulation and survival in mammary carcinoma models. *The Journal of clinical investigation*, 126(1):99–111.

Wong, S. H., Kupnik, M., Watkins, R. D., Butts-Pauly, K., and Khuri-Yakub, B. T. (2009). Capacitive micromachined ultrasonic transducers for therapeutic ultrasound applications. *IEEE transactions on Biomedical Engineering*, 57(1):114–123.

Xing, G., Wilkens, V., and Yang, P. (2021). Review of field characterization techniques for high intensity therapeutic ultrasound. *Metrologia*, 58(2):022001.

Yang, P.-F., Phipps, M. A., Newton, A. T., Chaplin, V., Gore, J. C., Caskey, C. F., and Chen, L. M. (2018). Neuromodulation of sensory networks in monkey brain by focused ultrasound with mri guidance and detection. *Scientific reports*, 8(1):1–9.

Yang, R., Reilly, C. R., Rescorla, F. J., Sanghvi, N. T., Fry, F. J., Franklin Jr, T. D., and Grosfeld, J. L. (1992). Effects of high-intensity focused ultrasound in the treatment of experimental neuroblastoma. *Journal of pediatric surgery*, 27(2):246–251.

Yu, Y., Shen, G., Zhou, Y., Bai, J., and Chen, Y. (2013). Quantitative assessment of acoustic intensity in the focused ultrasound field using hydrophone and infrared imaging. *Ultrasound in medicine & biology*, 39(11):2021–2033.

Zanelli, C. I. and Howard, S. M. (2006). Schlieren metrology for high frequency medical ultrasound. *Ultrasonics*, 44:e105–e107.

Zeqiri, B. and Hodnett, M. (2010). Measurements, phantoms, and standardization. *Proceedings of the Institution of Mechanical Engineers, Part H: Journal of Engineering in Medicine*, 224(2):375–391.

Zhang, T., Pauly, J. M., Vasanawala, S. S., and Lustig, M. (2013). Coil compression for accelerated imaging with Cartesian sampling. *Magnetic resonance in medicine*, 69(2):571–582.

Zheng, Y., Marx, M., Miller, G. W., and Butts Pauly, K. (2018). High sensitivity mr acoustic radiation force imaging using transition band balanced steady-state free precession. *Magnetic resonance in medicine*, 79(3):1532–1537.

Zhou, Y. (2015). *Principles and applications of therapeutic ultrasound in healthcare*. CRC press.

Zhou, Y., Zhai, L., Simmons, R., and Zhong, P. (2006). Measurement of high intensity focused ultrasound fields by a fiber optic probe hydrophone. *The Journal of the Acoustical Society of America*, 120(2):676–685.

Zhou, Y.-F. (2011). High intensity focused ultrasound in clinical tumor ablation. *World journal of clinical oncology*, 2(1):8.